STRUCTURAL AND ELECTRONIC PROPERTIES OF SEMICONDUCTORS : BULK AND NANOSCALE

THESIS SUBMITTED FOR THE DEGREE OF DOCTOR OF PHILOSOPHY (SCIENCE)

OF THE

JADAVPUR UNIVERSITY

ROBY CHERIAN

SATYENDRA NATH BOSE NATIONAL CENTRE
FOR BASIC SCIENCES
JD BLOCK, SECTOR III, SALT LAKE CITY
KOLKATA 700 098, INDIA

September, 2009

CERTIFICATE FROM THE SUPERVISOR

This is to certify that the thesis entitled **Structural and electronic properties of semiconductors : bulk and nanoscale** submitted by Sri **Roby Cherian**, who got his name registered on July 31, 2007 for the award of the Ph.D. (Science) degree of Jadavpur University, is absolutely based upon his own work under the supervision of Dr. Priya Mahadevan at the S. N. Bose National Centre For Basic Sciences, Kolkata, India and that neither this thesis nor any part of it has been submitted for any degree/diploma or any other academic award anywhere before.

Priya Mahadevan
Associate Professor,
Department of Material Sciences,
S. N. B. National Centre For Basic Sciences,
JD Block, Sector III, Salt Lake City, Kolkata 700 098, India
Date : 8^{th} September 2009

Dedicated to

My Parents and Darly

Acknowledgments

First and foremost, I would like to thank my supervisor Dr. Priya Mahadevan for her continuous support in carrying out this research. She always kept me motivated in the area of semiconductors in the bulk and nanoscale with her ideas. She was always ready to listen to my ideas and gave a right path to make me think deeply on the new problems we took up. She also helped me to collaborate with others so as to bring out the best from my side. I really had a nice period during my research which really has increased the thirst for my future research.

During my research work I came in close contact with Dr. Clas Persson of Sweden. During my research I had a chance to visit his group and during the one month stay over there he was always there to sort out all my problems that a first time foreigner faces. I cannot ever forget all the wonderful hospitality and enjoyable discussions with him during that short period. Here at this moment I would like to acknowledge the Swedish Foundation for International Cooperation in Research and Higher Education (STINT) for providing me the funding for the whole trip.

During my research period, I also came in contact with Prof. D. D. Sarma and his group members. We had active collaboration in our work on semiconductor nanocrystals and few of their experimental works really motivated us for the better theoretical understanding of the problems raised by them.

I would thank all my group members- Subhro, Ashis, Kapil, Abhinav, Hirak and Bipul for making the days at S. N Bose Institute a memorable one. I would like to thank others like - Prashant, Shankar, Ambika, Sujoy, Rajiv, Soumyajith, Manoj, Nurapanth, Gregor, Binit, Rexy of IOB bank, Ajith, Abhijit-Chalo Chalo, and the list continues, who made my life at Kolkata a pleasant one. For my research work I am really thankful for my few of the silent friends named: snbpc41 (a dell computer) and the supercomputers DMS, PMG1 and HPC.

Financial support by DAE-BRNS during my first two years of research and rest by Council of Scientific and Industrial Research (CSIR) - Government of India is gratefully acknowledged.

And finally, my family for their continued support.

Roby Cherian
Kolkata, India
September, 2009

List of Publications

1. **R. Cherian**, and P. Mahadevan
   Bulk and nanoscale GaN: Role of Ga d states
   Phys. Rev. B. **76**, 075205 (2007).

2. **R. Cherian**, and P. Mahadevan
   Size dependence of lattice constants of semiconductor nanocrystals
   Appl. Phys. Lett. **92**, 043130 (2008).
   This article was selected for the February 18, 2008 issue of Virtual Journal of Nanoscale Science and Technology.

3. **R. Cherian**, P. Mahadevan, and C. Persson
   Trends in ferromagnetism in Mn-doped dilute III-V alloys from a density functional perspective
   Phys. Rev. B. **79**, 195211 (2009).

4. **R. Cherian**, A. Kumar, and P. Mahadevan
   Effects of quantum confinement on the conduction band minimum of semiconductors
   J. Nanoscience and Nanotechnology, **9**, 5673 (2009).

5. **R. Cherian**, and P. Mahadevan
   Effects of non-stoichiometry on the lattice constant of semiconductor nanocrystals: CdSe and GaAs
   J. Nanoscience and Nanotechnology, **9**, 5564 (2009).

6. **R. Cherian**, A. K. Nandy, and P. Mahadevan
   Can Nano Silicon be Made Optically Active?
   J. Nanoscience and Nanotechnology, **9**, 5561 (2009).

7. **R. Cherian**, P. Mahadevan, and C. Persson
   Role of Coulomb interactions in semicore levels : Implication on band offsets

Accepted in *Solid State Communications*

8. A. Nag, **R. Cherian**, P. Mahadevan, and D. D. Sarma
   Tuning of dopant emission in Mn^{2+}-doped CdS nanocrystals
   Under preparation

9. **R. Cherian**, and P. Mahadevan
   A new hat for the passivating species
   Under preparation

10. **R. Cherian**, C. Gerard, P. Mahadevan, and D. D. Sarma
    Size dependence of the bulk modulus of semiconductor nanocrystals
    Under preparation

11. **R. Cherian** and P. Mahadevan
    Role of semicore Ga d states in determining the valence band offset of common anion semiconductors
    Under preparation

12. **R. Cherian**, P. Mahadevan and B. Koiller
    Band alignment in GaAs/AlAs superlattices
    Under preparation

Contents

List of Figures

List of Tables

Chapter 1

Introduction

Semiconductors have been the workhorse of modern day electronics from the fifties. However still the interest in these materials continues as new phenomena are been discovered in these materials. One such example are dilute magnetic semiconductors where a small concentration of transition metal doping in conventional semiconductors results in magnetism, sometimes even at room temperature. This has thrown open an entire new branch of physics - spintronics wherein one uses the spin degree of freedom of the electron in addition to the charge to construct new generation devices. Another area that has received a lot of interest are nanocrystalline semiconductors. The properties of these nanomaterials strongly depends on the shape and size and are quite different from their bulk counterparts. An understanding of the electronic structure of these systems will provide insights into the interesting properties observed in them. In this thesis we have studied the electronic structure of semiconductors both in the bulk and the nanoscale limit using *ab-initio* methods. For better understanding of the microscopic origin of certain phenomena we have also constructed model Hamiltonians which we use to discuss the phenomena. **Chapter 2** introduces and discuss in some detail the theoretical frameworks which we used to carry out electronic structure calculations in this thesis.

With recent advances in computational power, theory and specifically *ab-initio* density functional theory have played an important role in the design of materials with tailor-made properties. An important class of materials that have received considerable attention are the nitrides. Alloys of GaInNAs have been recognized as important materials for the development of long wavelength solid-state lasers emitting within the fibre-optic commu-

nication wavelength window (1.3 to 1.55 μm) [1]. GaInNAs semiconductor quantum dots with dilute amount of nitrogen substitutional impurities are promising candidates for the active region in the next generation of optoelectronic devices [2]. Transition metal doped GaN has been found to exhibit ferromagnetism at room temperature [3] which could make these materials useful in the emerging area of spintronics. Calculations for the systems of interest in the context of the nitrides, dilute nitrides as well as quantum dots, are usually performed for periodic systems considering large and representative supercells. These are computationally demanding within an *ab-initio* approach. It is therefore useful to have accurate and reasonable approximations which decrease the computational cost. The role of the Ga $3d$ states in determining the physical properties of GaN has received considerable attention over the past two decades. Unlike in the case of other Ga-V semiconductors, one finds that in GaN the Ga $3d$ core states are not chemically inert and the valence band has considerable Ga d character [4]. In **Chapter 3** we studied the role of Ga $3d$ states in determining the properties of bulk as well as nanocrystals of GaN using projected augmented wave (PAW) potentials. PAW potentials give us the freedom to toggle between using the Ga $3d$ in the valence and in the core and allows us to simultaneously examine the modifications in the electronic properties. A significant contribution of the Ga d states in the valence band is found to arise from interaction of Ga $4d$ states with the dominantly N p states making up the valence band. The errors in the calculated lattice constant arising from not treating the Ga $3d$ states as a part of the valence are found to be similar, $\sim 1\%$, for bulk as well as for nanocrystals of GaN.

The positions of the semicore Ga d levels in GaX semiconductors (X = N, P, and As) are underestimated in density functional calculations using either the local density approximation LDA or the generalized gradient approximation GGA for the exchange functional. Correcting for this inaccuracy within LDA+U calculations with an on-site Coulomb interaction U on the semicore d-states results in a modest enhancement of the band gap. The belief for the opening up of band gap has been that the t_2 states of the semicore d states interact with the states comprising the valence band maximum with the same symmetry pushing them up [5]. Recently Janotti *et al.* [6] examined the mechanism of the increase in the band gap with a U on the semicore states. They [6] found shifts in both valence band maximum and conduction band minimum and thus questioned the

earlier model [5]. The shift in the conduction band minimum was understood to be due to the modified screening effects arising from the a U on the semicore states. We re-examined this proposition and we show that this modest enhancement of the band gap energy comes from the movement of the valence band maximum alone, thus not affecting the conduction band states. Further, the localization of the charge on Ga d states with U leads to a regulation of charge on Ga. This yields a shift of 1-2 eV of the core levels on the Ga atom while the anion core levels remain unchanged.

Advances in growth techniques have made it possible to fabricate perfect single crystal layers of one material over another by epitaxy. These materials known as heterojunctions have the advantage of giving rise to high quality materials, in addition to suggesting the possibility of changing the properties of the materials over wide limits as a function of the layer thickness which can be varied from a fraction of atomic layer to hundreds of micrometers. An important class of materials with wide ranging technological application that have emerged are those in which confinement leads to properties entirely different from the bulk. The development of the physics and technology of semiconductor heterostructures has resulted in remarkable changes in our everyday life. Heterostructure electronics is widely used in many areas. In order to have a better handle on designing materials, it is useful to have a good understanding of the microscopics. A key parameter that determines the functionality of the semiconductor heterojuction device is the band offsets between the materials involved. It is an established fact that in isovalent heterojunctions of lattice-matched semiconductors the band offset depends only on the bulk properties of the two materials, while at heterovalent heterojunctions it crucially depends on the interfacial strain and the other microscopic details. Thus the problem reduces to determining the role of the microscopic interactions in the bulk electronic structure of the materials making up the heterostructure. In this chapter we reexamine the problem of the origin of the valence band offsets in the common anion lattice-matched semiconductors such as GaX/AlX where X= N, P and As. Our calculated valence band offset between the common anion pairs of semiconductors GaX/AlX (X=N, P and As) was found to be 0.72, 0.48 and 0.50 eV respectively. This is in agreement with other estimates [7] as well as other experimental estimates [8]. An early common-anion theory [9] suggested that ΔE_v(AX/BX) between two materials with the same anion type should be zero, but

the observed large band offsets have later been associated with a *p*-*d* interaction present in the GaX [5], having active semicore Ga *d* states in contrast to AlX. The role of *p*-*d* interactions in determining the valence band offset was studied for the first time. Quantitative estimates were obtained starting from a microscopic Hamiltonian found to give good description of the band structure of GaX and AlX semiconductors. Our studies show that this interaction cannot alone account for the large valence band offsets. Our studies reveal that the important interaction that bring about this observed valence band offset is from the *p*-*p* (cation-*p* and anion-*p*) interactions.

In the case of heterostructures the layer thicknesses and chemical composition can be controlled over a length scale comparable to or smaller than the electron de Broglie wavelength. This results in novel quantum effects related to size. Quantum well structures can be designed to perform special functions that are the core of many modern quantum devices. In **Chapter 4** we considered GaAs/AlAs superlattices, where we studied the type of band alignment and the nature of the valence band maximum and conduction band minimum wavefunction envelope in different cases by changing the GaAs and AlAs layer thickness. We observed a transition of the superlattice from a type-II to type-I when the GaAs well thickness was varied and the critical thickness at which this occurs was found to be around 20 Å. This critical thickness is slightly less than the thickness of 25 Å found by pseudopotential and tight binding approaches [10, 11]. Combining the techniques of photo-luminescence and photo-luminescence excitation spectroscopy K. J. Moore *et al.* [12] observed that for the fixed GaAs thickness at 25 Å the band alignment shows type-II when the AlAs thickness is greater than 15 Å while for AlAs thickness less than 10 Å they observed a type-I behavior. Studying the other limit where few AlAs is sandwiched between the GaAs layers we see that the superlattice is always type-I. Our studies on the ground state wavefunction of the holes, agrees quite well with the nature of the ground state wavefunction one expects from a particle in a potential well problem while the ground state wavefunction of the electrons deviates from the particle in a potential well problem for certain cases. In this chapter we also determine the shifts of the conduction band minimum of semiconductor nanocrystals as a function of size from *ab-initio* calculations, where confinement of carriers happens in all the three directions. The method has been applied to CdSe as well as GaAs and the shifts determined. A monotonic decrease is

found as a function of particle size, as expected. However, the most unusual aspect of our result is that the conduction band bottom approaches bulk-like values for the largest CdSe particles that we have studied here in contrast to expectations from other empirical theories [13, 14, 15].

Alloys at the dilute limit should show strong valence band bowing effects, and transition metal doping in dilute alloys has been suggested as a possible route to enhance ferromagnetic stability [16]. The basic idea that one aims to exploit here is to use semiconductors with band edges energetically closer to the Mn $3d$ levels. This increases the hybridization between the host anion p states and the Mn d states. The increased Mn character of the holes results in a deeper acceptor level in the band gap, thus the ferromagnetism-mediating holes are more localized. Hence the competition is between delocalization and increased magnetic character and the question is how does the T_c evolve. Recent experiments [17, 18] have looked at the dilute limit of $Ga_{1-x}Mn_xAs_{1-y}P_y$ and $Ga_{1-x}Mn_xAs_{1-y}N_y$ with y $\sim$ 0.01-0.04. They observed a strong decrease in T_c with increasing y even at this dilute limit. In **Chapter 5** we have examined these materials and have found that alloy scattering destroys the ferromagnetic stability in this limit. The role of the impurity potentials and the role of strain in the modified ferromagnetic stability has been identified for the first time in these systems. The Curie transition temperatures were evaluated within a mean field approximation.

Semiconductor nanocrystals have been intensively studied in recent times because of the dependence of their properties on nanocrystal size, an effect which has tremendous technological implications. In **Chapter 6** we studied the size dependence effect on the lattice constant of various semiconductor nanocrystals. All atoms at the surface would have broken coordination, while the interior having a bulk like coordination. As a result bonds at the surface would be shorter compared to the interior. These nanocrystals are termed as unpassivated nanocrystals. Experimentally the samples are usually passivated by organic molecules and since carrying out an *ab-initio* calculation of this real situation is computationally very expensive, we use hydrogens or pseudo-hydrogens [19] as the passivants. In our studies we found that even though these passivated nanocrystals attain an average bond-length very close to the bulk-like bond-length values for very small nanocrystals sizes ($\sim$ 20 Å diameter) there exist deviation in the bond-length as a function

of depth from the surface, with the largest deviation found at the surface. In the absence of passivant, experimentally this can be thought of the situation where the nanocrystals are passivated with weak passivants, we see that the nanocrystals shows larger deviation in the average bond-length values from the bulk-like bond-length values. These results have implication on the experimental studies where one might have different types of passivants and the role played by the passivants is strongly reflected on the average lattice constant of the nanocrystal. We also studied the effect of surface stoichiometry on the average equilibrium lattice constant of nanocrystals and we show that different growth condition could result in similar sized nanocrystals with different average equilibrium lattice constant. In this chapter we also focused on the modification of the bulk modulus of semiconductor nanocrystals with size. Experimental studies on semiconductor nanocrystals have been found to have an enhanced bulk modulus compared to values for the bulk [20, 21, 22]. As one does not always have a homogeneous distribution of particles it is difficult to study the renormalization of the mechanical properties experimentally. In this context theoretical calculations which can simulate the ideal situation would provide valuable insight into the modifications as a function of size. This class of materials was examined to see if there was a size dependence of the bulk modulus. A phenomenological law was derived which independently gets the bulk limit accurately.

This led us to the next problem of a choice of suitable passivant in binary nanocrystals. Experimental studies have shown the importance of surface stoichiometry in optimizing the optical properties of nanocrystals. In **Chapter 7** we examined whether it was possible during growth to have only one type of atoms at the surface. In the absence of any passivants one finds the existence of mid gap states which is as a result of the broken coordination at the surface. Now in the presence of passivants one finds that these surface states are moved into the valence band / conduction band by ~ 0.5 eV or more. This can happen in two ways. The first via a surface reconstruction and the second via the interaction of the surface atoms with the passivants. The pseudo-hydrogens here corresponds to the passivants used in the experiment and in our studies we find that they interact strongly with the surface atoms. We find the binary nanocrystals with just one type of the atoms at the surface to be strongly stabilized in the presence of passivation. A strong role was found to be played by the passivating ligands in determining the surface

structure. While the conventional belief is that a passivant prevents agglomeration of nanocrystals and saturates dangling bonds, here it dons the new role of being able to control the surface stoichiometry.

A key aspect of nanocrystals that have been intensively studied in recent times are their optical properties. Bulk silicon is optically inactive. Efforts have been made to look for other forms of silicon which might be optically active. Routes that have been taken include quantum confinement of Si between SiO_2 layers [23], porous silicon [24] as well as quantum dots / nanosized particles of Si [25]. In **Chapter 8** we went on to examine whether similar sized silicon particles with different shapes have the same physical properties and whether silicon may be rendered optically active by playing with the shape of the nanocrystals where one also has the effect of broken translation symmetry. In this chapter we also studied the tuning of the dopant emission in Mn^{2+}-doped CdS nanocrystals. Recent experimental studies [26] showed that a controlled tuning of Mn^{2+} *d*-emission color from Mn^{2+}-doped CdS nanocrystals, in the range of yellow to red by making slight changes in the reaction temperature was possible. We carried out *ab-initio* calculations and determine the *d-d* transition energies for the Mn^{2+} ion residing at different location in the CdS nanocrystal. Our studies show that the Mn^{2+} ions residing at surface/sub-surface regions of the nanocrystal experience a different crystal field compared to those residing at the core and thus giving rise to different emission energies. We find that the lower energy emissions is from the Mn^{2+} ions situated in the perturbed environments, namely near the surface/sub-surface regions of the nanocrystal. With increase in reaction temperature the particle size was found to increase [26] and as a result of this one has a smaller surface to bulk ratio leading to higher probability of Mn^{2+} incorporation in the interior of the nanocrystal than on the surface and thus leading to experimentally observed shift of the emission peak towards higher energies [26].

Bibliography

[1] M. Kondow, K. Uomi, K. Hosomi, and T. Mozume, J. Appl. Phys. **33**, L1056 (1994); J. S. Harris, Semicond. Sci. Technol. **17**, 880 (2002); H. Riechert, A. Ramakrishnan, and G. Steinle, *ibid.* **17**, 892 (2002).

[2] C. Y. Liu, S. F. Yoon, Z. Z. Sun, and K. C. Yew, Appl. Phys. Lett. **88**, 081105 (2006); C. Y. Liu, S. F. Yoon, Q. Cao, C. Z. Tong, and Z. Z. Sun, Nanotechnology **17**, 5627 (2006); Q. Gao, M. Buda, H. H. Tan, and C. Jagadish, Electrochem. Solid-State Lett. **8**, G57 (2005); Z. Z. Sun, S. F. Yoon, K. C. Yew, B. X. Bo, D. A. Yan, and T. C. Hang, Appl. Phys. Lett. **85**, 1469 (2004); S. Makino, T. Miyamoto, T. Kageyama, N. Nishiyama, F. Koyama, and K. Iga, J. Cryst. Growth **221**, 561 (2000).

[3] M. L. Reed, N. A. El-Masry, H. H. Stadelmaier, M. K. Ritums, M. J. Reed, C. A. Parker, J. C. Roberts, and S. M. Bedair, Appl. Phys. Lett. **79**, 3473 (2001); S. E. Park, H. Lee, Y.C. Cho, and S. Jeong, Appl. Phys. Lett. **80**, 4187 (2002).

[4] V. Fiorentini, M. Methfessel, and M. Scheffler, Phys. Rev. B **47**, 13353 (1993).

[5] S. H. Wei and A. Zunger, Phys. Rev. Lett. **59**, 144 (1987).

[6] A. Janotti, D. Segev, and C. G. Van de Walle, Phys. Rev. B **74**, 045202 (2006).

[7] S. H. Wei and A. Zunger, Appl. Phys. Lett. **72**, 2011 (1998).

[8] E. T. Yu, D. H. Chow, and T. C. McGill, Phys. Rev. B **38**, 12764 (1988); K. Hirakawa, Y. Hashimoto, and T. Ikoma, Appl. Phys. Lett. **57**, 2555 (1990).

[9] W. A. Harrison, J. Vac. Sci. Technol. **14**, 1016 (1977).

[10] A. Franceschetti and A. Zunger, Phys. Rev. B **52**, 14664 (1995).

[11] J. G. Menchero, T. G. Dargam, and Belita Koiller, Phys. Rev. B **61**, 13021 (2000).

[12] K. J. Moore, P. Dawson, and C. T. Foxon, Phys. Rev. B **38**, 3368 (1988).

[13] S. Sapra and D. D. Sarma, Phys. Rev. B **69**, 125304 (2004).

[14] L. Wang and J. Li, Phys. Rev. B **69**, 153302 (2004).

[15] P. E. Lippens and M. Lannoo, Phys. Rev. B **41**, 6079 (1990).

[16] A. H. MacDonald, P Schiffer, and N Samarth, Nature Mater. **4**, 195 (2005).

[17] P. R. Stone, K. Alberi, S. K. Z. Tardif, J. W. Beeman, K. M. Yu, W. Walukiewicz, and O. D. Dubon, Phys. Rev. Lett. **101**, 087203 (2008).

[18] K. Alberi, K. M. Yu, P. R. Stone, O. D. Dubon, W. Walukiewicz, T. Wojtowicz, X. Liu, and J. K. Furdyna , Phys. Rev. B. **78**, 075201 (2008).

[19] X. Huang, E. Lindgren, and J. R. Chelikowsky, Phys. Rev. B **71**,165328 (2005).

[20] Z. Wang, K. Tait, Y. Zhao, D. Schiferl, C. Zha, H. Uchida, and R. T. Downs, J. Phys. Chem. B **108**, 11506 (2004).

[21] Z. Wang, S. K. Saxena, V. Pischedda, H. P. Liermann, and C. S. Zha, Phys. Rev. B **64**, 012102 (2001).

[22] J. Z. Jiang, J. S. Staun Olsen, L. Gerward, and S. Morup, Europhys. Lett. **44**, 620 (1998).

[23] Z. H. Lu, D. J. Lockwood, and J. M. Baribeau, Nature **378**, 258 (1995).

[24] L. T. Canham, Appl. Phys. Lett. **57**, 1046 (1990).

[25] Y. Kanzawa, T. Kageyama, S. Takeoka, M. Fujii, S. Hayashi, and K. Yamamoto, Solid State Commun. **102**, 533 (1997).

[26] A. Nag and D. D. Sarma (unpublished).

Chapter 2

Density Functional Theory (DFT) way of solving quantum many body problem

2.1 The many-particle Hamiltonian

Atoms, molecules, clusters or solids, is a collection of heavy, positively charged particles (nuclei) and lighter, negatively charged particles (electrons). If we have N nuclei, we are dealing with a problem of N+ZN electromagnetically interacting particles. This is a many-body problem, and system is described by the many-particle Schrögінger equation of the form $H\Psi(\mathbf{R},\mathbf{r}) = E\Psi(\mathbf{R},\mathbf{r})$. The exact many-particle Hamiltonian for the system is :

$$H = -\sum_i \frac{\hbar^2}{2m_e}\nabla^2_{r_i} - \sum_I \frac{\hbar^2}{2M_I}\nabla^2_{R_I} - \sum_{i,I} \frac{Z_I e^2}{|\mathbf{R}_I - \mathbf{r}_i|} + \sum_{i>j} \frac{e^2}{|\mathbf{r}_i - \mathbf{r}_j|} + \sum_{I>J} \frac{Z_I Z_J e^2}{|\mathbf{R}_I - \mathbf{R}_J|} \quad (2.1)$$

The mass of the nucleus at $\mathbf{R}_I$ is M_I, the electrons have mass m_e and are at $\mathbf{r}_i$. The first term is the kinetic energy operator for the electrons, the second for the nuclei. The last three terms describe the Coulomb interaction between electrons and nuclei, between electrons and other electrons, and between nuclei and other nuclei. To solve this problem exactly is a very difficult issue. In order to find acceptable approximate eigenstates, we will need to make approximations at different levels.

The first step towards the simplification of the above equation is the *Born-Oppenheimer (B-O) approximation*(1927)[1] : since ions are much heavier than electrons ($(m_e/M_I) \sim$

(1/1836) for H atom), they move much slower compared to electrons and the electrons respond instantaneously to any ionic motion. In essence the electronic and the ionic degrees of freedom can be decoupled and the electronic properties can be calculated by assuming that the ions are fixed to a particular configuration. Following this approximation, the kinetic energy of ions can be neglected and the ion-ion interaction (last term in Eqn. (2.1)) is assumed to be constant. The constant term, called Madelung energy, is calculated classically. So under B-O approximation, the many-body Hamiltonian for a system of N interacting electrons moving in the field of fixed ion cores, takes the form

$$H = -\sum_i \frac{\hbar^2}{2m_e}\nabla^2_{r_i} - \sum_{i,I} \frac{Z_I e^2}{|\mathbf{R}_I - \mathbf{r}_i|} + \sum_{i>j} \frac{e^2}{|\mathbf{r}_i - \mathbf{r}_j|} \tag{2.2}$$

2.2 Single-particle approximation

Even after this simplification, it represents a very complicated many-electron eigen value problem and further approximation is needed to solve it. Efforts have been put, therefore, to develop an *effective single-particle picture*, in which the system of interacting electrons can be mapped into a system of non-interacting quantum mechanical particles that approximates the behavior of original system. Two distinct approaches have been put forward in this direction: *wave function approach* and *density functional theory*.

2.2.1 Wave function approach

Hartree (1928) first expressed the many-body wave function as a product of single-electron functions $\{\phi_i(\mathbf{r}_i)\}$ as $\psi^H(\mathbf{r}_1, \mathbf{r}_2, \ldots, \mathbf{r}_N) = \phi_1(\mathbf{r}_1)\phi_2(\mathbf{r}_2)\ldots\phi_N(\mathbf{r}_N)$ and solved, numerically, the equation for each electron moving in a central potential due to other electrons and the nucleus [2]. This simplest approximation can only take into account the electron-electron Coulomb repulsion in a mean-field way, neglecting the exchange and correlation properties completely. The next level of sophistication was then introduced by Fock (1930) [3], incorporating the antisymmetric character of electronic wave function in terms

of Slater determinant[4]

$$\psi^{HF} = \frac{1}{\sqrt{N!}} \begin{vmatrix} \phi_1(\mathbf{r}_1) & \phi_1(\mathbf{r}_2) & \dots & \phi_1(\mathbf{r}_N) \\ \phi_2(\mathbf{r}_1) & \phi_2(\mathbf{r}_2) & \dots & \phi_2(\mathbf{r}_N) \\ \vdots & \vdots & & \vdots \\ \phi_N(\mathbf{r}_1) & \phi_N(\mathbf{r}_2) & \dots & \phi_N(\mathbf{r}_N) \end{vmatrix}, \tag{2.3}$$

Application of the variational principle shows that such one-electron wave functions satisfy the Hartree-Fock (H-F) equations like

$$\left[-\frac{\hbar^2}{2m_e} \nabla^2_{r_i} + V_{ion}(\mathbf{r}_i) + V_i^H(\mathbf{r}_i) + V_i^X \right] \phi_i(\mathbf{r}_i) = \epsilon_i \phi_i(\mathbf{r}_i) \tag{2.4}$$

with

$$V_i^H(\mathbf{r}_i) = e^2 \sum_j^{occ} \int \frac{|\phi_j(\mathbf{r}_j)|^2}{|\mathbf{r}_i - \mathbf{r}_j|} d\mathbf{r}_j \tag{2.5}$$

as the Hartree potential and the exchange potential is given by

$$V_i^X \phi_i(\mathbf{r}_i) = -\sum_j^{occ} \phi_j(\mathbf{r}_i) \int \phi_j^*(\mathbf{r}_j) \frac{e^2}{|\mathbf{r}_i - \mathbf{r}_j|} \phi_i(\mathbf{r}_j) d\mathbf{r}_j \tag{2.6}$$

The screening potential includes both Hartree and exchange terms. The exchange term V_i^X is difficult to derive in practice because it is non-local and related to the interaction between all electrons in the system. Consequently, the Hartree-Fork approach has a highly computational cost and is therefore restricted to small systems.

In agreement with the variational principle, the Hartree-Fock energy E_0^{HF} is higher than the exact ground state energy E_0^{exact} of the many body system and the difference E_0^{exact} - E_0^{HF} is called the correlation energy. In spite of the importance and achievements of the Hartree-Fock approximation, corrections beyond it are often considered due to the fact that a single determinantal state, even with the best possible orbitals, remains in general a rather poor representation of the complicated ground state wave function of a many-body system. Therefore, methods like configuration interaction (CI) approach have been developed by quantum chemists, which consider a linear combination of different determinantal states to improve the situation. However, such approach becomes quickly computationally prohibitive as the system size grows.

2.2.2 Density functional theory

Hohenberg and Kohn proposed the Density Functional Theory (DFT) [5, 6] to deal with many-body system problems more efficiently. The formulation of DFT applies to any system of interacting particles in an external potential $V_{ext}(\mathbf{r})$. The main result of DFT is that the ground state properties of a many electron system are uniquely determined by its electron distribution. In other words, all ground state properties of the many electron system are functional of its ground state electron distribution. When the ground state electron distribution of the many electron system is determined, its external potential is also uniquely determined.

In DFT one ignores the precise details of the many-body wave function $\psi(\mathbf{r}_1, \mathbf{r}_2, \ldots, \mathbf{r}_N)$ and takes the density of electrons in the system $\rho(\mathbf{r}) = \mathrm{N} \int \psi^*(\mathbf{r}, \mathbf{r}_2, ..., \mathbf{r}_N)\psi(\mathbf{r}, \mathbf{r}_2, ..., \mathbf{r}_N)$ $d\mathbf{r}_2 d\mathbf{r}_3 .... d\mathbf{r}_N$ as the basic variable. This is a huge simplification, since the many-body wave functions need not to be explicitly specified, as is in case of Hartree and Hartree-Fock approximations. Thus, instead of starting with a drastic approximation for the behavior of the system, one can develop the approximate single-particle equations in an exact manner, and then introduce approximations as needed. Also it gives huge simplification by replacing the complex object like wave-function which depends on the positions of all the N electrons by electron density which depends only on single position.

Basic theorems of DFT and Kohn-Sham equation

Density functional theorem can be expressed in terms of two basic theorems:
Theorem I: For a system of interacting particles in an external potential $V_{ext}(\mathbf{r})$, the potential $V_{ext}(\mathbf{r})$ is determined uniquely, up to an additive constant, by the ground state density. This defines a one-to-one correspondence between an external potential $V_{ext}(\mathbf{r})$ and the density $\rho(\mathbf{r})$. Since external potential determines the wave function, the wave function must be a unique functional of density. Therefore, for a given ground state density, all properties of the system are completely determined.
Theorem II: If T represents the kinetic energy and U the electron-electron interaction, then the expression, $F[\rho(\mathbf{r})] = \langle\psi|T + U|\psi\rangle$ must be a universal functional of the density,

since the kinetic energy and the interaction energy are functional of density only. From this considerations, we conclude that the total energy of the system is a functional of the density and is given by,

$$E_v[\rho(\mathbf{r})] = \langle\psi|\mathcal{H}|\psi\rangle = F[\rho(\mathbf{r})] + \int V_{ext}(\mathbf{r})\rho(\mathbf{r})d\mathbf{r} \tag{2.7}$$

The Hohenberg-Kohn variational theorem states that if the functional $E_v[\rho(\mathbf{r})]$ is varied with respect to $\rho(\mathbf{r})$, then $E_v[\rho_0(\mathbf{r})]$ takes the lowest value, corresponding to the ground state, with the correct ground state density $\rho_0(\mathbf{r})$, *i.e.* $E_v[\rho_0] \leq E_v[\rho]$.

Now to reduce the expression (2.7) to a single particle equation, one can write the universal functional as

$$F[\rho] = T_S[\rho] + \frac{e^2}{2}\int \frac{\rho(\mathbf{r})\rho(\mathbf{r}')}{|\mathbf{r}-\mathbf{r}'|}d\mathbf{r}d\mathbf{r}' + E_{xc}[\rho(\mathbf{r})] \tag{2.8}$$

where $T_S[\rho]$ is the kinetic energy of the non-interacting electrons with density $\rho(\mathbf{r})$, second term is the classical mean-field inter-electron Coulomb (Hartree) energy $E_{Coulomb}$, which we separate out from the electron-electron interaction term in F and the third term E_{xc} = ($\langle T\rangle$ - $T_S[\rho]$ + $\langle U\rangle$ - $E_{Coulomb}$) is the non-classical many-body exchange-correlation energy functional. Therefore the ground-state energy functional in the Kohn-Sham approach is

$$E_{KS}[\rho] = T_S[\rho] + \int V_{ext}(\mathbf{r})\rho(\mathbf{r})d\mathbf{r} + \frac{e^2}{2}\int \frac{\rho(\mathbf{r})\rho(\mathbf{r}')}{|\mathbf{r}-\mathbf{r}'|}d\mathbf{r}d\mathbf{r}' + E_{xc}[\rho(\mathbf{r})] \tag{2.9}$$

There are three major problems in evaluating the functional $E_{KS}[\rho]$: (*i*) one needs a method of self-consistently evaluating the correct ground state charge density $\rho(\mathbf{r})$, (*ii*) evaluation of $T_S[\rho]$ given only $\rho(\mathbf{r})$ cannot be done straightforwardly as there is no information on wave functions, and (*iii*) the functional $E_{xc}[\rho]$ remains unknown and must therefore be represented in some simple and sufficiently accurate form.
These difficulties were resolved by Kohn and Sham (1965). The minimization of E_{KS} is carried out subject to the constraint of normalized density $\int \rho(\mathbf{r})d\mathbf{r} = N$. Application of the variational principle of the Kohn-Sham theory requires that for the ground state

$$\frac{\delta}{\delta\rho(\mathbf{r})}\{E_{KS}[\rho] - \mu N\} = 0 \tag{2.10}$$

μ is the Lagrange multiplier. Using Eqn. (2.9), one gets,

$$\frac{\delta T_S[\rho]}{\delta\rho(\mathbf{r})} + V_{KS}(\mathbf{r}) = \mu \tag{2.11}$$

where

$$V_{KS}(\mathbf{r}) = v(\mathbf{r}) + V_H(\mathbf{r}) + V_{xc}(\mathbf{r}) = v(\mathbf{r}) + \int \frac{\rho(\mathbf{r}')}{|\mathbf{r} - \mathbf{r}'|} d\mathbf{r}' + \frac{\delta E_{xc}}{\delta \rho(\mathbf{r})} \tag{2.12}$$

Kohn and Sham showed that solving Eqn. (2.11) is equivalent to solving the following set of single-particle Schrödinger-like equations for the variational wave-functions of fictitious non-interacting electrons

$$\left[-\frac{\hbar^2}{2m_e} \nabla^2 + V_{KS}(\mathbf{r}) \right] \phi_i = \epsilon_i \phi_i \tag{2.13}$$

where ϕ_i and ϵ_i are the single-particle wave-functions and eigenvalues, respectively, such that $\rho(\mathbf{r}) = \sum_i |\phi_i(\mathbf{r})|^2$. The Eqn. (2.13), therefore, represents the set of Kohn-Sham self-consistent field equations.

The first two difficulties outlined above are now resolved. Firstly, the ground-state electronic charge density is obtained through the self-consistent solution of Eqn. (2.13). Secondly, once the self-consistency is reached, $T_S[\rho]$ is calculated as

$$T_S[\rho] = \sum_i \langle \phi_i | -\frac{\hbar^2}{2m_e} \nabla^2 | \phi_i \rangle = \sum_i \epsilon_i - \int V_{KS}[\rho] \rho(\mathbf{r}) d\mathbf{r} \tag{2.14}$$

Exchange-correlation functional

As mentioned earlier, the third difficulty with the application of DFT is that the exact form of $E_{xc}[\rho]$ is unknown and it's a great challenge in DFT. It is to be noted that this exchange-correlation energy contains — (*i*) kinetic correlation energy, which is the difference in the kinetic energy functional between the real and the non-interacting system, (*ii*) the exchange energy, which arises from the requirement of antisymmetric nature of fermions, (*iii*) Coulombic correlation energy, which arises from the inter-electronic repulsion and (*iv*) a self-interaction correction.

Two levels of approximations have been suggested to estimate $E_{xc}[\rho]$: local density approximation (LDA) and generalized gradient approximation (GGA). They are very successful in predicting most of the material properties and below we discuss them briefly.

The local density approximation (LDA)

In 1965, W. Kohn and L. J. Sham proposed the local density approximation (LDA) [6] in order to deal with the exchange correlation energy. They supposed that there exist the exchange correlation energy density in the many-electron system, and the exchange correlation energy of a point in the space of the system is only related to the electron density of that point.

In this approximation it is assumed that the electronic charge density in the system corresponds to that of a homogeneous electron gas and the functional $E_{xc}[\rho]$ is approximated as

$$E_{xc}^{LDA}[\rho(\mathbf{r})] = \int \rho(\mathbf{r})\mathcal{E}_{xc}[\rho(\mathbf{r})]d\mathbf{r}, \tag{2.15}$$

where $\mathcal{E}_{xc}[\rho]$ is the exchange plus correlation energy per electron in a homogeneous electron gas with electron density $\rho(\mathbf{r})$. The functional derivative of E_{xc}^{LDA} gives the exchange-correlation potential within LDA,

$$V_{xc}^{LDA} = \frac{\delta E_{xc}^{LDA}}{\delta\rho} = \mathcal{E}_{xc}\left[\rho(\mathbf{r})\right] + \rho(\mathbf{r})\frac{\partial\mathcal{E}_{xc}[\rho]}{\partial\rho}. \tag{2.16}$$

The contribution of exchange to the total energy is $\mathcal{E}_x^{LDA}[\rho(\mathbf{r})] = -\frac{3}{4}e^2\left(\frac{3}{\pi}\right)^{1/3}[\rho(\mathbf{r})]^{1/3}$ (one can obtain this general form of exchange part starting from the solution of a uniform system [7]). For the correlation part, a number of expressions have been given. In all these expressions, the exchange-correlation functional is written as

$$E_{xc}^{LDA}[\rho(\mathbf{r})] = \int(\mathcal{E}_x[\rho(\mathbf{r})] + \mathcal{E}_c[\rho(\mathbf{r})])\rho(\mathbf{r})d\mathbf{r} \tag{2.17}$$

where the pure exchange energy $\mathcal{E}_x[\rho]$ is the expression as given above. The expressions for correlation energy are usually given in terms of Wigner-Seitz radius, $r_s = (3/4\pi\rho(\mathbf{r}))^{1/3}$. The expression proposed by Wigner [8] extrapolates between known limits in r_s, obtained by series expansions. The parameters that appear in the expression proposed by Hedin and Lundquist [9] are determined by fitting to the energy of the uniform electron gas, obtained by numerical methods at different densities. A similar type of expression was proposed by Perdew and Zunger [10], which captures the more sophisticated numerical calculations for the uniform electron gas at different densities performed by Ceperly and Alder [11]. The common feature in all these approaches is that E_{xc} depends on $\rho(\mathbf{r})$ in a local fashion, that is, ρ needs to be evaluated at one point in space at a time. For this

reason they are referred to as the Local Density Approximation to Density Functional Theory. This is actually a severe restriction, because even at the exchange level, the functional should be non-local, that is, it should depend on $\mathbf{r}$ and $\mathbf{r}'$ simultaneously. It is a much more difficult task to develop non-local exchange-correlation functionals.

The generalized gradient approximation (GGA)

In LDA, the exchange correlation energy density is a function of the local electron density, whereas local variations of the electron density are also important in elements condensed states. Generalized gradient approximation (GGA) was developed to improve accuracy of LDA. In a generalized gradient approximation, the functional depends on the density and its gradient,

$$E_{xc}^{GGA}[\rho] = \int \rho(\mathbf{r})\mathcal{E}_{xc}(\rho(\mathbf{r}), |\nabla\rho(\mathbf{r})|)d\mathbf{r} \tag{2.18}$$

Several GGA functionals like Perdew-Wang 1991 [12] and Perdew, Burke and Ernzerhof (PBE) [13] are the most popular. In comparison to LDA, GGA's tend to improve total energies, atomization energies, energy barriers and structural energy differences [13], while retaining all the correct features of LDA. GGA's expand and soften bonds, an effect that sometimes corrects and sometimes over-corrects the LDA prediction. Typically, GGA's favor density inhomogeneity more than LDA does.

2.3 General band-structure methods

To solve the single-particle Kohn-Sham Eqn. (2.13) and to obtain the eigenvalues (band structure) and eigenfunctions, a number of methods have been introduced. These methods are based on either k-space approach or real space approach and are applicable to both finite systems such as molecules or clusters as well as extended systems such as solids. For periodic solids, one usually exploits the translational periodicity and handles the solutions in k-space. For finite sized molecules and clusters also, k-space approach is used by constructing super-cell which imposes artificial periodicity in the system.

2.3.1 Basis sets

Regardless of whether it is k-space approach or real-space approach, one has to choose an appropriate basis set to expand the single-particle wave-functions and depending on the choice of basis functions, different schemes, therefore, can be broadly grouped into two categories: (*i*) methods using energy independent basis sets or fixed basis sets, like tight binding method using linear combination of atomic orbitals (LCAO) type basis[14], orthogonalized plane wave (OPW) method using plane waves orthogonalized to core states as the basis set[15], pseudopotential method using plane wave basis[16], and (*ii*) methods using energy dependent basis set, like cellular method[17], augmented plane wave (APW) method[18] and the Korringa-Kohn-Rostocker (KKR) Green's function method[19], which use partial waves as basis set. In this thesis, we mainly used pseudopotential method along with plane wave basis, as implemented in the Vienna *ab initio* simulation package (VASP)[20]. We also used full potential (L)APW+lo method, as implemented in the WIEN2k code [21] and also tight binding analysis in certain cases for better microscopic understanding of the problem. Structural optimization is performed using conjugate gradient or quasi-Newtonian dynamics.

2.3.2 Pseudopotential Method

It is well known that electrons in the outermost shell of atoms, the so called valence electrons, actively participate in determining the most of the chemical and physical properties of molecules and solids. This leads to the idea behind the pseudopotential theory. Here we will develop the basic concept of pseudopotential by a simple transformation of single-particle Kohn-Sham equation (2.13) for an atom where core and valence states are denoted as ψ^c and ψ^v respectively. A new set of single-particle valence states $\tilde{\phi}^v$ can be defined as

$$\psi^v(\mathbf{r}) = \tilde{\phi}^v + \sum_c \alpha_c \psi^c(\mathbf{r}) \tag{2.19}$$

where α_c are determined from the condition that ψ^v and ψ^c are orthogonal to each other *i.e* $\langle\psi^v|\psi^c\rangle = 0$ which gives α_c = - $\langle\psi^c|\tilde{\phi}^v\rangle$. Eqn. (2.13) then can be manipulated, with

the help of Eqn. (2.19), to

$$\left[T_S + V_{KS} + \sum_c (\epsilon^v - \epsilon^c)|\psi^c\rangle\langle\psi^c|\right]\tilde{\phi}^v = \epsilon^v\tilde{\phi}^v \tag{2.20}$$

with ϵ^c as the eigenvalue of the core state. Considering $V_R = \sum_c (\epsilon^v - \epsilon^c)|\psi^c\rangle\langle\psi^c|$ which is a repulsive potential operator (as $\epsilon^v > \epsilon^c$, making ϵ^v - ϵ^c positive), Eqn. (2.20) can be written as

$$[T_S + V_{PS}]\,\tilde{\phi}^v = \epsilon^v\tilde{\phi}^v \tag{2.21}$$

The operator

$$V_{PS} = V_{KS} + \sum_c (\epsilon^v - \epsilon^c)|\psi^c\rangle\langle\psi^c| \tag{2.22}$$

represents a weak attractive potential, denoting the balance between the attractive potential V_{KS} and the repulsive potential V_R, and is called a pseudopotential. While the new states $\tilde{\phi}^v$ obey a single-particle equation with a modified potential, but have the same eigenvalues ϵ^v as the original valence state ψ^v, are called pseudo-wavefunctions. These new valence states project out of the valence wavefunctions any overlap they have with the core wavefunctions, thereby having zero overlap with the core states. In other words, through the pseudopotential formulation, we have created a new set of valence states, which experience a weaker potential near the atomic nucleus, but the proper ionic potential away from the core region. Since it is this region in which the valence electrons interact to form bonds that hold the solid together, the pseudo-wavefunctions preserve all the important physics relevant to the behavior of the solid.

Since then several methods have been used to generate more accurate as well as more efficient pseudo-potentials, keeping the basic principles same. In norm-conserving pseudopotential [22], the all electron (AE) wave function is replaced by a soft nodeless pseudo (PS) wave function, with the restriction to the PS wave function that within the chosen core radius the norm of the PS wave function have to be the same with the AE wave function and outside the core radius both the wave functions are just identical. Good transferability of constructed pseudopotential requires a core radius around the outermost maximum of the AE wavefunction, because only then the charge distribution and moments of the AE wavefunctions are well produced by the PS wavefunctions. Therefore, for elements with strongly localized orbitals like first-row, 3d and rare-earth elements, the resulting

pseudopotentials require a large plane-wave basis set. To work around this, compromises are often made by increasing the core radius significantly beyond the outermost maximum in the AE wave-function. But this is usually not a satisfactory solution because the transferability is always adversely affected when the core radius is increased, and for any new chemical environment, additional tests are required to establish the reliability of such soft PS potentials. This was improved by Vanderbilt[23], where the norm-conservation constraint was relaxed and localized atom centered augmentation charges were introduced to make up the charge deficit. These augmentation charges are defined as the charge density difference between the AE and the PS wavefunction, but for convenience, they are pseudized to allow an efficient treatment of the augmentation charges on a regular grid. Only for the augmentation charges, a small cutoff radius must be used to restore the moments and the charge distribution of the AE wavefunction accurately.

The success of this approach is partly hampered by rather difficult construction of the pseudopotential. Later Blöchl [24] has developed the projector-augmented- wave (PAW) method, which combines idea from the LAPW method with the plane wave pseudopotential approach, and finally turns out computationally elegant, transferable and accurate method for electronic structure calculation of transition metals and oxides. Below we have outlined the idea behind the PAW method.

In the PAW method, the AE wavefunction Ψ_n (which is a full one-electron Kohn-Sham wavefunction) is derived from the PS wavefunction $|\tilde{\Psi}_n\rangle$ by means of a linear transformation:

$$|\Psi_n\rangle = |\tilde{\Psi}_n\rangle + \sum_i (|\phi_i\rangle - |\tilde{\phi}_i\rangle)\langle\tilde{p}_i|\tilde{\Psi}_n\rangle \tag{2.23}$$

The index i is a shorthand for the atomic site $\mathbf{R}$, the angular momentum numbers $L = (l, m)$ and an additional index k referring to the reference energy ϵ_{kl}. The all electron partial waves ϕ_i are the solutions of the radial Schrödinger equation for the isolated atom, and the PS partial waves $\tilde{\phi}_i$ are are equivalent to the AE partial waves outside a core radius r_c^l and match with value and derivative at r_c^l. The core radius r_c^l is usually chosen approximately around half the nearest-neighbor distance. The projector function $\tilde{p}_i$ for each PS partial wave localized within the core radius, obeys the relation $\langle\tilde{p}_i|\tilde{\phi}_i\rangle = \delta_{ij}$. Starting from Eqn. (2.23), it is possible to show that in the PAW method, the AE charge

density is given by

$$\rho(\mathbf{r}) = \tilde{\rho}(\mathbf{r}) + \rho^1(\mathbf{r}) - \tilde{\rho}^1(\mathbf{r}) \tag{2.24}$$

where $\tilde{\rho}$ is the soft pseudo-charge density calculated directly from the pseudo wavefunctions on a plane wave grid:

$$\tilde{\rho}(\mathbf{r}) = \sum_n f_n \langle \tilde{\Psi}_n | \mathbf{r} \rangle \langle \mathbf{r} | \tilde{\Psi}_n \rangle \tag{2.25}$$

The on-site charge densities ρ^1 and $\tilde{\rho}^1$ are treated on a radial support grids localized around each atom. They are defined as

$$\rho^1(\mathbf{r}) = \sum_{n,(ij)} f_n \langle \tilde{\Psi}_n | \tilde{p}_i \rangle \langle \phi_i | \mathbf{r} \rangle \langle \mathbf{r} | \phi_j \rangle \langle \tilde{p}_j | \tilde{\Psi}_n \rangle \tag{2.26}$$

and

$$\tilde{\rho}^1(\mathbf{r}) = \sum_{n,(ij)} f_n \langle \tilde{\Psi}_n | \tilde{p}_i \rangle \langle \tilde{\phi}_i | \mathbf{r} \rangle \langle \mathbf{r} | \tilde{\phi}_j \rangle \langle \tilde{p}_j | \tilde{\Psi}_n \rangle \tag{2.27}$$

It is to be noted that the charge density $\tilde{\rho}^1$ is exactly the same as $\tilde{\rho}$ within the augmentation spheres around each atom. In PAW approach, an additional density, called compensation charge density is added to both auxiliary densities $\tilde{\rho}$ and $\tilde{\rho}^1$ so that the multi-pole moments of the terms $\rho^1(\mathbf{r})$ - $\tilde{\rho}^1(\mathbf{r})$ in Eqn. (2.24) vanish. Thus the electrostatic potential due to these terms vanishes outside the augmentation spheres around each atom, just as is accomplished in LAPW method. Like density, the energy can also be written as a sum of three terms and by functional derivatives of the total energy, one can derive the expressions of Kohn-Sham equations.

2.3.3 (L)APW+lo method

Although the pseudopotential method is extremely useful, there are reasons why alternatives could be attractive. Unlike the plane wave if we could choose a basis that uses functions that does not require the introduction of a pseudopotential, then such a basis set will have to be more efficient. Here we will introduce one of the most accurate methods (L)APW+lo, which is LAPW in combination with APW.

Augmented Plane Wave (APW)

Before going into the (L)APW+lo method, it will be advantageous to discuss the APW method introduced by Slater [25]. Considering the behavior of electrons in space, when electrons are far away from the nuclei, they show the behavior of free electrons, and are then suitably described by plane waves. While close to the nuclei, electrons bind strongly to their nuclei, their behavior is quite as in a free atom and they could be described more efficiently by atomic like functions. Therefore, the whole space can be divided technically into two regions, (i) non-overlapping atomic spheres (called the Muffin-tin (MT) regions) and (ii) interstitial (I) region. Correspondingly, the potential in the whole space can be defined as

$$\begin{aligned} V(\mathbf{r}) &= V(\mathbf{r}) \qquad (\mathbf{r} \in \text{MT}) \\ &= constant \qquad (\mathbf{r} \in \text{I}) \end{aligned} \tag{2.28}$$

and, two types of basis sets are used in the two different regions,

$$\begin{aligned} \phi_{\mathbf{kn}}^{APW} &= \sum_{lm} A_{lm,\mathbf{k_n}} u_l(r,\epsilon_l) Y_{lm}(\hat{\mathbf{r}}) \qquad (\text{r} \in \text{MT}) \\ &= \frac{1}{\sqrt{\Omega}} e^{i\mathbf{k}_n \cdot \mathbf{r}} \qquad (\mathbf{r} \in \text{I}) \end{aligned} \tag{2.29}$$

where, Ω is volume of the unit cell. In the atomic spheres (MT), the wave functions are expanded by radial functions times spherical harmonics. u_l is the solution of the radial Schrödinger equation for a spherical potential [(V (r)] for energy ϵ_l,

$$-\frac{1}{r^2}\frac{d}{dr}(r^2\frac{du_l}{dr}) + [\frac{l(l+1)}{r^2} + V(r) - \epsilon_l] r u_l = 0 \tag{2.30}$$

Plane waves are used to build the wave function in the interstitial region (I). The coefficients A_{lm} in the atomic sphere expansion are determined by requiring that the wave functions in the MT and the interstitial regions match each other at the MT boundary. Thus, each plane wave is augmented by an atomic-like function in every atomic sphere and constitutes thus the basis set used to expand the wave function,

$$\Psi(\mathbf{r}) = \sum_n c_n \phi_{\mathbf{k}_n}(\mathbf{r}) \tag{2.31}$$

The main disadvantage in the APW method is that one can not get the eigenvalues from a single diagonalization due to the unknown parameter ϵ_l in Eq. 2.29. The exact ϵ_l value, which is what we want to know, is needed to describe the eigenstate $\Psi(\mathbf{r})$ accurately. Since this energy depends on the function $u_l(r,\epsilon_l)$, the resulting eigenvalue problem is non-linear in energy. One has to set a trial energy for ϵ_l, solve Eq. 2.30 to obtain the APW basis, set up the matrix elements, and compute the secular matrix determinant. If the eigen-energy does not equal ϵ_l, another trial energy must be chosen until the eigen-energy equals ϵ_l. This makes the APW method extremely inefficient.

LAPW

The non-linearity problem in the APW method was overcomed by Andersen using the linearized augmented plane wave method (LAPW) [26]. In his idea, the radial function u_l is expanded by a Taylor expansion around ϵ_l,

$$u_l(r,\epsilon_l) = u_l(r,\epsilon_l^1) + (\epsilon_l - \epsilon_l^1)\dot{u}_l(r,\epsilon_l^1) + O((\epsilon_l - \epsilon_l^1)^2) \tag{2.32}$$

where $\dot{u}_l = \frac{\partial u_l}{\partial \epsilon_l}$. In this case the radial function error is second order, and the energy error is of fourth order. When ϵ_l^1 is set near ϵ_l, the radial radial function and energy errors are negligible. Formulation of the LAPW basis set is obtained by substituting Eq. 2.32 into Eq. 2.29,

$$\begin{aligned} \phi_{\mathbf{kn}}^{LAPW} &= \sum_{lm}[A_{lm,\mathbf{kn}}u_l(r,\epsilon_l^1) + B_{lm,\mathbf{kn}}\dot{u}_l(r,\epsilon_l^1)]Y_{lm}(\hat{\mathbf{r}}) \qquad (\mathbf{r} \in \text{MT}) \\ &= \frac{1}{\sqrt{\Omega}}e^{i\mathbf{k_n}\cdot\mathbf{r}} \qquad (\mathbf{r} \in \text{I}) \end{aligned} \tag{2.33}$$

The basis set in the interstitial region is the same as in the APW method, but in the MT spheres, the basis functions not only depend on u_l, but also on its energy derivative, $\dot{u}_l$. It is very clear that the LAPW method is thus more flexible than the APW in the MT spheres. To know the exact value for ϵ_l as in the APW is not important anymore. For a fixed value of ϵ_l^1, the modified basis functions (Eq. 2.32) provide the extra flexibility to cover a large energy region around this linearization energy. In order to determine both

$A_{lm,\mathbf{k_n}}$ and $B_{lm,\mathbf{k_n}}$, the functions in the MT spheres are required to match the plane wave function both in value and in slope at the sphere boundary. However, the continuous derivatives require higher plane wave cutoffs to achieve a given level of convergence.

LAPW with Local Orbital (LAPW+LO)

Electrons can be divided into two types, depending on whether or not electrons in an atom participate in the chemical bonding with other atoms. One type of electrons are core electrons, which are extremely bound to their nucleus and are thus entirely localized in the MT sphere. The corresponding states are called core states. The other type of electrons are valence electrons, which are leaking out of the MT sphere and bond with other atoms. However, for many elements, the electrons cannot be clearly distinguished like that. Some states are neither constrained in the core states, nor lie in the valence states and are correspondingly termed semi-core states. They have the same angular quantum number l as the valence states but with lower principal quantum number n. When applying LAPW on these states, it is thus hard to use one ϵ_l^1 to determine the two same l in Eq. 2.33. The dilemma is solved by introducing local orbitals (LO)[27], which are defined as

$$\begin{aligned} \phi_{lm}^{LO}(r) &= [A_{lm}u_l(r,\epsilon_l^1) + Blm\dot{u}_l(r,\epsilon_l^1) + C_{lm}u_l(r,\epsilon_l^2)]Y_{lm}(\hat{\mathbf{r}}) \qquad (\mathbf{r} \in \text{MT}) \\ &= 0 \qquad (\mathbf{r} \in \text{I}) \end{aligned} \tag{2.34}$$

Each local orbital is zero in the interstitial region and other atom's MT sphere. The three coefficients A_{lm}, B_{lm} and C_{lm} can be determined by requiring the LO to have both zero value and zero slope at the MT boundary and be normalized.

APW+lo

It has been realized that the standard LAPW method is not the most efficient way to linearize Slaters APW method [28]. Instead, the basis set of the introduced APW+lo [28, 29] method is also energy independent and still has the same basis size as the original

APW method. In order to achieve that a new local orbital (lo) is added, which is different from the LOs used to describe semicore states to gain enough variational flexibility in the radial basis functions. The lo definition is,

$$\begin{aligned} \phi_{lm}^{lo}(\mathbf{r}) &= [A_{lm}u_l(r,\epsilon_l^1) + B_{lm}\dot{u}_l(r,\epsilon_l^1)]Y_{lm}(\hat{\mathbf{r}}) \qquad (\mathbf{r} \in \text{MT}) \\ &= 0 \qquad (\mathbf{r} \in \text{I}) \end{aligned} \tag{2.35}$$

The two coefficients A_{lm} and B_{lm} are determined by normalization, and by requiring that the local orbital has zero value at the Muffin-tin boundary. The advantage of the APW+lo method is that it has the same small basis set size as the APW method, and has the same accuracy compared to the LAPW method.

As mentioned by Madsen *et al.* [28], it is also possible to use a hybrid basis set, LAPW in combination with APW [(L)APW+lo], and treat the physically important orbitals by the APW+lo method, but the polarization l-quantum numbers with LAPW.

Full Potential (L)APW+lo Method

In Eq. 2.28, we supposed the potential is constant in the interstitial region and spherical in the MT region. The accuracy of (L)APW+lo method can be further improved by considering the full potential (FP), and expand it similar to the wave functions,

$$\begin{aligned} V(r) &= \sum_{lm} V_{lm}(r)Y_{lm}(\hat{r}) \qquad (\mathbf{r} \in \text{MT}) \\ &= \sum_{\mathbf{G}} V_{\mathbf{G}} e^{i\mathbf{G}\cdot\mathbf{r}} \qquad (\mathbf{r} \in \text{I}) \end{aligned} \tag{2.36}$$

This is also called non-muffin-tin correction. In this case, the radial function u_l in Eq. 2.30 is not the exact solution inside the MT sphere. It should be evaluated for the true MT potential.

WIEN2k Code

The WIEN2k code [21] is based on the FP-(L)APW+lo method. The code can only be applied to systems with periodic boundary conditions and is therefore mainly used for crystal calculations. The WIEN2k code has two main parts. One is the initialization where it checks if MT spheres overlap, generate a new structure file according to its space group, detect its symmetry operations, generate a k-mesh in its Brillouin zone, and get the input trial density. The other one is the self-consistency cycle where it calculates the potential used in the Kohn-Sham equation, diagonalizes the Hamiltonian and overlap matrices and generates eigenvalues and eigen-vectors, integrates all valence states and obtains the valence electron density (ρ_{val}), solves the atomic calculation and gets the core electron density (ρ_{core}), mixes the two electron densities with the old total electron density (ρ_{old}) and gets the new total electron density (ρ_{new}). Thereafter it checks if the properties (ρ_{new}, or total energy, or forces ...) of the system are converged, and either stops the self-consistency cycle or starts a new.

2.3.4 The tight-binding method (LCAO method)

For a periodic system, the tight-binding Hamiltonian is given by

$$\mathbf{H} = \sum_{il_1\sigma} \epsilon_{l_1} a^{\dagger}_{il_1\sigma} a_{il_1\sigma} + \sum_{ij} \sum_{l_1,l_2,\sigma} (t^{l_1 l_2}_{ij} a^{\dagger}_{il_1\sigma} a_{jl_2\sigma} + h.c.) \tag{2.37}$$

where, the electron with spin σ is able to hop from the orbitals labelled l_1 with onsite energies equal to ϵ_{l_1} in the i^{th} unit cell to those labelled l_2 in the j^{th} unit cell, with the summations l_1 and l_2 running over all the orbitals considered on the atoms in a unit cell, and i and j over all the unit cells in the solid. Thus, any orbital in the solid can be defined with the two indices, i and l_1, henceforth referred to as the set (i, l_1). The hopping interaction strength ($t^{l_1 l_2}_{ij}$) depends on the nature of the orbitals involved as well as on the geometry of the lattice [14]. Since the hopping integrals are expected to fall off rapidly with distance [30], it is sufficient to consider those terms in the Hamiltonian which allow the electron to hop to orbitals on nearest neighbor atoms. Further, since the Hamiltonian is independent of the spin (σ), in the rest of the discussion the spin indices

of the Fermion operators will not be retained explicitly. The Hamiltonian can be cast into the momentum space by a Fourier transformation of the operators given by

$$a^{\dagger}_{il_1} = \frac{1}{\sqrt{N}} \sum_k a^{\dagger}_{kl_1} e^{i\mathbf{k}.\mathbf{r}_{il_1}}$$

so that,

$$\begin{aligned}
\mathbf{H} &= \sum_{il_1} \epsilon_{l_1} a^{\dagger}_{il_1} a_{il_1} + \sum_{<ij>} \sum_{l_1,l_2} (t^{l_1 l_2}_{ij} a^{\dagger}_{il_1} a_{jl_2} + h.c.) \\
&= \frac{1}{N} \sum_{il_1} \sum_{kk'} \epsilon_{l_1} a^{\dagger}_{kl_1} a_{k'l_1} e^{i\mathbf{k}.\mathbf{r}_{il_1}} e^{-i\mathbf{k}'.\mathbf{r}_{il_1}} \\
&\quad + \frac{1}{N} \sum_{<ij>} \sum_{l_1,l_2,k,k'} (t^{l_1 l_2}_{ij} a^{\dagger}_{kl_1} a_{k'l_2} e^{i\mathbf{k}.\mathbf{r}_{il_1}} e^{-i\mathbf{k}'.\mathbf{r}_{jl_2}} + h.c.)
\end{aligned}$$

An advantage of this representation is that the Hamiltonian breaks into distinct blocks for each $\mathbf{k}$ value, thereby simplifying the problem. In order to realize this, we first define a set of vectors $\mathbf{R}^{l_1 l_2}_{\alpha}$ for the orbital (i, l_1), that connect it to the orbitals (j, l_2) on nearest neighbor atoms, $\mathbf{r}_{jl_2} = \mathbf{r}_{il_1} + \mathbf{R}^{l_1 l_2}_{\alpha}$. As a result of the periodicity of the lattice, the set of vectors $\mathbf{R}^{l_1 l_2}_{\alpha}$ are the same for every (i, l_1) independent of the unit cell index, i. As the hopping integrals, between orbitals (i, l_1) and (j, l_2) depend only on the vector $\mathbf{R}^{l_1 l_2}_{\alpha}$ connecting the two orbitals involved, the quantities $t^{l_1 l_2}_{ij}$ in the Hamiltonian can be replaced with $t^{l_1 l_2}_{\alpha}$. Therefore, the simplified Hamiltonian becomes,

$$\begin{aligned}
\mathbf{H} &= \frac{1}{N} \sum_{il_1} \sum_{kk'} \epsilon_{l_1} a^{\dagger}_{kl_1} a_{k'l_1} e^{i\mathbf{k}.\mathbf{r}_{il_1}} e^{-i\mathbf{k}'.\mathbf{r}_{il_1}} \\
&\quad + \frac{1}{N} \sum_{\alpha} \sum_{i,l_1,l_2,k,k'} (t^{l_1 l_2}_{\alpha} a^{\dagger}_{kl_1} a_{k'l_2} e^{i\mathbf{k}.\mathbf{r}_{il_1}} e^{-i\mathbf{k}'.(\mathbf{r}_{il_1} + \mathbf{R}^{l_1 l_2}_{\alpha})} + h.c) \\
&= \frac{1}{N} \sum_{il_1} \sum_{kk'} \epsilon_{l_1} a^{\dagger}_{kl_1} a_{k'l_1} e^{i(\mathbf{k}-\mathbf{k}').r}_{il_1} + \frac{1}{N} \sum_{\alpha} \sum_{i,l_1,l_2,k,k'} (t^{l_1 l_2}_{\alpha} a^{\dagger}_{kl_1} a_{k'l_2} e^{i(\mathbf{k}-\mathbf{k}').\mathbf{r}_{il_1}} e^{-i\mathbf{k}'.\mathbf{R}^{l_1 l_2}_{\alpha}} + h.c) \\
&= \sum_{l_1} \sum_{kk'} \epsilon_{l_1} a^{\dagger}_{kl_1} a_{k'l_1} \delta(k - k') + \sum_{\alpha} \sum_{l_1,l_2,k,k'} (t^{l_1 l_2}_{\alpha} a^{\dagger}_{kl_1} a_{k'l_2} \delta(k - k') e^{-i\mathbf{k}'.\mathbf{R}^{l_1 l_2}_{\alpha}} + h.c.) \\
&= \sum_{l_1} \sum_{k} \epsilon_{l_1} a^{\dagger}_{kl_1} a_{kl_1} + \sum_{\alpha} \sum_{kl_1 l_2} (t^{l_1 l_2}_{\alpha} a^{\dagger}_{kl_1} a_{kl_2} e^{-i\mathbf{k}.\mathbf{R}^{l_1 l_2}_{\alpha}} + h.c.)
\end{aligned}$$

From the above expression, it is seen that the Hamiltonian involves terms connecting different orbitals which may be on the same or on different atoms at a $\mathbf{k}$ point. Thus, the problem of electronic structure determination reduces to one of solving the Hamiltonian at each $\mathbf{k}$ point in the Brillouin zone. This has to be performed numerically in most cases,

with the size of the matrix equal to the total number of orbitals considered on all the atoms in the unit cell.

The eigenfunctions of the Hamiltonian, $\mathbf{H}$, correspond to linear combinations of the atomic orbitals, $\phi_j(r)$, given by,

$$\Psi_i(r) = \sum_j x_{ij}\phi_j(r)$$

It is seen that the different atomic orbitals located on neighboring atoms are not necessarily orthogonal to each other. However, since the formalism of second quantization requires an orthogonal basis for the proper definition of fermion creation and annihilation operators and their associated Fock space, the Löwdin transformation [31] which is outlined below has been used to transform the orbitals into an orthogonal basis set. If the spatial overlap between orbitals on neighboring atoms is given by

$$S_{\alpha\beta} = \int dr \phi^*_\alpha(r)\phi_\beta(r) - \delta_{\alpha\beta}$$

it is then seen that the coefficients x_{ij} must satisfy the matrix equation

$$\mathbf{Hx} = \mathbf{(1+S)xE}$$

where,

$$\mathbf{x}^\dagger\mathbf{(1+S)x} = \mathbf{1}$$

involving $\mathbf{x}$ and $\mathbf{E}$, which are the matrices formed by the expansion coefficients x_{ij} and the eigenvalues E_j respectively. In order to represent the Hamiltonian in an orthogonal basis, given by $\mathbf{c}$, the matrix $\mathbf{x}$ is replaced by $\mathbf{c}$ according to the relation,

$$\mathbf{x} = \mathbf{(1+S)^{-1/2}c}$$

By this substitution, the eigenvalue problem is reduced to the form,

$$\mathbf{H'c} = \mathbf{Ec}$$
$$\mathbf{c}^\dagger\mathbf{c} = 1$$

where $\mathbf{H'}$ is the Hamiltonian in the orthogonal basis. $\mathbf{H'}$ is related to the Hamiltonian set up in the non-orthogonal basis by the expression,

$$\mathbf{H'} = \mathbf{(1+S)^{-1/2}H(1+S)^{-1/2}}$$

In order to evaluate $\mathbf{(1+S)}^{-1/2}$, the matrix $\mathbf{(1+S)}$ is first diagonalized by a unitary transformation $\mathbf{U}$ to yield a diagonal matrix $\mathbf{D}$,

$$\mathbf{U}^{\dagger}(\mathbf{1}+\mathbf{S})\mathbf{U} \;=\; \mathbf{D}$$

As the eigenvalues of $\mathbf{(1+S)}$ are positive, a new matrix $\mathbf{D}^{-1/2}$ can be formed from $\mathbf{D}$ by replacing each diagonal element by its inverse square root. So, $\mathbf{(1+S)}^{-1/2}$ can be evaluated using the following relation

$$(\mathbf{1}+\mathbf{S})^{-\mathbf{1/2}} = \mathbf{U}\mathbf{D}^{-\mathbf{1/2}}\mathbf{U}^{\dagger}$$

Once $\mathbf{(1+S)}^{-1/2}$ is known, the Hamiltonian can be set up in the orthogonal basis and solved.

Bibliography

[1] M. Born and J. R. Oppenheimer, "Zur Quantentheorie der Molekeln", Ann. Physik **84**, 457 (1927).

[2] D. R. Hartree, "The wave mechanics of an atom with non-coulombic central field: parts I, II, III", Proc. Cambridge Phil. Soc. **24**, 89, 111, 426 (1928).

[3] V. Fock, "Naherungsmethode zur Losung des quanten-mechanischen Mehrkorper-probleme", Z. Phys. **61**, 126 (1930).

[4] J. C. Slater, "The Theory of Complex Spectra", Phys. Rev. **34**, 1293 (1929).

[5] P. Hohenberg and W. Kohn, Phys. Rev. **136**, B864 (1964).

[6] W. Kohn and L. J. Sham, Phys. Rev. **140**, A1133 (1965).

[7] E. Kaxiras, Atomic and Electronic Structure of Solids; Cambridge University Press, UK, p. 62-65, (2003).

[8] E. P. Wigner, Phys. Rev. **46**, 1002 (1934); see also R.M. Dreizler and E.K.U. Gross, *Density Functional Theory*, Springer, New York (1990).

[9] L. Hedin and B.I. Lundqvist, J. Phys. C **4**, 2064 (1971).

[10] J. P. Perdew and A. Zunger, Phys. Rev. B **23**, 5048 (1981).

[11] D. M. Ceperley and B. J. Alder, Phys. Rev. Lett. **45**, 566 (1980).

[12] J.P. Perdew and Y. Wang, Phys. Rev. B **45**, 13244 (1992).

[13] J. P. Perdew, K. Burke, and M. Ernzerhof, Phys. Rev. Lett. **77**, 3865 (1996).

[14] J. C. Slater and G. F. Koster, Phys. Rev. **94**, 1498 (1954).

[15] W. C. Herring, Phys. Rev. **57**, 1169 (1940); W. C. Herring and A. G. Hill, Phys. Rev. **58**, 132 (1940).

[16] J. C. Phillips and L. Kleinman, Phys. Rev. **116**, 287 (1959).

[17] E. P. Wigner and F. Seitz, Phys. Rev. **46**, 509 (1934).

[18] T. L. Loucks, *Augmented Plane Wave Methods*, (Benjamin, New York, 1967).

[19] J. Korringa, Physica **13**, 392 (1947); J. Korringa, Phys. Rev. **238**, 341 (1994).

[20] G. Kresse and J. Hafner, Phys. Rev. B **47**, 558 (1993); G. Kresse and J. Furthmuller, Phys. Rev. B **54**, 11169 (1996).

[21] P. Blaha, K. Schwartz, G. K. H. Madsen, D. Kvasnicka and J. Luitz; An Augmented Plane Wave + Local Orbitals Program for calculating crystal properties (K. Schwarz, Techn. University Wien, Austria, 2001), ISBN 3-9501031-1-2.

[22] D. R. Hamann, M. Schlüter, and C. Chiang, Phys. Rev. Lett. **43**, 1494 (1979).

[23] D. Vanderbilt, Phys. Rev. B **41**, 7892 (1985).

[24] P. E. Blöchl, Phys. Rev. B **50**, 17953 (1994).

[25] J. C Slater, Phys. Rev. **51**, 846 (1937); J. C Slater, Phys. Rev. **81**, 385 (1951).

[26] O. K. Andersen, Phys. Rev. B **12**, 3060 (1975).

[27] D. J. Singh, Phys. Rev. B **43**, 6388 (1991).

[28] G. K. H. Madsen, P. Blaha, K. Schwarz, E. Sjöstedt, L. Nordström, Physical Review B **64**, 195134 (2001).

[29] E. Sjöstedt, L. Nordström, D. J. Singh, Solid State Commun. **114**, 15 (2000)

[30] Walter A. Harrison, *Electronic Structure and Properties of Solids* (Dover, 1989).

[31] Per-Olov Löwdin, J. Chem. Phys. **18**, 365 (1950).

Chapter 3

Role of semicore Ga d states in GaX semiconductors

Semicore states present in Ga - based semiconductors play an important role in determining the properties of these materials. As they are not too deep, they are chemically active and play a role in modifying the band gap, band offsets and in some cases also the cohesive properties and the lattice constant. In this chapter we examine three aspects.

(a) Modification of equilibrium properties such as lattice constant.

(b) The interaction of semicore states with the valence and conduction band states.

(c) Modification of the valence band offsets with lattice matched materials.

3.1 Role of semicore Ga d states in modification of equilibrium properties

3.1.1 Introduction

The semiconductor industry has used silicon as its basic building block since the beginning. Recently the focus has shifted to other materials with the aim of harnessing their multi-functionality to construct new generation devices. An important class of materials that have received considerable attention in this context are the nitrides. The bulk ni-

[1]This section is based on the following paper:
R. Cherian and P. Mahadevan, *Bulk and nanoscale GaN: Role of Ga d states*, Phys. Rev. B. **76**, 075205 (2007).

trides formed with group III elements show interesting physical properties such as large piezoelectric response [1]. However, the dilute nitrides where one observes dramatic effects by the introduction of a small amount of nitrogen to replace the anion sites have received a lot of attention in recent times. Alloys of GaInNAs have been recognized as important materials for the development of long wavelength solid-state lasers emitting within the fibre-optic communication wavelength window (1.3 to 1.55 μm) [2]. There are also theoretical predictions that exist which suggest that these materials could also be used to increase the efficiency of multijunctional solar-cells [3]. In the case of GaNP alloys, the crossover from an indirect to a direct band gap induced by N incorporation [4] promises high radiative efficiency, whereas a N-induced reduction in the lattice constant offers a possibility of lattice matching between optically efficient III-V compounds and Si wafers, desirable for the integration of the two technologies [5]. GaInNAs semiconductor quantum dots with dilute amount of nitrogen substitutional impurities are promising candidates for the active region in the next generation of optoelectronic devices [6]. Transition metal doped GaN has been found to exhibit ferromagnetism at room temperature [7] which could make these materials useful in the emerging area of spintronics.

With recent advances in computational power, theory and specifically *ab-initio* density functional theory has played an important role in the design of materials with tailor-made properties [8]. Calculations for the systems of interest in the context of the nitrides - dilute nitrides as well as quantum dots, are usually performed for periodic systems considering large and representative supercells. These are computationally demanding within an *ab-initio* approach. It is therefore useful to have accurate and reasonable approximations which decrease the computational cost. In this context it was shown that enormous saving in terms of computational time may be made if one used ultrasoft pseudopotentials developed by Vanderbilt [9]. Further improvements were made by Blöchl [10] who combined the ideas of soft pseudopotentials and all electron methods like LAPW (linearised augmented plane wave) within an elegant framework called the projected augmented wave (PAW) method. In this work we have examined the bulk electronic structure of GaN using PAW potentials. The results have been compared with those obtained using ultrasoft pseudopotentials. The calculated equilibrium lattice constants are within 0.3 % of each other.

The role of the Ga 3d states in determining the physical properties of GaN has received considerable attention over the past two decades. Unlike in the case of other Ga-V semiconductors one finds that in GaN the Ga 3 d core states are not chemically inert. One finds a strong overlap in energy between the semi-core Ga 3d states as well as the N 2s states. Fiorentini *et al.* [11] pointed out that ignoring this interaction would have consequences on both the cohesive energy as well as the equilibrium lattice constant deduced theoretically. According to the variational principle, neglect of any relaxation of the semi core levels would increase the total energy, an effect which would disappear in the limit of well separated atoms in the solid. Further, the overlap of the core states with the valence states on the same atom results in a nonlinear exchange interaction. Finally the interaction of core states with core states on the neighboring atom results in the neglect of closed shell repulsion. This has the effect of an increase in the kinetic energy when the cores on neighboring atoms are made orthogonal. If this contribution is neglected, the cohesive energy comes out too large and the lattice constant too small. The net effect which they found was that the lattice constant when Ga 3d states were neglected was almost 4 % smaller than that obtained with the Ga 3d states included within LDA. An additional effect of the neglect of the Ga 3d states is observed in the modification of the band gap. The Ga 3d states that split into states with t_2 and e symmetry in the tetrahedral crystal field of the N neighbors, interact with the valence band derived levels with the same symmetry. This interaction pushes the valence band maximum to higher energies and therefore decreases the band gap of GaN in comparison to treatments in which Ga 3d states were a part of the core. Recent studies by Bouhafs *et al.* [12] on the GaN semiconductor, at a fixed lattice constant, also confirm that the band gap decreases in a treatment in which the Ga 3d states were included in the valence.

PAW potentials give us the freedom to toggle between using the Ga 3d in the valence and in the core and allows us to simultaneously examine the modifications in the electronic properties and more importantly the structural and cohesive properties. The implementation of PAW that we use allows for core-valence interaction within a frozen core approximation. We first review the existing understanding for bulk GaN using PAW potentials. The equilibrium lattice constant computed by us within pseudopotential calculations with and without Ga 3d in the valence differ by less than 0.3 % using ultrasoft

pseudopotentials. The deviations between the two approaches is similar when we use PAW potentials. All earlier studies have found that the lattice constant without Ga $3d$ in the valence is underestimated within the pseudopotential approach, and our results using ultrasoft pseudopotentials are consistent with this observation. The PAW approach gives us a different trend, however, and we attribute that to the treatment of core-valence exchange interaction. Changing the anion to P and then As, we find an overestimation of the lattice constant when Ga $3d$ states are not included as a part of the valence. The difference between the theoretical lattice constants, however, decreases as we go from GaN to GaAs. A considerable portion of the literature has commented on the Ga $3d$ admixture in the valence band of GaN. To explicitly examine this, we have plotted the Ga d partial density of states for both cases - with and without Ga $3d$ states in the valence. The Ga d contribution in the valence band arising from semi-core valence interaction accounts for 51% of the total d admixture. This ratio decreases as we move to GaP and GaAs.

Having studied the bulk limit of GaN, we examined small representative nanocrystals of GaN. Quantum confinement effects modify the energy of the valence band maximum and conduction band bottom of the semiconductor nanoparticles, and should decrease the separation between the semi core Ga $3d$ states and the valence band maximum. This results in an increased interaction strength and therefore an enhanced $3d$ contribution in the valence band. Comparing the equilibrium lattice constant with and without Ga $3d$, we find a difference of $\sim 1\%$ for nanocrystals with an average diameter of ~ 10 Å.

3.1.2 Methodology

The electronic structure of bulk zinc-blende GaN, GaP and GaAs was calculated using a plane wave pseudopotential implementation of density functional theory within VASP Ultrasoft pseudopotentials as well as PAW potentials [13] have been used. Calculations have been performed with and without Ga $3d$ states included in the valence band. GGA-PW91 approximation [14] has been used for the exchange. A dense k-points grid of 8x8x8 within Monkhorst Pack scheme has been used. The energy cutoffs used for the kinetic energy of the plane waves used in the basis was 500 eV for GaN, 337.5 eV for GaP and 260.9 eV for GaAs. The calculations for GaP and GaAs which did not include the Ga $3d$

states as a part of the valence band had a cutoff of 353.4 eV. The convergence with respect to k-points was tested by increasing the mesh density from 8x8x8 to 10x10x10. The total energies changed by 0.02 meV. The equilibrium lattice constant has been determined by fitting the energy variation with volume to the Murnaghan equation of state [15]. An analysis of the electronic structure was performed using the density of states calculated using the tetrahedron method. The wavefunctions were projected onto atom-centered spherical harmonics that were integrated over spheres of radii 1.2 Å for Ga, P and As in GaP, GaAs and GaN and 0.95 Å for N in GaN for the evaluation of the density of states.

We also examined the electronic structure of GaN nanocrystals in the nanocrystal limit by considering representative nanocrystals. We construct nanocrystals by cutting a spherical fragment of a bulk crystal, which has an underlying geometry of the zinc-blende structure. Now to define a spherical nanocrystal in this way we need to specify the center and the radius (Ref. Chapter 6). In our studies the nanocrystal is centered on the Ga atom, and then the nanocrystals are generated by considering a spherical cut off radius. These will have a T_d point group symmetry. The smallest nanocrystal considered had 4 atoms around the central Ga atom, and since it had just one layer around the central atom for simplicity we denote this nanocrystal as n=1 (where n stands for the number of layers around the central atom). The next size nanocrystal which was considered in our study had 3 layers around the central atom (n=3), having in total 13 Ga and 16 N atoms.

The average equilibrium lattice constant of the nanocrystals were calculated (refer section 6.2). Again as done in the case of the bulk, the average equilibrium lattice constant with and without Ga $3d$ states in the valence were determined. Features of the electronic structure are examined by calculating the density of states broadening each eigenvalue with a gaussian of full width at half maximum of 0.1 eV.

3.1.3 Results and Discussion

As discussed earlier , the near resonance of the Ga $3d$ states with the N $2s$ states results in a strong deviations in calculated structural properties in treatments where Ga $3d$ states are not included as a part of the valence band. These considerations prompted us to carry out calculations using PAW potentials, allowing us to toggle between using Ga d

in the valence, and merely as a part of the core. The results are given in Table I. For the comparison the results using ultrasoft potentials were also calculated (Table I). The error in the calculated lattice constant with and without d states in the valence were $\sim$ 0.03-0.04 Å (around 1%). A smaller error in the calculated lattice constant is also found when one used ultrasoft potentials with and without Ga d in the valence. These results suggest that possibly the large deviations in the equilibrium lattice constant found earlier are specific to the choice of the method. The trends in the lattice constant with and without d are in opposite directions when we used ultrasoft potentials and when we use PAW potentials. As the treatment of the core electrons are meaningful in the PAW calculations, we examined these calculations in greater detail. The equilibrium lattice constant is predicted to be smaller when Ga d states are included in the valence. This is a suprising result at first as Ga d states interact primarily with the filled N s and N p states in the valence band. Hence, naively one does not expect there to be any energy gain as a result of the interaction. However the valence and conduction band electrons feel the presence of the Ga $3d$ electrons in the semi-core. Our analysis in section 3.2 has shown the manner in which the Ga d states interact with valence band states. By artificially moving the Ga d states to deeper energies using a U on the $3d$ states within the framework of LDA+U, we simulated the situations of having / not having chemically active Ga $3d$ states. Gradually moving the Ga $3d$ states to deeper energies we find a redistribution of charge on Ga related levels. This in turn leads to a modification of the interaction between the anion p states and cation states. The altered interaction strengths can therefore explain why there should be any modification of the total energy and therefore the lattice constant of these systems with and without the inclusion of Ga $3d$ states in the valence.

Moving down the Group V series of the periodic table to heavier anions instead of Nitrogen, we find a similar trend. The theoretical lattice constant (Table II) calculated within the PAW method in the absence of $3d$ in the valence for Ga are consistently larger than when the $3d$ states are treated as a part of the valence. With increasing atomic number on the anion, the Ga $3d$ states are pushed deeper into the valence band, and hence their interaction with the anion p states making up the valence band are weaker. Hence the deviation in the equilibrium lattice constant with the two choice of basis becomes

smaller as we go from GaP to GaAs. While the deviations in the theoretical lattice constant are small, the errors in the theoretical bulk modulus are significant in the case of GaN, while they are small in the case of GaP and GaAs.

The significant interaction between the Ga $3d$ states with the N p states comprising the valence band is usually measured by plotting the Ga d admixture in the valence band. Our choice of basis, however, allows us to distinguish the $3d$ admixture from the $4d$ admixture, which one believes is not strongly affected by changing the basis and is largely additive. The total as well as the s, p, d contribution to the Ga and N partial density of states have been plotted (Fig. 3.1) for GaN with the $3d$ states on the Ga treated as a part of the core. The zero of the energy axis has been set to be the valence band maximum. The N s states contribute at around -11.5 eV while the N p states contribute between 0-6 eV. The band gap is calculated to be 1.47 eV within the present calculation. Ga s and p states are strongly intermixed in the conduction band. As is evident from the middle panel, there is a small admixture of the Ga $4d$ states within the states comprising the valence band (especially 0-3 eV below the valence band maximum).

A similar plot (Fig. 3.2) has been made from the calculations which include Ga $3d$ states in the valence. The gross features of the electronic structure remain unchanged. The Ga $3d$ states are found to lie at higher energies in these calculations than the N s states. Significant interaction is found to exist between the semi core N s and Ga d states because of their close proximity in energy. The Ga d states in the semi core also interact with the N p states. The band gap in the current calculation is found to be 1.56 eV, therefore increased by $\sim$ 90 meV from the value obtained when the Ga $3d$ states were a part of the core. It should be noted that the density of states have been plotted at the theoretical equilibrium lattice constants given in Table 3.1. Had we fixed the lattice constant in the two calculations, we would have seen a reduction in the band gap when the Ga $3d$ states were included in the basis as observed earlier [12]. Here we have the additional effect of a decreased lattice constant and so we find a larger band gap.

We have also examined the change in Ga d contribution in the valence and conduction band with the two choice of basis. This is plotted in Fig. 3.3. Assuming that the Ga $4d$ admixture in the valence band is unchanged when Ga $3d$ states are included in the

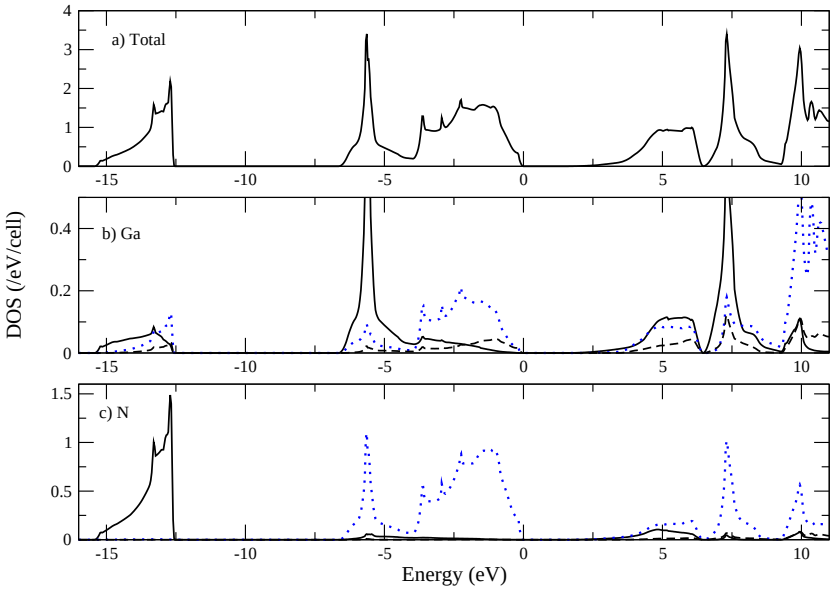

Figure 3.1: (a) The total DOS , (b) Ga s (solid line), p (dotted line) and d(dashed line) projected density of states and (c) N s (solid line), p (dotted line) and d(dashed line) projected density of states for GaN using PAW potentials with no Ga-d. The zero of energy corresponds to the valence band maximum.

basis, the results are quite surprising. We find that the Ga $3d$ admixture in the valence band accounts for around 51% of the total Ga d component in the valence band. This is contrary to the belief that the Ga d contribution in the valence band is a measure of the semi-core valence interaction. Similar results are plotted for GaP and GaAs in Figs. 3.4 and 3.5 at their theoretical equilibrium lattice constants (Table 3.2). The d admixture gradually decreases as we go from GaN to GaP and finally to GaAs, and is mainly from interaction of the anion p states with the Ga $4d$ states in the conduction band. The Ga $3d$ admixture in the valence band accounts for around 42% and 23% of the total Ga d component in the valence band for GaP and GaAs respectively.

As GaN showed significant interaction between the Ga $3d$ states with the N p sates, we examined the modifications in the interactions and consequent implications when one

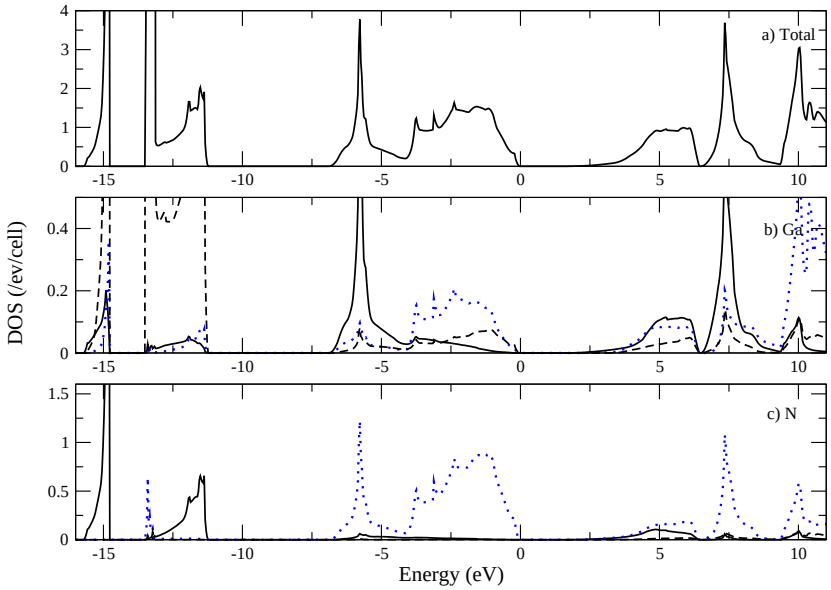

Figure 3.2: (a) The total DOS , (b) Ga s (solid line), p (dotted line) and d(dashed line) projected density of states and (c) N s (solid line), p (dotted line) and d(dashed line) projected density of states for GaN using PAW potentials with Ga-d. The zero of energy corresponds to the valence band maximum.

went down to the nanoregime. As is well known, quantum confinement effects modify the position of the levels which move from their positions in the bulk solid to deeper energies at a rate which is inversely proportional to the effective mass of the level. Since the d states would move more slowly than the states comprising the valence band maximum, with decreased nanocrystal size, one expects the Ga d - N p seperation to decrease, and hence interaction to increase. Indeed this is found to be the case, and one measures the enhancement in the p-d strength by the relative error that one finds in computed quantities such as the lattice constant. In Table 3.3 we provide the optimized lattice constants for the two representative nanocrystals. These are found to be smaller than that for the bulk GaN. As the size of the nanocrystal decreases we find the the relative position of the Ga $3d$ from the valence band maximum to decrease, for the smallest nanocrystal (n=1) the

Table 3.1: The lattice constant, a_0 (Å) and bulk modulus, B (G Pa), variation in GaN with different potentials.

	PAW		USP	
	no Ga-d	with Ga-d	no Ga-d	with Ga-d
a_0	4.584	4.545	4.513	4.530
B	183.63	172.59	177.33	170.03

Table 3.2: Calculated structural properties for GaX, X= N, P and As. The lattice constant a_0 is in Å, B is the bulk modulus in G Pa.

	PAW			
	no Ga-d		with Ga-d	
	a_0	B	a_0	B
GaN	4.584	183.63	4.545	172.59
GaP	5.532	78.74	5.504	76.70
GaAs	5.759	62.47	5.746	61.28

seperation is reduced by 2 eV and for the n=3 case it is reduced by 0.6 eV, with respect to the bulk separation value, resulting in the increased *p-d* interaction which modifies the lattice constant. With the two choices of basis we also examined the changes in the Ga *d* and N *p* contribution in the valence and conduction band. Around the conduction band region the changes resulting from the choice of the two basis were small. For the two nanocrystal cases (n=1 and n=3) the density of states around the valence band region are shown in Fig. 3.6 . The zero of the energy corresponds to the valence band maximum. Here the Ga 3*d* admixture in the valence band accounts for around 53% for the n=1 case and 51% for the n=3 case of the total Ga *d* component in the valence band, which is almost the same as what we had observed for the bulk.

Further the presence and absence of the semi-core Ga 3*d* states modifies the lattice constant in the same direction as the bulk calculations. The deviations are found to of the same order as that observed for the bulk. At the theoretical calculated equilibrium lattice constant of these nanocrystals we found band gap of 5.45 and 5.46 eV within our

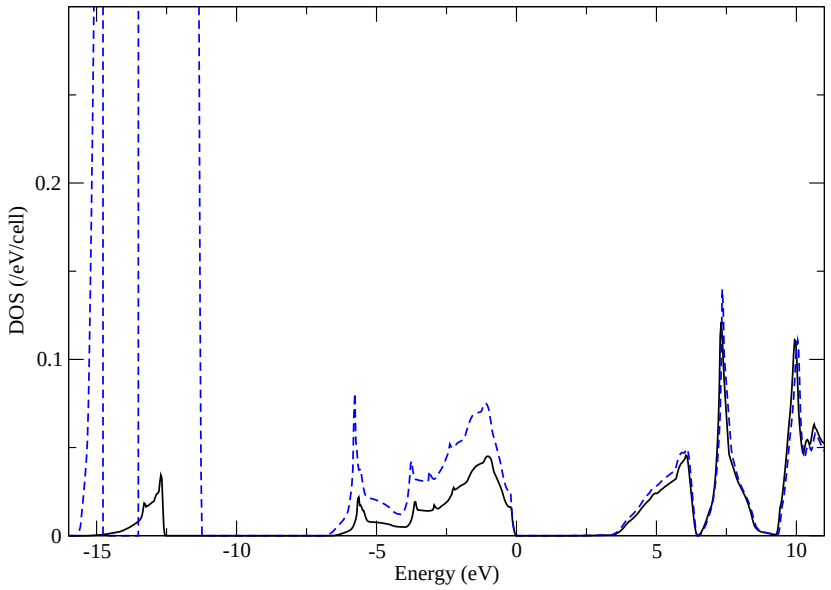

Figure 3.3: The Ga d projected density of states for GaN using PAW potentials with (dotted line) and without (solid line) Ga $3d$ as a part of the valence band. The zero of the energy corresponds to the valence band maximum.

calculations and larger nanocrystal had a band gap of 4.79 and 4.76 eV, for the cases with and without the inclusion of Ga $3d$ states in the basis separately.

3.1.4 Conclusion

Hence we have studied the modification of the equilibrium properties for GaN, with and without treating the Ga $3d$ in the valence, in both the bulk as well as in the nanocrystal limit. The effects of the lattice constant modification are found to be small and of the order of 1% at both limits. Hence we conclude that a treatment using PAW potentials where Ga $3d$ states are treated as a part of the core is adequate to describe the properties of the GaN.

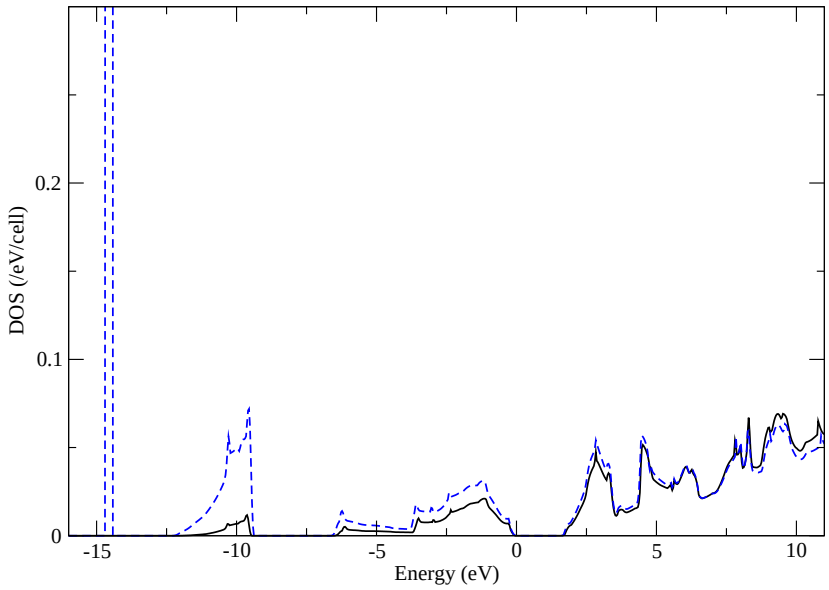

Figure 3.4: The Ga d projected density of states for GaP using PAW potentials with (dotted line) and without (solid line) Ga $3d$ as a part of the valence band. The zero of energy corresponds to the valence band maximum.

3.2 Role of Coulomb interactions in semicore levels Ga d levels of GaX semiconductors: Implication on band offsets

3.2.1 Introduction

Enormous progress has been made over the years in the development of realistic theories of materials starting from a approach [16]. A popular method in this direction is the Kohn-Sham formalism of density functional theory (DFT). The Hohenberg-Kohn theorem [17] states that the ground state energy can be written as an exact functional of the density.

[2]This section is based on the following paper:
R. Cherian, P. Mahadevan, and C. Persson, *Role of Coulomb interactions in semicore levels : Implication on band offsets*, Accepted in Solid State Communications.

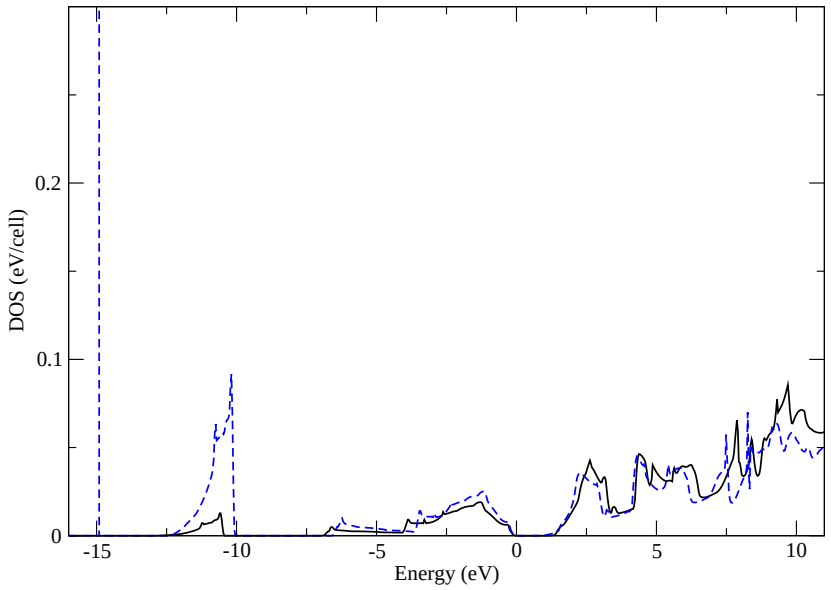

Figure 3.5: The Ga d projected density of states for GaAs using PAW potentials with (dotted line) and without (solid line) Ga $3d$ as a part of the valence band. The zero of energy corresponds to the valence band maximum.

Unfortunately the exact form of the functional is not known, and approximations such as the original local density approximation (LDA) [18, 19] as well as various types of the generalized gradient approximations (GGA) [14, 20] have been used quite successfully in describing the ground state properties of a wide variety of systems. See Ref. [21] for pros and cons of the DFT.

The limitations of the approximated exchange functionals (incorrect self interaction and the neglect of correlations effects) directly affect the electron energy states, especially excited properties such as the band-gap energy. For s-p bonded semiconductors, the GW approximation [22] has been enormously successful in improving the gap energy by partially or fully self-consistently solving the Dyson equation. However, another contributory factor to the LDA band-gap error is the cation d position [23], especially for shallow d

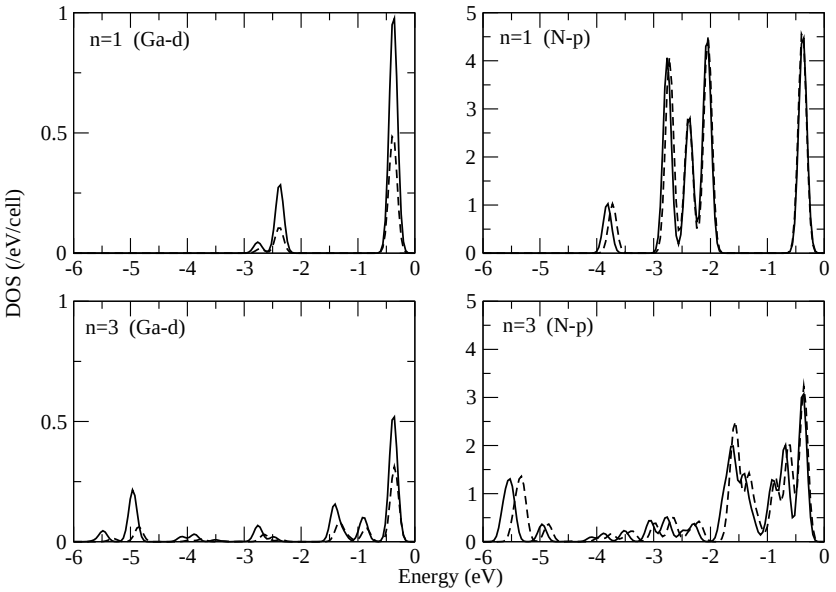

Figure 3.6: The Ga d projected density of states (left panel) using PAW potentials with (solid line) and without (dashed line) Ga $3d$ as a part of the valence band, the N p projected density of states (right panel) using PAW potentials with (solid line) and without (dashed line) Ga $3d$ as a part of the valence band for the two nanocrystal sizes n=1 (top panel) and n=3 (bottom panel) considered have been shown. The zero of energy corresponds to the valence band maximum.

states. The reason is that the LDA d-levels are not deep enough to be chemically inert, and so they interact with the valence band states leading to a reduction of the gap energy. To correct this LDA error, without degrading the computational time, an on-site correction potential U has been proposed [24]. The correction potential is chosen to be dependent on the atom and angular momentum projected density operator [25, 26], therefore the correction will affect mainly the semicore states. Within this LDA+U model, the potential correction thus pushes the semicore/valence states to deeper energies and thereby modifies the valence band maximum position as a result of the modified semicore/valence interaction.

Table 3.3: Optimized lattice constant in Å for Ga centered nanocrystals.

Nanocrystal size (n)	PAW	
	no Ga-d	with Ga-d
1	4.521	4.483
3	4.550	4.509

In this work, we examine the modification of the energy of the valence band maximum and the consequent change in the band gap arising from an incorrect position of the semicore d states on the cations in binary GaX semiconductors (X = N, P, and As). The belief has been that the t_2 states on the semicore cation d states interact with the states comprising the valence band maximum with the same symmetry pushing them up. As a result, the band gap is reduced. A recent paper [27] has questioned this model, and has proposed that a part of the shifts come from modified screening effects which result in a movement of the conduction band minimum also. Re-examining this proposition we demonstrate that the opening of the band gap with a U correction on the semicore d states is due to a movement of the valence band maximum alone. In addition there is a reorganization of charge on the Ga atoms and this results in large shifts of $\sim$ 1-2 eV of the core levels on Ga while those on the anion remain unchanged.

3.2.2 Methodology

We have carried out *ab-initio* calculations within the local spin density approximation of the DFT. A full potential linearized augmented plane wave (FPLAPW) implementation in the WIEN2k code was used by us in our calculations. We considered the systems GaN, GaP and GaAs in the zinc-blende structure. The radii for the muffin tin spheres used were R_{MT} = 1.20, 1.16 and 0.96 Å for both Ga and X in GaAs, GaP and GaN, respectively. In the calculations we use $G_{MAX} = 14$ and $|K| < 9/R_{MT}$. The LDA approximation to the exchange functional was used. The number of k-points used was 8×8×8 for the self-consistency and in the evaluation of the density-of-states (DOS). The tetrahedron method of integration was used for the DOS calculation. An additional potential within the LDA+U [26] formalism was introduced on the Ga d states, and the changes in

the electronic structure were calculated as a function of U. Superlattices of the form $(GaX)_5/(Ga(U)X)_5$ were constructed to determine the valence- and conduction band offsets introduced by U with respect to the $U = 0$ eV result. A k-points grid of 8×8×1 was used for the superlattice.

The equilibrium lattice constants of these materials were found to be 4.46, 5.40 and 5.61 Å (Table 3.4), respectively, in the absence of any U on the Ga d states. The value of U applicable for each system was determined by comparing the energy of the semicore d states with that determined from photoemission experiments [28, 29], yielding $U = 11$, 10 and 9 eV for GaN, GaP and GaAs respectively. Using these values, the equilibrium lattice constants were determined to be slightly smaller, namely 4.45, 5.37 and 5.58 Å, respectively. The results are given in Table 3.4. In order to make a proper comparison with earlier published work [27] which was performed with a plane wave pseudopotential implementation, we calculate the equilibrium lattice constant also by using projector augmented-wave (PAW) potentials [13] within the VASP package.

Table 3.4: Calculated lattice constants in units of Å of GaN, GaP and GaAs using the VASP/PAW and WIEN2k/FPLAPW methods. $U = 11$, 10 and 9 eV for GaN, GaP and GaAs, respectively.

	LDA		LDA+U	
	VASP	WIEN2k	VASP	WIEN2k
GaN	4.46	4.46	4.24	4.45
GaP	5.39	5.40	5.27	5.37
GaAs	5.61	5.61	5.49	5.58

In order to obtain the band lineup between the LDA and LDA+U calculations, the following prescription was followed. First, we performed bulk calculations using WIEN2k for GaX within LDA and LDA+U separately at its equilibrium lattice constant, and we determined the valence band maximum and the conduction band minimum with respect to the corresponding X anion 1s core level (E_{v_0} and E_{c_0} respectively). As the value of energy by itself has no meaning, we cannot compare the energy corresponding to the valence band maximum/conduction band minimum between two different calculations. Therefore, we

constructed superlattices of the form $(\mathrm{Ga}X)_5/(\mathrm{Ga}(U)X)_5$ and the relative separations of the two core X $1s$ levels in the bulk-like regions on both sides, far away from the interface, were determined. This was used to construct the band lineup. The optimized lattice constants of GaX were different from Ga$(U)X$, and therefore the superlattice was constructed using the average of the lattice constants obtained by the LDA and LDA+U methods. Thereafter, we incorporated the effects of strain on the band lineup, by using the literature values of the hydrostatic deformation potentials for the valence band and conduction band [30]. The strained valence band maximum (E_v) and conduction band minimum (E_c) were related to the unstrained values E_{v_0} and E_{v_0} by the two expressions:

$$E_v = E_{v_0} + a_v \frac{(V-V_0)}{V_0},$$
$$E_c = E_{c_0} + a_c \frac{(V-V_0)}{V_0}$$

where, V_0 was the volume of the unit cell in its equilibrium lattice constant within LDA or LDA+U while V was the volume of the unit cell at the averaged lattice constant. a_v and a_c were the hydrostatic deformation potentials for the valence band maximum and conduction band minimum. The procedure followed in Ref. [27] was similar except that they used the averaged electrostatic potentials instead of core levels for the definition of an absolute energy scale.

3.2.3 Results and Discussion

In Fig. 3.7 we have plotted the Ga d and As p partial density of states for GaAs for the cases without a U on the Ga d states [panel(a)] and with a U on the Ga d states [panel(b)]. The most notable change seems to be a movement of the Ga d states from -15 eV to -18.5 eV with a U of 9 eV. There are changes in the conduction band as well as in the valence band which are not evident on the energy scale at which Fig. 3.7 is plotted. In order to examine the changes in the valence band/conduction band, we first align with respect to the As $1s$ core level in both the systems. The zero of energy has been chosen to be the valence band maximum of the zero U calculations. The conduction bands of the two calculations line up and the shifts are in the valence band alone. As is evident one

has an increase of the band gap. Using the value of U determined to be appropriate for each material, we find that the increase in the band gap is found to be 0.23 eV for GaN, by 0.28 eV for GaP and 0.20 eV for GaAs.

The mechanism for the opening up of the gap has been discussed in the literature in another context [31]. Wei and Zunger [31] examined the role of semicore d states in the valence band offsets of lattice matched common anion semiconductors. The belief was that, for the first approximation, the valence band maximum in the common anion semiconductors should be aligned. Additional interactions were responsible for the observed offsets. For instance, here, these were found to arise from an interaction between the d states with t_2 symmetry on the cation with the corresponding states with the same symmetry comprising the valence band maximum. This interaction pushes the valence band maximum into the band gap, reducing it from the value in the system which has no semicore states. An incorrect position of the semicore states closer to the valence band maximum results in an enhancement of the effective $p - d$ interaction coupling the two interacting states, and therefore a reduction in the band gap.

Recent work by Janotti *et al.* [27] have examined the mechanism of the increase in the band gap with U on the semicore states. Their approach involved determination of the band offsets between the GaX and the Ga(U)X calculations using the procedure described in the methodology. They found shifts in both the valence band maximum as well as the conduction band minimum. The former could be understood by the model described earlier. The shift in the conduction band minimum was understood in terms of modified screening arising from a U on the semicore states.

Our analysis presented in Fig. 3.7 assumes that the X 1s core level are aligned in the two systems. This is not the case and a superlattice geometry is used to determine the relative shifts of the X 1s core level. In addition, Ref. [27] suggested a different equilibrium lattice constant for GaX and Ga(U)X, while analysis of Fig. 3.7 was carried out with the same lattice constant with and without U. We examined the theoretical equilibrium lattice constant within both VASP and WIEN2k with and without potential correction U. We expect small changes due to modified interactions of the semicore states and this is what we find for the results computed within WIEN2k. The results from VASP

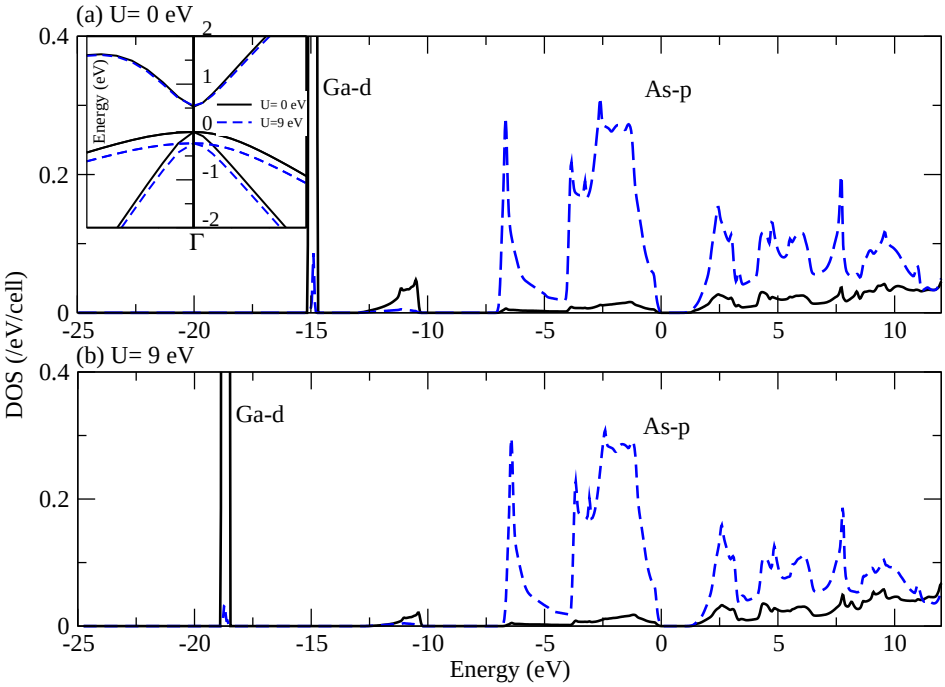

Figure 3.7: The Ga d (black solid lines) and As p (red dashed lines) projected DOS for (a) $U = 0$ eV and (b) $U = 9$ eV on the Ga $3d$ states for GaAs, obtained from the WIEN2k/FPLAPW calculation. The zero of energy corresponds to the valence band maximum. The inset of (a) show the near Γ point magnified view of the band dispersions, (along L-Γ-X direction) for $U = 0$ eV (solid lines) and 9 eV (dashed lines) on the Ga $3d$ states for GaAs. Here, the valence band maximum of the $U = 0$ eV case corresponds to the zero of energy.

suggest much larger deviations in the lattice constant. We are not sure what the origin of this large discrepancy is but we believe this could be the origin of different conclusions arrived at in the earlier work [27].

The band lineup between the zero U and the finite U calculations is given in Fig. 3.8 for GaN, GaP and GaAs. The band-gap energy is found to be 0.22, 0.24 and 0.19 eV larger for the finite U results. In order to examine the origin we look at valence- and conduction band offsets. For GaN we find a shift of 0.704 eV of the conduction band minimum for finite U. This is equal within 10-20 meV to the shift in the N 1s corelevel in the two cases. Hence the conduction band shift cannot contribute to the opening of the band gap. Similar conclusions are reached for GaP and GaAs also. A suprising conclusion from this work are the valence band shifts of the finite U results with respect to the zero U case. We argued that reduced semicore valence interaction should be responsible for the valence band maximum of finite U results to be lower than that of the zero U result. While the Ga 3d levels do move deeper in energy with U, the valence band offset of GaN with U is positive while that of GaAs and GaP are negative with respect to the zero U results. This is a result of the large shifts of the energy eigenvalues for finite U with respect to the zero U result. This is opposite in direction to the shifts of the valence band maximum, due to reduced p-d interaction as the Ga 3d levels move deeper. Hence, we have the observed trend in the valence band offsets.

In order to examine the effect of U on the core levels, we considered the cation and anion core levels for both the finite U as well as zero U case. The results are presented in Table 3.5. In every case we find that the anion levels align with respect to each other. There are however deviations in the cation levels for the finite U calculations. These deviations we find are as large as 1–2 eV.

One could get some hints of the origin of these shifts from the s, p and d components of the charge on each atom calculated as a function of U (Table 3.6).

The most significant changes that we find for any system with U are on the Ga levels, while those on the anion remain largely unchanged. As expected the d component of the charge on the Ga increases as the Ga d becomes more localized. To compensate the s and p components of the charge on Ga decrease. This regulation of charge takes place to

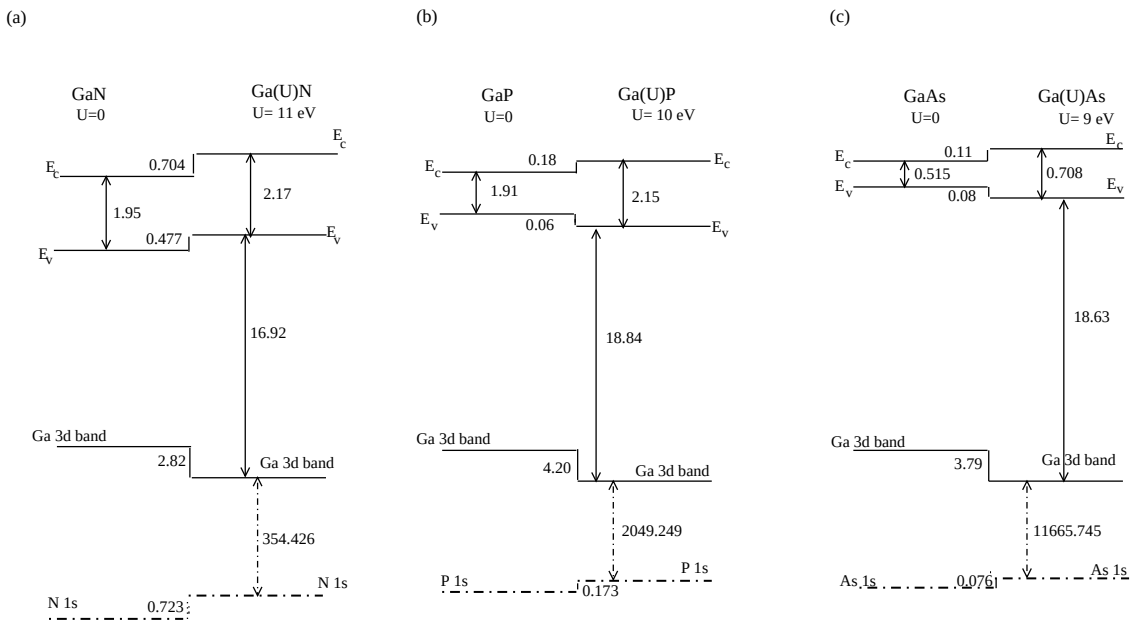

Figure 3.8: Calculated band offsets at the hypothetical interfaces (a) GaN/Ga(U)N, (b) GaP/Ga(U)P and (c) GaAs/Ga(U)As using the WIEN2k/FPLAPW method. U correction has been introduced on the Ga d states. The X (X = N, P, and As) 1s level is shown in dashed dotted lines. The energy separations between the levels are given in eV.

offset the additional Coulomb repulsion that the electrons encounter due to localization of charge on Ga with increasing U. As the interaction between the core and the valence is dependent on the charge on that atom, the Ga related core levels shift while the anion related shifts remain unchanged.

3.2.4 Conclusion

In conclusion, we present a model to understand the opening of the band-gap when a U is applied on the semicore d states present in the III–V semiconductors. An analysis reveals that it is only the modified p-d interaction between the states comprising the valence band maximum and the semicore d states that results in an opening of the band gap with U. The band offsets between the zero-U and the finite-U systems have been evaluated for GaX semiconductors. While one would expect a negative valence band offset of the finite U result with respect to the zero U result as a result of reduced p-d interaction, we find the opposite trend in GaN.

3.3 Role of semicore Ga d states in determining the valence band offset of common anion semiconductors.

3.3.1 Introduction

Band offsets in semiconductor heterostructure

Advances in growth techniques have made it possible to fabricate single crystal layers of one material on some other material by epitaxy. These materials known as heterojunctions [32] have the advantage of giving rise to high quality materials, in addition to suggesting the possibility of changing the properties of the materials over wide limits as a function of the layer thickness which can be varied from a fraction of an atomic layer to hundreds of micrometers.

The properties of such heterostructures constructed from semiconductors are of critical importance for many devices including field-effect transistors, bipolar transistors, light-

emitting diodes and lasers. At the interface of the heterostructure, the energies of the conduction and valence band edges change. The magnitudes of the changes in the band-edge energies are critically important for many semiconductor devices. A key parameter that determines the functionality of the semiconductor heterojuction device is the band offsets between the materials involved.

There have been numerous attempts and models to predict and calculate the energy *bandoffsets* in the semiconductor heterostructures. Here, we restrict ourselves to a few empirical rules and fundamental theoretical concepts which will be useful for the understanding of heterojunction band discontinuities.

Empirical rules

(a) Electron affinity model

The earlier attempts to describe band offsets theoretically assumed that band offset values were determined by the intrinsic properties of each individual semiconductor. Therefore the earlier studies attempted to place the electronic levels in every material on a single absolute energy scale. Band offsets were then determined by the relative position of each material on its absolute energy scale. The first such model was so called electron affinity rule [33] postulated by Anderson, which states that the conduction band offset is given by the simple difference in the electron affinities of the two heterojunction constituents. Electron affinities are determined experimentally to obtain the conduction band offset.

Since the electron affinity is an experimental measure of the energy of the conduction band edge relative to the vacuum level, the essential assumption of the electron affinity rule is that the vacuum level serves as a valid common energy reference level for all material. A major conceptual weakness of this rule is that the electron affinities reflect potential shifts arising from surface electronic structure, rather than shifts that are due to charge redistribution at an actual interface. A more practical consideration is that large uncertainties in experimental electron affinity values results in large ambiguities in predicted band offset values.

(b) Common anion rule

In addition to the electron affinity rule, a number of other semiempirical rules have been proposed for the prediction of the band offset values. The more widely quoted of these have been the so-called common anion rules, proposed originally by McCaldin, McGill and Mead [34] with a modified form later postulated by Menendez *et. al* [35]. The physical motivation for the original common anion rule arises from the theoretical evidence that the valence band states in compound semiconductors are predominantly from p-like atomic orbitals of the anion [36]. Thus leading to the expectation that the position of the semiconductor valence band edge on an absolute energy scale is determined principally by the energies of the valence electrons of the anion. McCaldin *et al.* pointed out that the Schottky barrier height for a large number of II-V and II-VI semiconductors depended primarily on the electronegativity of the anion. It was later proposed [37] that this correction might extend to valence band offset values as well, leading to the postulate that, for a large number of compound semiconductors (materials containing Al being a notable exception), the valence band offset in a heterostructure should depend only on the difference ion the anion electronegativity for the two constituent materials. The physical motivation of the original common anion rule arises from the theoretical evidence that, in a compound semiconductors, the valence band states are derived mainly from the p-like atomic orbitals of the anion. According to this ("common anion rule") rule, the unstrained valence band offsets between the valence band states of the two semiconductor materials AX and BX which share an anion X should be zero. Early theories of band offset, such as those of Harrison [38] and of Frensley and Kroemer [37, 39], were in general agreement with the common anion rule, even for the compounds such as AlAs for which the common anion rule was not claimed to be valid.

Experimentally [34, 40], however, this is not found to be the case and large discrepancies are found between this empirical rule and the observed valence band offset. Wei and Zunger [31] suggested that the deviations from the common anion rule arise largely from the cation-d orbital contributions to the valence band structure, which were generally omitted in early theoretical studies of the band offset. One can understand the band offset observed in AlX/GaX semiconductors (X = N, P, and As) if one considers the

semicore interaction. Ga has chemically active $3d$ states in its valence band, while Al does not. The interaction of the semicore Ga $3d$ states with the anion derived p states in the GaX modifies the valence band position and hence is believed to explain the offset.

Theoretical calculation of band offset: Models and methods

A number of theories have been proposed relating band offset values to the calculated electronic properties of bulk semiconductors. In theoretical calculations the bulk band structure is typically obtained relative to a reference level. A suitable alignment of the reference levels in each semiconductors then yields values for the band offset.

Pseudopotential theory of Frensley and Kroemer [37, 39], is the first attempt to calculate the band offset values without the use of the experimental data for the vacuum-semiconductor or metal-semiconductor interface. In this theory a pseudopotential calculation was used to obtain the bulk band structure for each semiconductor, with a self-consistency condition enforced for the electrostatic potential and the charge density calculated from the valence band functions. Once the individual bulk band structure is obtained for the semiconductors, the band offsets in a heterostructure could be obtained by matching the energies of the interstitial potentials for the two heterostructure constituents.

This theory was refined [39] to include an approximate correction to account for heterojunction dipoles induced charge redistribution near the interface. By estimating the effective charge on the atoms near the interface using the electronegativities of each atom and its nearest neighbors an approximate calculation of the heterojuction dipole effects was made. This scheme leads to an effective "electronegativity potential" for each semiconductor. The correction to the band offsets for the heterojunction dipole effects was then taken to be simply the difference in the electronegativity potential for the two heterojunction constituents.

Frensley and Kroemer [39] shows that the dipole correction for most lattice-matched heterojunction pairs is typically few tenths of an electron volt or even less than that. For lattice-mismatched hererojunction the apparent dipole corrections can be larger and the

applicability of Frensley and Kroemer's electronegativity potential in lattice-mismatched heterojunctions is probably questionable.

Another early theory of heterojunction band offset was the linear combination of atomic orbitals (LCAO) theory of Harrison [38]. The basis of the Harrison model is the linear combination of atomic orbitals of a very small group of atoms which then used to calculate the band structure. The band structure calculation would be correct if the true atomic-like potentials and energy eigenfunctions of the atoms forming the semiconductor would be known. Because the atomic-like potentials and eigen energies of the atoms in the crystal lattice are unknown, Harrison simply took takes as unperturbed atomic energies values the theoretical values of the free atoms. Hence this model is clearly an approximation. In this model, several more approximations are employed for the calculation of the matrix elements coupling the relevant atomic states between the nearest neighbors. The valence band edge energies obtained using the LCAO approach are therefore automatically given on the same energy determined by the individual atomic state energies, and the valence band offset are determined just by taking the difference between the valence band edge energies on this common energy scale for the two heterojunction materials. Conduction band offsets can be determined from the valence band offset and the experimental band gaps for each material. As was the case with the semiempirical rules and the original theory of Frensley and Kroemer, Harrison's LCAO theory does not include any correction for heterojunction dipole effects.

A number of theories have been developed that include effects arising from the detailed electronic structure of the specific semiconductor interface under consideration. Van de Walle and Martin [41, 30] have calculated band offset values by using self consistent local density functional theory and *ab-initio* pseudopotentials to compute the electronic structure in each layer of a superlattice. The calculations of Van de Walle and Martin were also the first to incorporate the effects of strain in lattice-mismatched heterojunctions, where the Si/Ge heterojunctions were considered as a prototypical lattice-mismatched material system. On the basis of their self-consistent local density functional calculations for the Si/Ge and other heterojunction systems, they proposed a model solid theory of band offsets [41, 30].

In their model solid theory, an absolute electrostatic potential is computed for each material by constructing the solid as a superposition of neutral atoms. The atomic potentials can be placed on an absolute energy scale common to all the materials, and hence an average electrostatic potential relative to the atomic potential can be defined in the solid. This procedure resulted in good agreement with the results of the full self-consistent interface calculations. The bulk band structure relative to the average electrostatic potential within the solid is calculated using the *ab-initio* pseudopotentials and it is now possible to define the position of the valence band edge in each material on the common energy scale given by the atomic potentials and consequently to derive the band offset values for various heterojunctions. Van de Walle [30] has also calculated the absolute deformation potentials using the model solid approach, which allows to predict the band offsets in strained heterojunctions.

Since the energy reference of the band structure can be related to the average electrostatic potential, it is sufficient to estimate the change in the average electrostatic potential through the interface from a heterostructure calculation, and then align the bulk valence band maxima accordingly to obtain the valence band offset. Bylander and Kleinman [42, 43] used a method where the interfacial double-layer potential (ΔV), induced by the planar average of the difference between the superlattice and the bulk constituent charge densities was used along with the bulk constituent eigenvalues of the valence band maximum, in order to determine the valence band offset. In the method of Baldereschi *et al.* [44] running average across the unit cell, along the growth direction, of the xy planar averaged potential is calculated to obtain a slowly varying curve for the potential, from where it is a simple thing to read the potential shifts. In principle, one could also take only one point (any point) from the electrostatic potential and compare that between the interface calculation and the bulk calculation. In practice, due to charge redistribution and geometric relaxations, a well-defined reference point in space should be chosen. An example of such a point would be the potential in the core regions of the ions. Merely from this reasoning, it is possible to write out the equation for the band offset between the materials AX and BY

$$\begin{aligned}\Delta E_v &= (E_v[AX] - V_c[AX])^b - (E_v[BY] - V_c[BY])^b + (V_c[AX] - V_c[BY])^i \\ &= (E_v[AX] - E_v[BY])^b + (V_c[AX]^i - V_c[AX]^b - V_c[BY]^i + V_c[BY]^b)\end{aligned}$$

ie,

$$\Delta E_v = \Delta E_v^b + \Delta V_c^i, \tag{3.1}$$

where $E_v[AX(BY)]$ is the valence band maximum and V_c[AX(BY)] is the electrostatic potential at the core of a given type of an atom (anion or cation) located in the material AX(BY). Superscripts b and i stand for the bulk and interface calculation, respectively. Finally, Δ E_v^b, is the lineup of the VBM between the bulk constituents AX and BY , and Δ V_c^i, aligns the energy reference by combining the electrostatic potentials at the core of some appropriately chosen anions or cations from the bulk and interface calculations.

Further justification for the use of the electrostatic potential at the atomic core, in aligning the two bulk band structures can be found from the idea of the band offset determination by the core-level photoemission spectroscopy [45]. In this approach, the core levels are measured with respect to the valence band maxima. At the same time, the change in the core-level energy from one side of the interface (AX) to the other (BY) is also measured, so that the valence band offset ΔE_v at the heterojunction interface is simply given by,

$$\Delta E_v = (E_v[AX] - E_{cl}[AX]) - (E_v[BY] - E_{cl}[BY]) + (E_{cl}[AX]^i - E_{cl}[BY]^i), \tag{3.2}$$

where E_v[AX(BY)] and E_{cl}[AX(BY)] are the valence band maximum and core-level energy of the material AX(BY), far away from the interface, and $E_{cl}[\mathrm{AX(BY)}]^i$ is the corelevel energy at the AX(BY) side of the interface.

Using the core-level energies in determining the band offset is computationally problematic, since this approach requires, if not an all-electron method, at least a method with deep core potentials and subsequently sufficient number of valence electrons active in the

calculation. A comprehensive list of band offsets for binary materials calculated with this approach, using the linearized augmented plane wave (LAPW) method, has been given by Wei and Zunger [46].

The procedure followed by Wei and Zunger [46] is the following. To obtain the unstrained "natural" offsets, the core-to-valence band maximum (VBM) one electron energy difference is calculated for AX (and similarly for BY) at their respective equilibrium experimental zinc-blende lattice constants. The core level difference is obtained here from the calculation for the $(AX)_n/(BY)_n$ superlattices with (001) orientation. In their studies they find that for most of the systems n=3 is sufficient to converge $(E_{cl}[AX]^i - E_{cl}[BY]^i)$ within 0.02 eV with the error been larger for systems with large lattice mismatch (e.g., GaN/GaAs). The method of Wei and Zunger [46] is what is followed in the literature to determine band offsets.

Our interest in this problem was motivated by the important role played by the semicore d states in determining the band offsets between lattice matched semiconductors. The work by Wei and Zunger [31] pointed this out for the first time. This can be understood as follows. Considering the example of GaAs, one finds that the valence band maximum (VBM) which is derived from Γ point has t_2 symmetry. The semi core Ga $3d$ states split in the point ion limit into doubly degenerate e states and triply degenerate t_2 states. These states are depicted schematically Fig. 3.9. The levels with the same symmetry interact and the energy level diagram taking into account the interactions is shown in the central panel. Starting with $t_2(p)$ levels at the same position in GaX/AlX semiconductors, this interaction pushes the antibonding levels to higher energies in GaX semiconductors. Our earlier analysis in the chapter showed that even in GaN where the semicore states are just 11 eV deeper than the valence band maximum, the semicore states do not play any significant role in determining the equilibrium properties. Hence the suggestion of shifts of 0.80 eV [46] arising from an interactions semicore d states with the valence states seems unlikely.

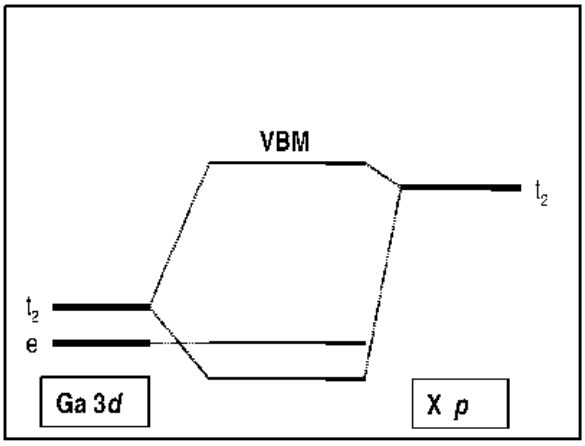

Figure 3.9: Schematic energy level diagram for the interaction of the Ga 3d states and X p states.

3.3.2 Methodology

In this work we have carried out full potential linearised augmented plane-wave (FPLAPW) calculations as implemented in the WIEN2k code to determine the unstrained valence band offset between the common anion pairs of semiconductors GaN/AlN, GaP/AlP and GaAs/AlAs. These are determined by aligning the X 1s core levels in two separate FPLAPW calculations carried out for the bulk. However, this computation of the band offset also includes the chemical shift of the core levels which must be subtracted out to determine the shift of the valence band maxima alone. The chemical shifts have been computed for the same core-levels considering a superlattice geometry of $(AlX/GaX)_3$ in the (001) direction as used earlier [46]. This method has some uncertainties associated with it which we determine to be 0.020 eV. This is a result of the uncertainty in the chemical shift associated with the core levels of same atom type.

The zinc-blende structure was considered for all the compounds. The lattice constants of GaN, GaP, and GaAs were kept fixed at the experimental values of 4.52, 5.45 and 5.65

Å respectively [32, 47], while those of AlX were kept fixed to the values of their GaX counterparts. This was the case also for the superlattice geometry. For both Ga and X (Al and X) the radii for the muffin tin spheres used were R_{MT} = 1.20, 1.16 and 0.96 Å in GaAs (AlAs), GaP (AlP) and GaN (AlN) respectively. In the calculations we use G_{MAX} = 14 and $|K| < 9/R_{MT}$. A Γ centered grid of 8x8x8 was used in addition to the GGA PW91 approximation [14] for the exchange functional. In the case of superlattice studies k-points grid of 8x8x1 were considered.

There have also been earlier attempts [48] to estimate the role of p-d interactions in the offset values. All these approaches have started with tight-binding Hamiltonians whose parameters were determined from atomic calculations [49]. Hence agreement with earlier theories was not really a ratification of the theory. Therefore, in this work, we study the role of the semi core Ga 3d levels in modifying the core valence interaction, by fitting the *ab-initio* band structure to a minimal *spd* tight-binding model. A tight-binding Hamiltonian that included hopping between nearest neighbor anion-cation pairs as well as second neighbor anion/cation pairs was considered. The parameters entering the tight-binding Hamiltonian were determined by fitting to the *ab-initio* eigenvalue energies at symmetry points by a least-square error minimization procedure. This is the first time that a fully microscopic Hamiltonian that describes the valence and conduction band structure of the GaX semiconductors has been used. Setting the semi-core valence interaction to zero we determine the modification of the valence band offset coming from semi core valence interaction.

Our studies suggest that *the semi-core valence interaction cannot be the only explanation for the large valence band offsets* that one observes in these common anion systems. We propose a new model for the observed valence band offset for these common anion semiconductors by taking the cation-p anion-p interactions into account.

3.3.3 Results and Discussion

The valence band offset between the common anion pairs of semiconductors GaX/AlX (X=N, P and As) have been calculated and found to be 0.72, 0.48 and 0.50 eV respectively by the method outlined above. This is in agreement with other estimates [46] as well as

other experimental estimates [50]. These contains two parts - the first due to purely electronic contributions, and the second due to charge transfer taking place at the interface. As we are interested in just the electronic contribution to the band offset, we substract out the contribution arising from the interface charge transfer to get 1.29, 1.04 and 0.81 eV respectively. Our interest is to set up a microscopic model to determine the electronic interactions that determine the band offset. The first step in this direction is to set up a minimal tight binding model. Examining the density of states given in Fig. 3.10 for GaX and AlX semiconductors, the Ga s, p and d states contribute in the energy window -20 to 5-10 eV above Fermi energy (which is chosen to be the valence band maximum). Al s and p states mainly contribute in the same energy range. On the anions we find s, p and d states contribute in this energy window, except in the case of GaN where the contribution of N d states is very small. In the case of GaX semiconductors the tight binding model included s, p and d states on Ga and s, p, d^* states on P and As (here d^* corresponds to the unoccupied d states), while in the case of N only s, p states were taken in the basis. For the AlX tight-binding studies s, p states on Al and s, p, d^* states on N, P and As were considered. This choice of ours is similar to the earlier tight binding works [51] where the only difference was that they did not include Ga d states in the basis. Before we proceed with the fitting of the *ab-initio* band structure, the energy eigen values for different materials have to have a common energy reference. This is done by aligning the X 1s corelevel in the two materials comprising the heterostructure. Once the X 1s core levels in the two separate GaX and AlX calculations are aligned we see that automatically the other X core levels gets aligned within an error of 0.06 and 0.03 eV in the case of GaP and GaAs. In the case of GaN we have just the core N 1s level. After aligning with the X 1s core level and looking at the eigen values at the Γ point we see that the semicore X 2s, 3s and 4s level also gets aligned, within an error of 0.17, 0.08 and 0.04 eV in the two separate sets (GaX and AlX) of calculations for X=N, P and As respectively.

This motivates us to impose a constraint on the tight binding parameters, which is that the anion s onsite energy be the same in both the materials. A comparison of the band structure - *ab-initio* as well as the tight binding fit are given in Figs. 3.11 and 3.12. The tight binding model is found to reproduce the *ab-initio* band structure in the desired energy window. The fitted parameters are given in Tables 3.7 and 3.8.

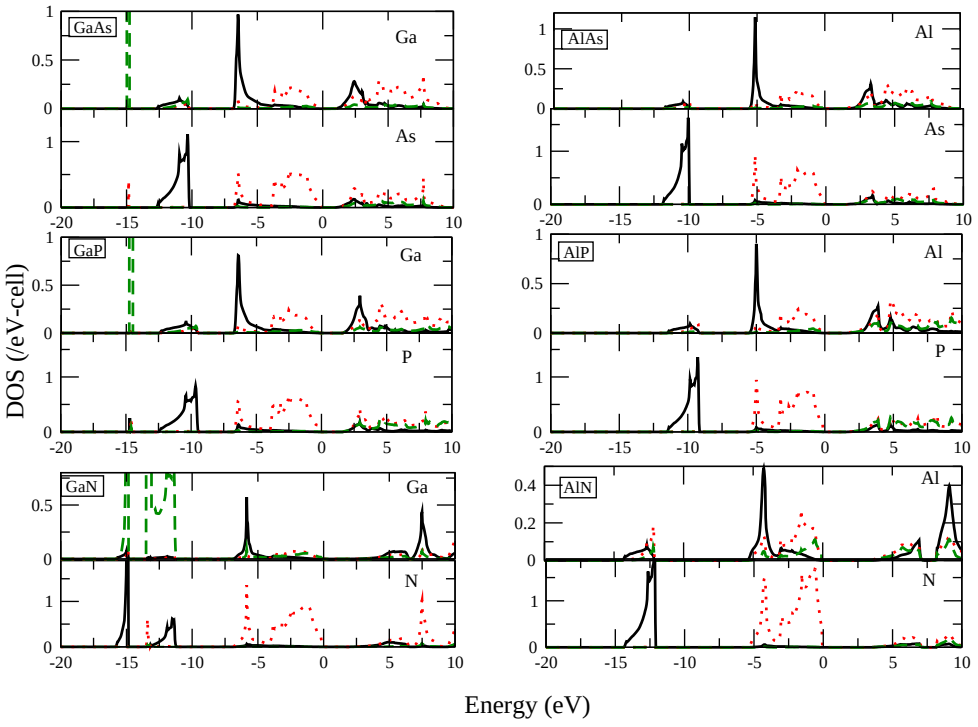

Figure 3.10: Cation and anion s (solid line), p (dotted line) and d (dashed line) projected density of states for GaX and AlX semiconductors. The zero of energy corresponds to the valence band maximum.

Our fitted parameters matches quite well with earlier tight binding fitting method [51]. An interesting aspect that emerges from this analysis is that the X p and X d almost get aligned up. An initial look at the tight binding parameters does not make our task look easy as there are 40 parameters for GaX semiconductors and 27 parameters in AlX semiconductors. However if we look at the tight binding Hamiltonian at the Gamma point [49] we find that it block diagonalizes (Table 3.9) and one just has to consider the anion p block interacting with the cation d and cation p blocks to explain the shifts in the band offsets.

The contribution to the valence band offset from the interactions was determined by switching off the interaction and observing the shift of the valence band maximum. The shift was found to be 0.09 eV for GaAs, 0.1 eV for GaP and 0.16 eV for GaN. Hence p-d interactions alone cannot explain the large band offsets that exist between GaX and AlX semiconductors.

We next calculated the shifts in the VBM of GaX and AlX coming from the anion p states and cation p states. The presence of cation-p and anion-p in GaX and in AlX moves the VBM to lower energy. But the movement to the VBM in AlX towards lower energy is more compared to GaX, this is because the separation between the cation-p and anion-p levels are lower in the case of the AlX compared to GaX and moreover the estimated cation-p and anion-p (p-p) interaction is larger in the case of AlX compared to GaX (Tables 3.7 and 3.8). The overall effect of this interaction is the movement of AlX VBM to lower energy with respect to the VBM of the GaX counterpart. From our tight binding analysis we found of that the valence band offset that comes from this interactions is 0.59 eV for GaAs/AlAs, 0.91 eV for the GaP/AlP and 0.77 eV for GaN/AlN semiconductors. Thus the total valence band offset that comes from these two interactions are 0.68 eV for GaAs/AlAs, 1.01 eV for GaP/AlP and 0.93 eV for GaN/AlN. While the electronic contribution to the band offset was earlier found to be 0.81, 1.04 and 1.29 eV in the case of GaAs/AlAs, GaP/AlP and GaN/AlN respectively, thus out of this total 84%, 97% and 72% contribution comes from the p-d and p-p interactions in GaAs/AlAs, GaP/AlP and GaN/AlN semiconductors respectively.

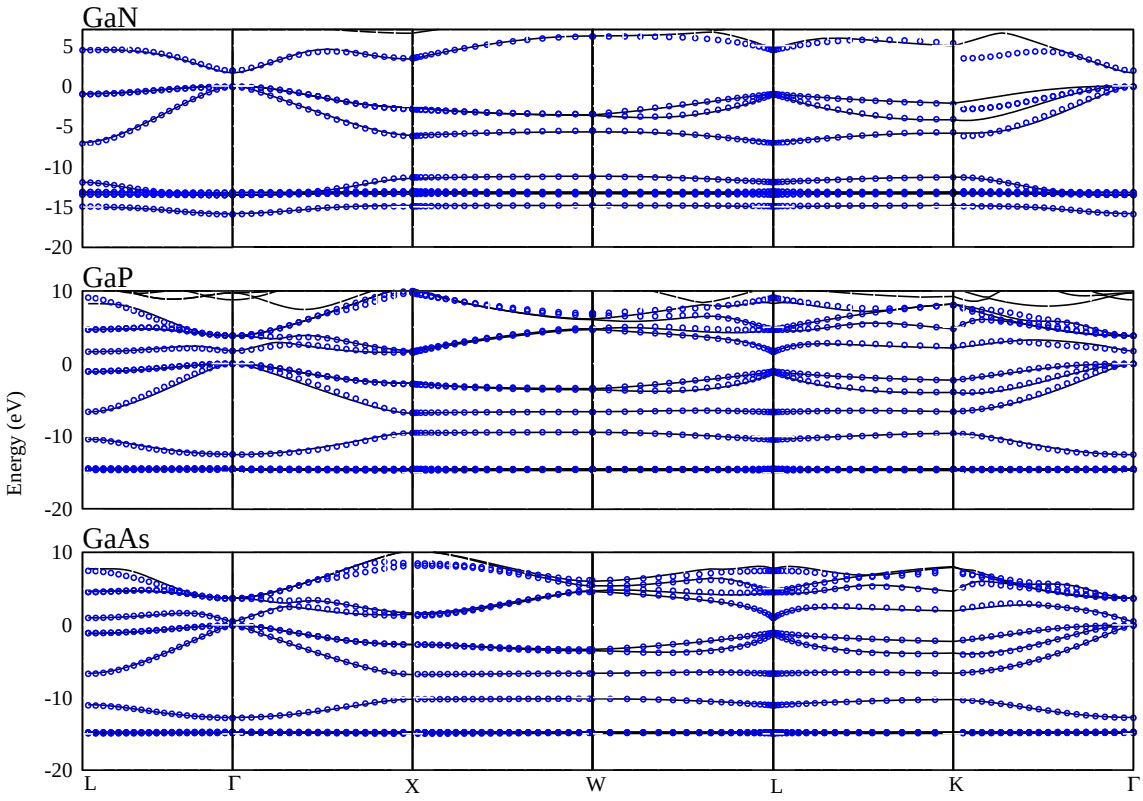

Figure 3.11: Comparisons of the band dispersions obtained for GaN, GaP and GaAs, from FPLAPW (solid lines) calculations and from TB fitting (open circles). Here the VBM of GaX is set to zero of the energy.

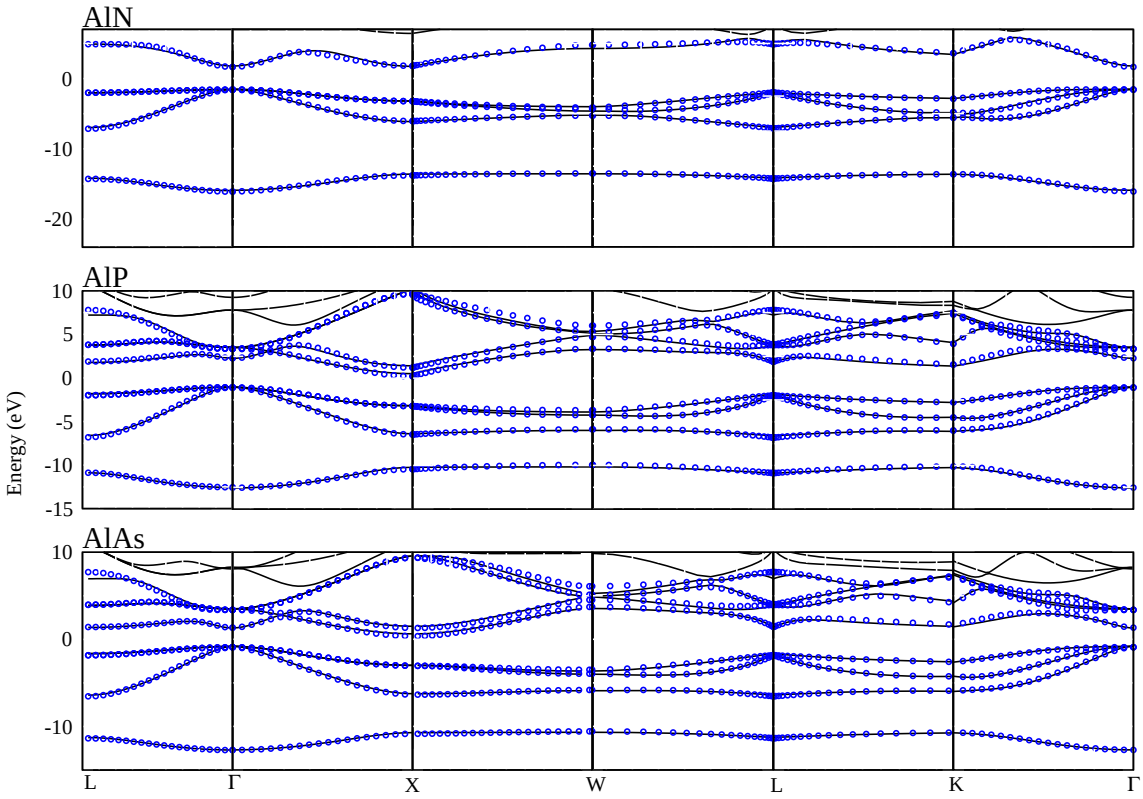

Figure 3.12: Comparisons of the band dispersions obtained for AlN, AlP and AlAs, from FPLAPW (solid lines) calculations and from TB fitting (open circles). Here X'1s core level of AlX is aligned to the X'1s core of GaX and all energies been shifted so that the VBM of GaX is set to zero of the energy.

3.3.4 Conclusion

To summarize, the valence band offsets between common anion semiconductors have been calculated. The role of p-d interactions in determining the valence band offsets have been clarified for the first time. Quantitative estimates were obtained starting from a microscopic Hamiltonian found to give a good description of the band structure of GaX and AlX semiconductors. The results suggest that p-d interactions account only a small percentage of the observed band offset while the main interaction that contribution comes from the cation-p and anion-p interactions.

Table 3.5: The relative shifts on the Ga and X (anion) core levels in units of eV with respect to the X 1s core level.

		Core level	U (eV)		
			0	10	15
GaN					
	Ga	$1s_{1/2}$	-9825.863	-9824.478	-9823.856
	Ga	$2s_{1/2}$	-881.193	-879.698	-879.027
	Ga	$2p_{1/2}$	-738.006	-736.518	-735.849
	Ga	$2p_{3/2}$	-710.420	-708.932	-708.262
	Ga	$3s_{1/2}$	230.453	231.524	232.003
	N	$1s_{1/2}$	0.0	0.0	0.0
GaP					
	Ga	$1s_{1/2}$	-8130.089	-8129.483	-8129.223
	Ga	$2s_{1/2}$	814.301	814.972	815.259
	Ga	$2p_{1/2}$	957.513	958.178	958.464
	Ga	$2p_{3/2}$	985.096	985.761	986.047
	Ga	$3s_{1/2}$	1926.017	1926.523	1926.739
	Ga	$3p_{1/2}$	1972.305	1972.799	1973.010
	Ga	$3p_{3/2}$	1975.943	1976.431	1976.640
	P	$1s_{1/2}$	0.0	0.0	0.0
	P	$2s_{1/2}$	1901.728	1901.722	1901.720
	P	$2p_{1/2}$	1949.755	1949.749	1949.748
	P	$2p_{3/2}$	1950.668	1950.663	1950.662
GaAs					
	Ga	$1s_{1/2}$	1485.670	1486.197	1486.420
	Ga	$2s_{1/2}$	10430.076	10430.660	10430.909
	Ga	$2p_{1/2}$	10573.286	10573.865	10574.111
	Ga	$2p_{3/2}$	10600.868	10601.448	10601.695
	Ga	$3s_{1/2}$	11541.798	11542.241	11542.429
	Ga	$3p_{1/2}$	11588.0860	11588.519	11588.703
	Ga	$3p_{3/2}$	11591.724	11592.153	11592.334
	As	$1s_{1/2}$	0.0	0.0	0.0
	As	$2s_{1/2}$	10207.062	10207.059	10207.059
	As	$2p_{1/2}$	10363.728	10363.726	10363.725
	As	$2p_{3/2}$	10400.200	10400.197	10400.197
	As	$3s_{1/2}$	11500.795	11500.795	11500.796
	As	$3p_{1/2}$	11553.433	11553.433	11553.435
	As	$3p_{3/2}$	11558.466	11558.466	11558.467

Table 3.6: The calculated s, p, d and total components of the charge on Ga and X (X = N, P and As) as functions of U, where a U has been introduced only on the Ga d states.

		U (eV)	s	p	d	total
GaN						
	Ga	0	0.256	0.207	9.393	9.863
	Ga	5	0.252	0.204	9.428	9.889
	Ga	10	0.248	0.201	9.461	9.915
	Ga	15	0.245	0.198	9.491	9.939
	N	0	1.282	2.691	0.016	3.993
	N	5	1.282	2.695	0.015	3.995
	N	10	1.282	2.698	0.014	3.998
	N	15	1.282	2.702	0.013	4.000
GaP						
	Ga	0	0.744	0.710	9.900	11.369
	Ga	5	0.737	0.698	9.924	11.375
	Ga	10	0.732	0.687	9.947	11.381
	Ga	15	0.726	0.675	9.968	11.385
	P	0	1.272	2.079	0.068	3.430
	P	5	1.271	2.087	0.066	3.434
	P	10	1.270	2.094	0.064	3.437
	P	15	1.269	2.100	0.062	3.440
GaAs						
	Ga	0	0.820	0.746	9.932	11.515
	Ga	5	0.814	0.734	9.954	11.518
	Ga	10	0.808	0.722	9.975	11.522
	Ga	15	0.802	0.710	9.996	11.524
	As	0	1.341	1.902	10.025	13.278
	As	5	1.340	1.910	10.023	13.282
	As	10	1.338	1.917	10.021	13.286
	As	15	1.335	1.924	10.020	13.288

Table 3.7: Tight-binding parameters (in eV) obtained from a least-squared-error fitting procedure for GaX semiconductors. The VBM of GaX is set to the zero of the energy.

	GaN	GaP	GaAs
s_c	8.63	1.62	0.97
p_c	8.73	7.82	6.55
d_c	-13.23	-14.49	-14.78
s_a	-12.83	-8.64	-10.01
p_a	-1.01	-0.53	-0.41
d_a	-	7.64	6.84
$s_c s_a\sigma$	-1.66	-1.58	-1.33
$s_c p_a\sigma$	3.60	2.74	2.67
$s_c d_a\sigma$	-	-2.03	-1.72
$p_c p_a\sigma$	3.03	2.83	2.94
$p_c p_a\pi$	-0.82	-1.03	-0.81
$p_c d_a\sigma$	-	-0.54	-0.50
$p_c d_a\pi$	-	1.63	1.28
$d_c d_a\sigma$	-	0.0	0.0
$d_c d_a\pi$	-	0.0	0.0
$d_c d_a\delta$	-	0.0	0.0
$p_c s_a\sigma$	-0.11	-1.55	-0.75
$d_c s_a\sigma$	-0.76	0.0	0.0
$d_c p_a\sigma$	1.11	0.654	0.568
$d_c p_a\pi$	-0.00	-0.216	-0.318
$s_c s_c\sigma$	-0.81	-0.31	-0.26
$s_c p_c\sigma$	0.89	0.45	0.05
$s_c d_c\sigma$	-0.11	-0.21	-0.16
$p_c p_c\sigma$	1.33	0.01	0.28
$p_c p_c\pi$	0.0	-0.02	-0.23
$p_c d_c\sigma$	0.12	0.01	0.0
$p_c d_c\pi$	0.25	0.09	0.0
$d_c d_c\sigma$	-0.01	-0.01	0.0
$d_c d_c\pi$	0.02	0.01	0.01
$d_c d_c\delta$	0.0	0.0	0.0

	GaN	GaP	GaAs
$s_a s_a\sigma$	-0.01	0.0	-0.01
$s_a p_a\sigma$	0.17	0.15	0.07
$s_a d_a\sigma$	-	-0.12	-0.13
$p_a p_a\sigma$	0.35	0.25	0.31
$p_a p_a\pi$	-0.05	-0.15	-0.04
$p_a d_a\sigma$	-	-0.24	-0.31
$p_a d_a\pi$	-	0.15	0.13
$d_a d_a\sigma$	-	-0.94	-0.84
$d_a d_a\pi$	-	0.50	0.43
$d_a d_a\delta$	-	-0.09	-0.036

Table 3.8: Tight-binding parameters (in eV) obtained from a least-squared-error fitting procedure for AlX semiconductors. Here the X 1s core levels in AlX is aligned with that of GaX and then setting the VBM of GaX to zero of the energy.

	AlN	AlP	AlAs
s_c	5.09	4.37	5.23
p_c	6.52	6.37	6.47
s_a	-12.83	-8.64	-10.01
p_a	-1.01	-0.35	-0.45
d_a	10.12	7.01	6.98
$s_c s_a \sigma$	-1.72	-1.50	-1.22
$s_c p_a \sigma$	2.95	3.15	3.14
$s_c d_a \sigma$	0.0	-1.69	-2.07
$p_c p_a \sigma$	3.36	3.55	3.33
$p_c p_a \pi$	-0.52	-0.61	-0.63
$p_c d_a \sigma$	-1.12	-0.50	-0.40
$p_c d_a \pi$	2.07	1.94	1.80
$p_c s_a \sigma$	-1.49	-2.11	-1.55
$s_c s_c \sigma$	-0.56	-0.43	-0.49
$s_c p_c \sigma$	0.10	0.24	0.32
$p_c p_c \sigma$	0.57	0.58	0.46
$p_c p_c \pi$	0.0	-0.29	-0.28
$s_a s_a \sigma$	0.0	0.07	-0.06
$s_a p_a \sigma$	0.11	0.19	0.122
$s_a d_a \sigma$	-0.40	-0.13	-0.18
$p_a p_a \sigma$	0.40	0.29	0.27
$p_a p_a \pi$	-0.13	-0.01	-0.01
$p_a d_a \sigma$	-0.25	0.0	0.0
$p_a d_a \pi$	0.14	0.0	0.07
$d_a d_a \sigma$	-0.0	-1.14	-1.05
$d_a d_a \pi$	0.0	0.44	0.40
$d_a d_a \delta$	0.0	0.0	0.0

Table 3.9: The LCAO Hamiltonian matrix at Γ point for the zinc-blende structure taking the s, p, d of cation and s,p of anion in the basis. At Γ point the matrix can be divided into two block diagonal matrices as shown below.

$$
\begin{array}{c} \\ s^c \\ s^a \\ d^c_{x^2-y^2} \\ d^c_{3z^2-r^2} \end{array}
\begin{array}{c}
\begin{array}{cccc} s^c & s^a & d^c_{x^2-y^2} & d^c_{3z^2-r^2} \end{array} \\
\begin{pmatrix} \epsilon^c_s & 4E_{ss} & 0 & 0 \\ 4E_{ss} & \epsilon^a_s & 0 & 0 \\ 0 & 0 & \epsilon^c_d & 0 \\ 0 & 0 & 0 & \epsilon^c_d \end{pmatrix}
\end{array}
$$

$$
\begin{array}{c} \\ p^c_x \\ p^c_y \\ p^c_z \\ d^c_{xy} \\ d^c_{yz} \\ d^c_{zx} \\ p^a_x \\ p^a_y \\ p^a_z \end{array}
\begin{array}{c}
\begin{array}{ccccccccc} p^c_x & p^c_y & p^c_z & d^c_{xy} & d^c_{yz} & d^c_{zx} & p^a_x & p^a_y & p^a_z \end{array} \\
\begin{pmatrix}
\epsilon^c_p & 0 & 0 & 0 & 0 & 0 & 4E_{xx} & 0 & 0 \\
0 & \epsilon^c_p & 0 & 0 & 0 & 0 & 0 & 4E_{xx} & 0 \\
0 & 0 & \epsilon^c_p & 0 & 0 & 0 & 0 & 0 & 4E_{xx} \\
0 & 0 & 0 & \epsilon^c_d & 0 & 0 & 0 & 0 & 4E_{pd} \\
0 & 0 & 0 & 0 & \epsilon^c_d & 0 & 4E_{pd} & 0 & 0 \\
0 & 0 & 0 & 0 & 0 & \epsilon^c_d & 0 & 4E_{pd} & 0 \\
4E_{xx} & 0 & 0 & 0 & 4E_{pd} & 0 & \epsilon^a_p & 0 & 0 \\
0 & 4E_{xx} & 0 & 0 & 0 & 4E_{pd} & 0 & \epsilon^a_p & 0 \\
0 & 0 & 4E_{xx} & 4E_{pd} & 0 & 0 & 0 & 0 & \epsilon^a_p
\end{pmatrix}
\end{array}
$$

where the onsite s, p and d energies of cation are given by ϵ^c_s, ϵ^c_p and ϵ^c_d respectively, while the onsite s and p energies of the anion are given by ϵ^a_s and ϵ^a_p. The inter-atomic matrix elements are given by the Slater Koster parameters [52] as given below:

E_{ss}= $V_{ss\sigma}$

E_{xx}= $V_{pp\sigma}/3 + 2V_{pp\pi}/3$

and E_{pd}= -$V_{pd\sigma}/3 + 2V_{pd\pi}/(3\sqrt{3})$

Bibliography

[1] J. H. Edgar, Editor, *Properties of Group III Nitrides*, EMIS Datareviews, vol. 11, INSPEC, London (1994).

[2] M. Kondow, K. Uomi, K. Hosomi, and T. Mozume, J. Appl. Phys. **33**, L1056 (1994); J. S. Harris, Semicond. Sci. Technol. **17**, 880 (2002); H. Riechert, A. Ramakrishnan, and G. Steinle, *ibid.* **17**, 892 (2002).

[3] D. J. Firedman, J. F. Geisz, S. R. Kurtz, and J. M. Olson, J. Crystal. Growth **195**, 409 (1998); J. F. Geisz, and D. J. Firedman, Semicond. Sci. Technol. **17**, 769 (2002).

[4] L. Bellaiche, S. H. Wei, and A. Zunger, Phys. Rev. B. **56**, 10233 (1997); H. P. Xin, C. W. Tu, Y. Zhang, and A. Mascarenhas, Appl. Phys. Lett. **76**, 1267 (2000); W. Shan, W. Walukiewicz, K. M. Yu. J. Wu, J. W. Ager III, E. E. Haller, H. P. Xin, and C. W. Tu, Appl. Phys. Lett. **76**, 3251 (2000); I. A. Buyanova, G. Pozina, J. P. Bergman, W. M. Chen, H. P. Xin, and C. W. Tu, Appl. Phys. Lett. **81**,52 (2002).

[5] K. Momose, H. Yonezu, Y. Fujimoto, Y. Furukawa, Y. Motomura, and K. Aiki, Appl. Phys. Lett. **79**, 4151 (2001); H. Yonezu, Semicond. Sci. Technol. **17**, 762 (2002).

[6] C. Y. Liu, S. F. Yoon, Z. Z. Sun, and K. C. Yew, Appl. Phys. Lett. **88**, 081105 (2006); C. Y. Liu, S. F. Yoon, Q. Cao, C. Z. Tong, and Z. Z. Sun, Nanotechnology **17**, 5627 (2006); Q. Gao, M. Buda, H. H. Tan, and C. Jagadish, Electrochem. Solid-State Lett. **8**, G57 (2005); Z. Z. Sun, S. F. Yoon, K. C. Yew, B. X. Bo, D. A. Yan, and T. C. Hang, Appl. Phys. Lett. **85**, 1469 (2004); S. Makino, T. Miyamoto, T. Kageyama, N. Nishiyama, F. Koyama, and K. Iga, J. Cryst. Growth **221**, 561 (2000).

[7] M. L. Reed, N. A. El-Masry, H. H. Stadelmaier, M. K. Ritums, M. J. Reed, C. A. Parker, J. C. Roberts, and S. M. Bedair, Appl. Phys. Lett. **79**, 3473 (2001); S. E. Park, H. Lee, Y.C. Cho, and S. Jeong, Appl. Phys. Lett. **80**, 4187 (2002).

[8] See *Materials Research Bulletin*, Sept 2006 for a recent collection of reviews.

[9] D. Vanderbilt, Phys. Rev. B **41**, 7892 (1990).

[10] P. E. Blöchl, Phys. Rev. B **50**, 17953 (1994).

[11] V. Fiorentini, M. Methfessel, and M. Scheffler, Phys. Rev. B **47**, 13353 (1993).

[12] B. Bouhafs, F. Litimein, Z. Dridi, and P. Ruterana, Phys. Stat. Sol. (b),**1**, 61 (2003).

[13] G. Kresse and J. Joubert,Phys. Rev. B **59**, 1758 (1999).

[14] J.P. Perdew and Y. Wang, Phys. Rev. B **45**, 13244 (1992).

[15] F. D. Murnaghan, Proc. Natl. Acad. Sci. U.S.A. **30**, 244 (1944).

[16] R. O. Jones and O. Gunnarsson, Rev. Mod. Phys. **61**, 689 (1989).

[17] P. Hohenberg and W. Kohn, Phys. Rev **136**, B864 (1964).

[18] D. M. Ceperley and B.J. Alder, Phys. Rev. Lett. **45**, 566 (1980) as parametrised by J.P. Perdew and Zunger in [19].

[19] J. P. Perdew and A. Zunger, Phys. Rev B **23**, 5048 (1981).

[20] J. P. Perdew, K. Burke and M. Ernzerhof, Phys. Rev. Lett. **77**, 3865 (1996).

[21] Martin R M 2004 *Electronic Structure: Basic Theory and Practical Methods* (Cambridge University Press).

[22] F. Aryasetiawan and O. Gunnarsson, Rep. Prog. Phys.**61**, 237 (1998).

[23] S. H. Wei and A. Zunger, Phys. Rev. B **37**, 8958 (1998); P. Schröer, P. Krüge, and J. Pollmann, Phys. Rev. B **47**, 6971 (1993); P. Schröer, P. Krüge, and J. Pollmann, Phys. Rev. B **48**, 18264 (1993); S. B. Zhang, S. H. Wei, and A. Zunger, Phys. Rev. B **52**, 13975 (1995).

[24] W. R. Lambrecht, A. V. Rodina, S. Limpijumnong, B. Segall, and B. K. Meyer, Phys. Rev. B **65**, 075207 (2002); S. Zh. Karazhanov, P. Ravindran, U. Grossner, A. Kjekhus, H. Fjellvag, and B. G. Svensson, J. Cryst. Growth **287**, 162 (2006); S. Zh. Karazhanov, P. Ravindran, U. Grossner, A. Kjekhus, H. Fjellvag, and B. G. Svensson, J. Appl. Phys. **100**, 043709 (2006); H. C. Choi, S. K. Kwon, B. I. Min, and F. Aryasetiawan, J. Korean Phys. Soc. **53** 967 (2008).

[25] V. I. Anisimov, I. V. Solovyev, M. A. Korotin, M. T. Czyzyk, and G. A. Sawatzky, Phys. Rev. B **48**, 16929 (1993). A. I. Liechtenstein, V. I. Anisimov, and J. Zaanen, Phys. Rev. B **52**, R5467 (1995).

[26] S. L. Dudarev, G. A. Botton, S. Y. Savrasov, C. J. Humphreys, and A. P. Sutton, Phys. Rev. B. **57** 1505 (1998).

[27] A. Janotti, D. Segev, and C. G. Van de Walle, Phys. Rev. B **74**, 045202 (2006).

[28] N. J. Shevchick, J. Tejeda, and M. Cardona, Phys. Rev. B. **9**, 2627 (1971).

[29] G. Martin, A. Botchkarev, A. Rockett, and M. Morkoc, Appl. Phys. Lett. **68**, 2541 (1996).

[30] C. G. Van de Walle, Phys. Rev. B **39**, 1871 (1989).

[31] S. H. Wei and A. Zunger, Phys. Rev. Lett. **59**, 144 (1987).

[32] J. Singh, *Physics of Semiconductors and Their Heterostructures* (McGraw-Hill, New York, 1993);

[33] R. L. Anderson, Solid-State Electron. **5**, 341 (1962). A. G. Milnes and D. L. Fuecht, *Heterojuctions and Metal-Semiconductor Junctions* (Academic Press, New York, 1972).

[34] J. O. McCaldin, T. C. McGill, and C. A. Mead, Phys. Rev. Lett. **36**, 56 (1976).

[35] J. Menendez, A. Pinczuk, D. J. Werder, J. P. Valladares, T. H. Chiu, and W. T. Tsang, Solid State Commun. **61**, 703 (1987).

[36] H. Kroemer, J. Vac. Sci. Technol. B **2**, 433 (1984).

[37] W. R. Frensley and H. Kroemer, J. Vac. Sci. Technol. **13**, 810 (1976).

[38] W. A. Harrison, J. Vac. Sci. Technol. **14**, 1016 (1977).

[39] W. R. Frensley and H. Kroemer, Phys. Rev. B **16**, 2642 (1977).

[40] R. C. Miller, D. A. Kleinman, and A. C. Gossard, Phys. Rev. B **29**, 7085 (1984).

[41] C. G. Van de Walle and R. M. Martin, Phys. Rev. B **35**, 8154 (1987).

[42] D. M. Bylander and L. Kleinman. Phys. Rev. B **36**, 3229 (1987).

[43] D. M. Bylander and L. Kleinman. Phys. Rev. Lett. **59**, 2091 (1987).

[44] A. Baldereschi, S. Baroni, and R. Resta. Phys. Rev. Lett. **61**, 734 (1988).

[45] S. P. Kowalczyk, J. T. Cheung, E. A. Kraut, and R. W. Grant, Phys. Rev. Lett. **56**, 1605 (1986); T. M. Duc, C. Hsu, and J. P. Faurie, *ibid.* 58, 1127 (1987).

[46] S. H. Wei and A. Zunger, Appl. Phys. Lett. **72**, 2011 (1998).

[47] T. Lei, T. D. Moustakas, R. J. Graham, Y. He, and S. J. Berkowitz, J. Appl. Phys. **71**, 4933 (1992).

[48] M. Sugawara, Phys. Rev. B **47**, 7588 (1993).

[49] W. A. Harrison, *Electronic Structure and Properties of Solids*, (Freeman, San Francisco, 1980).

[50] E. T. Yu, D. H. Chow, and T. C. McGill, Phys. Rev. B **38**, 12764 (1988); K. Hirakawa, Y. Hashimoto, and T. Ikoma, Appl. Phys. Lett. **57**, 2555 (1990).

[51] R. Viswanatha, S. Sapra, T. Saha-Dasgupta, and D.D. Sarma, Phys. Rev. B **72**, 045333 (2005).

[52] J. C. Slater and G. F. Koster, Phys. Rev. **94**, 1498 (1954).

Chapter 4

Quantum confinement of nanostructures

In this chapter we have examined two aspects of nanostructures, the first being the evolution of the electronic structure of quantum wells of the most well-studied materials GaAs/AlAs and the second being the evolution of the conduction band bottom as a function of nanoparticle size of semiconductor quantum dots.

4.1 GaAs/AlAs heterostructures

4.1.1 Introduction to heterostructures

A semiconductor heterostructure is formed when two different semiconductors are grown in contact. The layer thicknesses in heterostructures can be controlled over a length scale comparable to or smaller than the electron de Broglie wavelength. This results in novel quantum effects related to size. Quantum well structures can be designed to perform special functions that are the core of many modern quantum devices. For example, quantum well laser and high electron mobility transistor (HEMT) are well-developed quantum devices. Quantum well lasers are extensively employed in optical communication systems, bar-code scanners, laser arrays and optical disc readers/writers; whereas HEMTs are used in low-noise receivers, digital integrated circuits and microwave circuits [1].

In practice, different semiconductors are "brought into contact" by epitaxially growing one semiconductor on top of another semiconductor. To date, the fabrication of the heterostructures by epitaxial method, such as Molecular Beam Epitaxy (MBE) and

Metal-Organic Vapor-Phase Epitaxy (MOVPE), is the cleanest and the most reproducible method available. Since the two materials usually have different band gaps the properties of the materials significantly change at the interface. To prevent any dislocation formation due to any strain effects it is preferred to have lattice matched heterostructures.

The magnitudes of the changes in the band-edge energies are critically important for many semiconductor devices. The double junction heterostructures are known as quantum wells (QW) and the multi-junction structures as superlattices (SL) or multiple quantum wells (MQW). The types of band alignments in quantum wells is classified according to the relative ordering of the band-edge energies as shown in the Fig. 4.1.

The most common (and generally considered to be the "normal") alignment is the straddling configuration. However, the band gaps need not entirely overlap. The conduction band of the smaller-gap material might lie above that of the larger-gap material, or its valence band might lie below that of the larger-gap material. Such a band alignment is called staggered. The staggering might become so extreme that the band gaps cease to overlap. This situation is known as a broken gap. From the engineering point of view, straddling is known as type-I while staggered and broken are known as type-II. In type-I quantum wells electrons and holes are confined in the same layers, while in type-II quantum wells electrons and holes are not spatially confined in the same region. In usual semiconductor after the photoexcitation electrons and holes typically stay in the same region which results in the maximized wavefunction overlap of the electron and hole and thus yielding a high radiative recombination rate. This is what is observed in type-I heterostructures, which makes it ideal in light emitting devices. However in many of the other devices like in dye-sensitized solar cells [2] and even in the usual solar cells the efficient charge separation of the electron and hole after photoexcitation is highly preferred. In type-II heterostructures the photogenerated carriers are spatially separated such that the electron wavefunction mainly resides in one semiconductor while the hole wavefunction in the other, which make them ideal materials for photovoltaic devices for its long range photoinduced charge separation, which can efficiently separate photo-generated electron-hole pairs in each semiconductor material and reduce their recombination [3]. The recombination times of electrons and holes are long in type-II heterostructures.

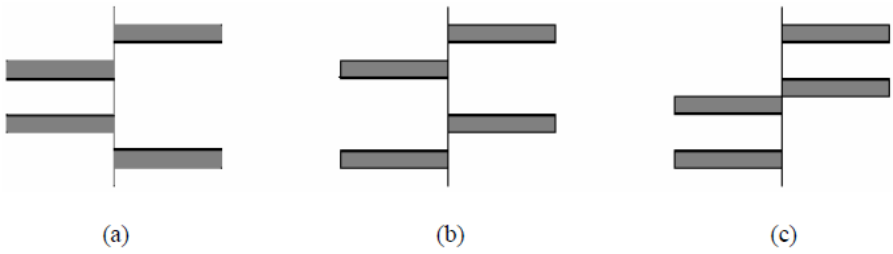

Figure 4.1: Types of band alignment (a) straddling (b) staggered (c) broken

Experimentally, quantum wells are formed by sandwiching a narrower band gap semiconductor (the well) with the wider band gap materials as adjacent layers (the barriers) and thereby attaining type-I arrangement. The relative heights of the discontinuities in the conduction band (CB) and valence band (VB) edges are intrinsic properties of the two materials involved. The motion of the electrons in the x-y plane is unrestricted. Thus, the one-dimensional confinement effect occurs in QW which is used to engineer the electronic properties of the materials [4]. The width of the quantum well determines whether the confinement effect will be important. The properties of the QW is determined by the band gap energies and by the chemical composition and thickness of the layers.

4.1.2 What is know about GaAs/AlAs superlattices

These systems have been extensively studied by means of optical and/or electrical measurements as well as numerous calculations with varying degrees of sophistication. In all the different cases studied in these superlattices, where the thickness of GaAs and AlAs were changed, the top of the valence band is always confined to the GaAs region, while localization of the conduction band bottom in the AlAs or GaAs region depends on the thickness of the layers considered.

J. Ihm [5] studied the effects of the layer thickness on the electronic character in GaAs/AlAs superlattices using an empirical tight binding method. Here they identify

three regions of the short-period superlattices based upon m (number of monolayers in each GaAs layers) and n (number of monolayers in each AlAs layers). Each monolayer thickness is half the lattice constant of the material, ie having 2 atomic layers i.e., Al and As or Ga and As. In region I (m > 10 and n= any value) the lowest electronic states are in the Γ states in the GaAs layers. In region II (m < 10 , n> m) the lowest conduction band states are in the X states in the AlAs layers. They observe an intermediate region III, with m > n and both n and m < 10, where the superlattice exhibits alloy-like behavior (giving rise to both direct and indirect gap for certain m and n values). The transition between region I and region II superlattices is not abrupt.

Combining the techniques of photo-luminescence and photo-luminescence excitation spectroscopy K. J. Moore *et al.* [6] mapped out both direct Γ-related band gap and X-Γ band gap as a function of AlAs thickness. They observed that for the fixed GaAs thickness at 25 Å the band alignment shows type-II when the AlAs thickness is greater than 15 Å. For AlAs thickness less than 10 Å they observed a type-I behavior. They could adequately describe the electronic states by the envelope function approach, where one of the main parameters determining the energies of the quantum confined systems is the effective mass.

M. C. Munoz *et al.* [7] carried out empirical tight binding studies on GaAs/AlAs superlattices, over a broad range of values of n and m ((2,2)<=(n,m)<=(22,22)), classified the superlattice into four different regions depending on the type of band alignment as a function of (n,m). The four region are classified as follows: Region I- The gap is direct and the amplitude is confined to GaAs. This corresponds approximately to the region I of J. Ihm studies [5]. Region II- The lowest conduction band state is confined to the AlAs layers. In bulk AlAs crystal this would be an X state and the gap would be indirect, but here the conduction band minimum is at the Γ point and the gap is direct. Electron and holes are separated in real space but the two band extrema have the same momentum in the reciprocal space of the superlattice. Region III- This is an intermediate zone between the region I and region II where the superlattice has direct band gap and the spectral strength of the bottom of the conduction band is distributed between the two constituents. Region IV- Here the electrons and holes separated in both real and momentum space. This region is found in [5] but [7] finds the same for much smaller range of (n,m) values.

R. Cingolani *et al.* [8] studied the transition from a type-I to type-II superlattice occurring in $GaAs_m/AlAs_n$ ultra-short-period superlattices at certain critical layer thicknesses using spectroscopic techniques. They also compared their experimental data's with theoretical calculations for the quantized sub-bands in the superlattices employing a Kronig-Penny formalism based on the Bastard envelope function approximation [9]. They found the crossover between the direct and indirect optical transition occurs when the well and barrier are each composed of 12 monolayers.

J. G. Menchero *et al.* [10] studied the band-edge states for GaAs quantum well embedded in AlAs spacer layers, near the critical well width for which the fundamental transition goes from direct to indirect. Studies were done using real space tight-binding analysis and the results were compared with models taking first (1NN) and second nearest neighbor interactions (2NN) into account. Both 1NN and 2NN models provided the same description of the first hole state. For the first electron state, however, important differences arise. Although the critical width is the same in both models, for the 2NN approach the indirect-gap regime is characterized by the wavefunction escaping from the well into the AlAs barriers, but keeping the same translational symmetry. In the 1NN approach, the transition is characterized by a change in translational symmetry, and the wavefunction may or may not remain localized in the well. Their 2NN approach is in complete agreement with the theoretical results of Franceschetti and Zunger [11] which is based on an empirical pseudopotential approach.

Till now there is no *ab-initio* work in this regime and this makes our work important. Here we also track the evolution of the wavefunction, corresponding to the first hole state and first electron state, as a function of well size as well as under negative pressure.

4.1.3 Methodology

In the present work we consider GaAs/AlAs (001) superlattices with fixed total number of principal layers (n+m=48). Here n (m) is the number of principal layers of AlAs (GaAs). Each principal layer (layer) includes two atomic layers of cation and anion, thus resulting in a total of 96 atomic layers in these superlattices. All the calculations presented here are performed within a supercell scheme. Our supercell is constructed

from a 1x1x24 zinc-blende cubic cell (lattice constant was kept at the experimental lattice constant of the material i.e., 5.65 Å) and contains 192 atoms in total. Here we consider full optimization of the internal positions. In order to study the effect of pressure on there superlattices we considered a larger lattice constant of 5.73 Å which is the theoretical optimized lattice constant. We use periodic boundary conditions in all directions. GGA-PW91 approximation [12] has been used for the exchange. A dense Γ centered k-points grid of 6x6x1 was used in the calculations. The energy cutoff used for the kinetic energy of the plane waves used in the basis was 240.4 eV.

4.1.4 Results and Discussion

Few monolayers of GaAs sandwiched between AlAs layers : Studies near the critical GaAs thickness where the system undergoes a transition from type-II to type-I superlattice

In Fig. 4.2 we have plotted the planar averaged charge density corresponding to the valence band maximum as a function of the growth direction for 7, 11, 15, 19 and 23 atomic layers of GaAs sandwiched between AlAs. The position of Al, Ga and As atoms has also been indicated. As one expects the primary contribution to the valence band maximum is from the As atomic layer and this is indeed what we find and the peaks in the charge density occur in the As atomic layer and the minima occur in the atomic layers containing the cation site. The boundaries of the quantum well have been indicated by dashed lines. The wavefunction corresponding to the valence band maximum is localized primarily in the GaAs well region as is expected. A small portion tunnels into the AlAs barrier region also. Interestingly the percentage of charge density that has tunneled through increases with quantum confinement (Table.4.1). This can be understood in the following manner. With increased quantum confinement, the separation between the valence band maximum of GaAs and AlAs decreases, hence the effective barrier. This results in increased tunneling. A consequence of the increased quantum confinement on the conduction band edge brings about a reversal with the conduction band minimum of AlAs being lower than that of GaAs at 7 and 11 atomic layers. This corresponds to a well thickness of 19.8 Å and is slightly less than the thickness of 25 Å found by pseudopotential and tight binding approaches [11, 10]. The charge density corresponding

to the conduction band minimum of the 7 and 11 atomic layers is shown in Fig. 4.3. As a consequence of the type-II transition discussed above, the wavefunction here is localized in the AlAs region. For thicker GaAs well regions there is an abrupt transition to type-I behavior. The charge density profile after the transition (Fig. 4.4) does not show an oscillatory behavior as observed in Figs. 4.2 and 4.3.

While a fully atomistic approach is useful, most of the physical insight into the problem has been obtained from empirical approaches. So the first question we asked was where are the deviations. Merely capturing the strong oscillations of the wavefunctions did not seem reason enough to carry out this computationally demanding exercise which has not been done before because of the computational costs. Well there were suprises.

The simplest approximation to the particle in a potential well is the textbook example of a particle in a box with finite barriers where realism is maintained by using the effective mass derived from the bulk band structure for the hole and electron respectively. The ground state wavefunction for the problem consists of a nodeless sine/cosine function in the well region which decays exponentially into the barrier region and may be solved numerically. The envelope of the charge density plot of the conduction band minimum should correspond to the result expected from the effective mass approach. A similar analysis is valid for a hole at the top of the valence band.

Armed with this expectation we first examine the envelope of the charge density corresponding to the valence band maximum for 7, 11, 15, 19 and 23 atomic layers of GaAs (Fig. 4.5). This is expected from the particle in a finite potential well problem. In addition to the outer envelope (corresponding to the maxima of the charge density) we have also plotted the inner envelope (corresponding to the minima of the charge density).

In the effective mass approximation the inner envelope should be zero and this is what we find largely. When we examine the results for the conduction band minima (Fig. 4.6) for the 7 and 11 atomic layers, the outer envelope offers no suprise. However the inner envelope is suprisingly large with a shape very similar to the outer envelope. This is a consequence of the significant weight of the wavefunction in this case on both the cations and anions. The profile of the outer envelope changes drastically when we consider 15, 19 and 23 atomic layers of GaAs comprising the well region (Fig. 4.7). This has been

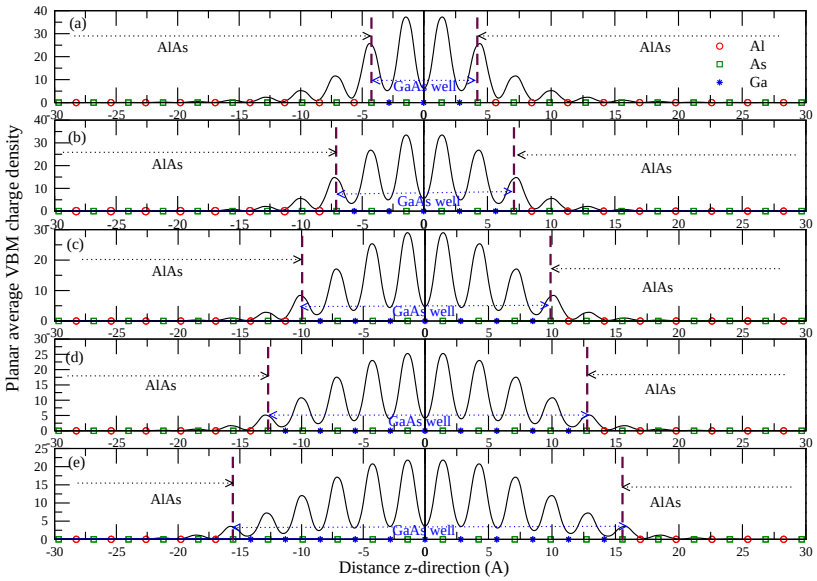

Figure 4.2: Variation of the planar averaged charge density plot of the VBM for (a) 7, (b) 11, (c) 15, (d) 19, and (e) 23 atomic layers of GaAs sandwiched cases in the fixed GaAs/AlAs 96 atomic layer superlattice. The interface As layer is shown by dashed lines.

observed earlier in the simple tight binding models by Menchero *el al.* [10] and suggests that the approximation to a simple potential well problem is not valid and the potential is far more complicated.

We then went on to examine the effects of pressure. For this purpose we considered the theoretical lattice constant of GaAs and compared the results. Fig. 4.8 shows that the valence band maximum charge density profile for the 7 atomic layers where the atomistic variations as well as the outer envelope are shown in the same plot. There are no suprises here. Moving to the conduction band minimum charge density (Fig. 4.9) we find that the unlike at the lattice constant of 5.65 Å, here, the band alignment is type-I. Thus the effect of a small negative pressure is sufficient to offset the type-I to type-II transition observed earlier.

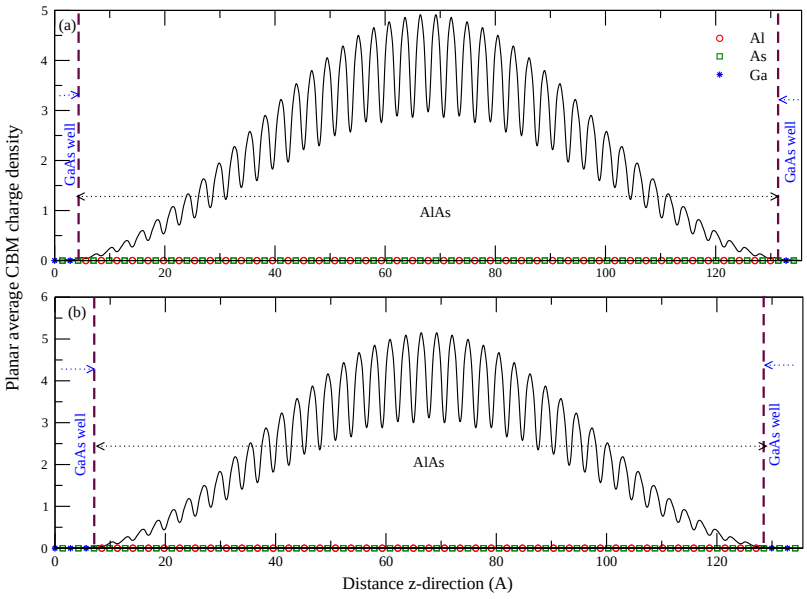

Figure 4.3: Variation of the planar averaged charge density plot of the CBM for (a) 7 and (b) 11 atomic layers of GaAs sandwiched cases in the fixed GaAs/AlAs 96 atomic layer superlattice. The interface As layer is shown by dashed lines.

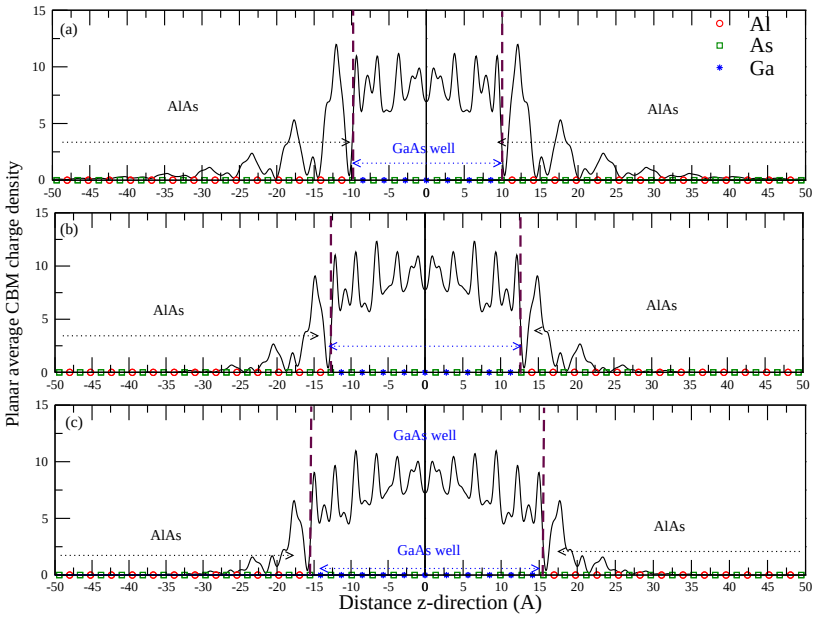

Figure 4.4: Variation of the planar averaged charge density plot of the CBM for (a) 15, (b) 19, and (c) 23 atomic layers of GaAs sandwiched cases in the fixed GaAs/AlAs 96 atomic layer superlattice. The interface As layer is shown by dashed lines.

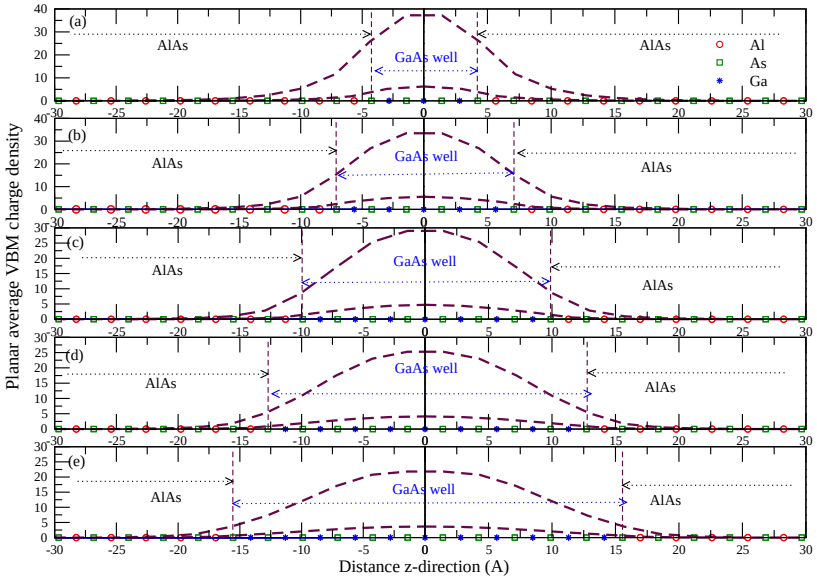

Figure 4.5: Variation of the outer and inner envelope of the planar averaged charge density plot of the VBM for (a) 7, (b) 11, (c) 15, (d) 19, and (e) 23 atomic layers of GaAs sandwiched cases in the fixed GaAs/AlAs 96 atomic layer superlattice. The interface As layer is shown by dashed lines.

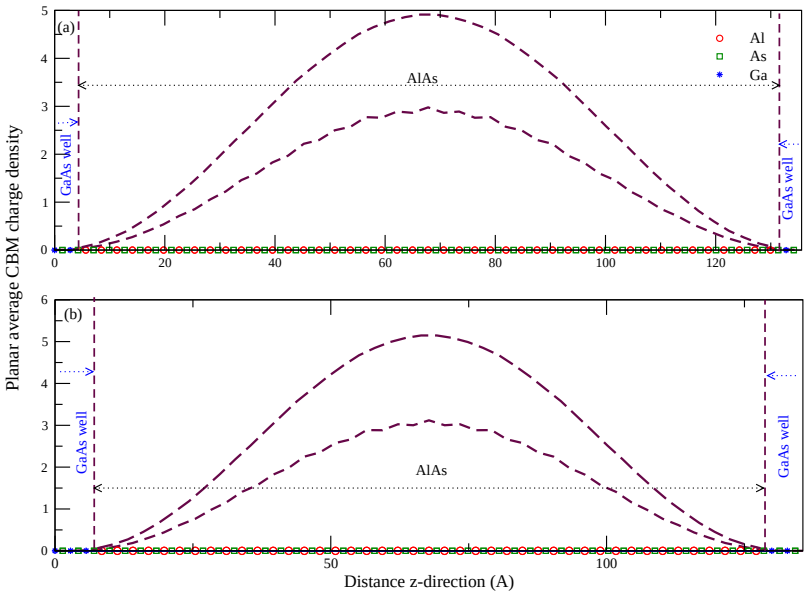

Figure 4.6: Variation of the outer and inner envelope of the planar averaged charge density plot of the CBM for (a) 7 and (b) 11 atomic layers of GaAs sandwiched cases in the fixed GaAs/AlAs 96 atomic layer superlattice. The interface As layer is shown by dashed lines.

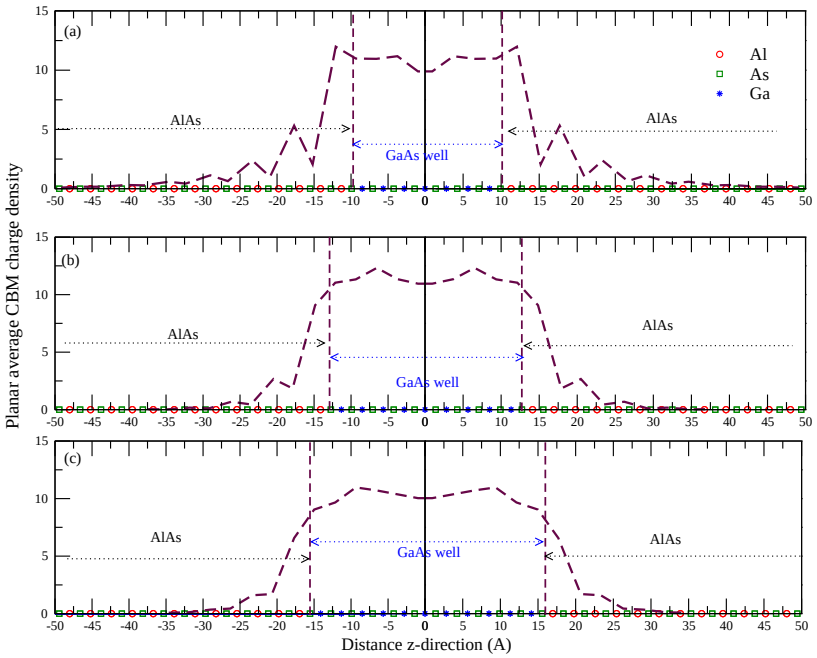

Figure 4.7: Variation of the envelope of the planar averaged charge density plot of the CBM for (a) 15, (b) 19, and (c) 23 atomic layers of GaAs sandwiched cases in the fixed GaAs/AlAs 96 atomic layer superlattice. The interface As layer is shown by dashed lines.

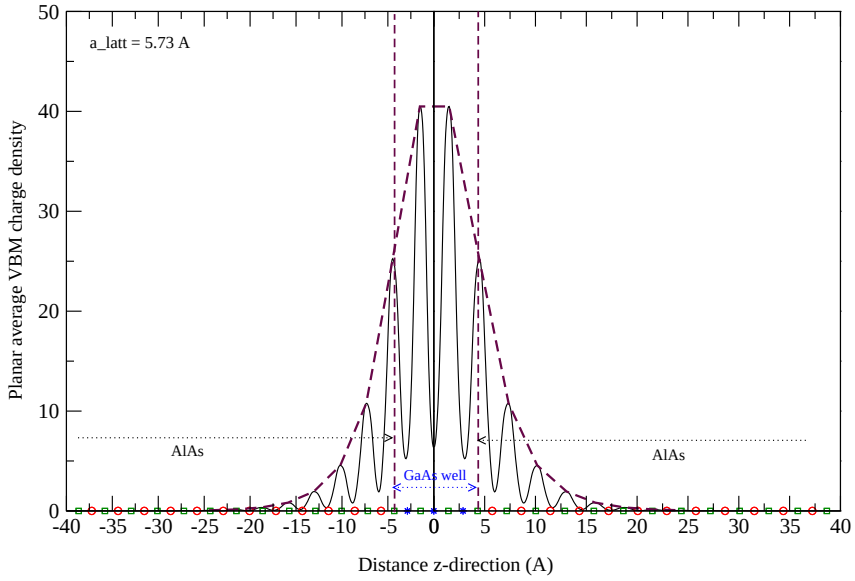

Figure 4.8: Variation of the planar averaged charge density plot of the VBM for 7 atomic layers of GaAs sandwiched cases in the fixed GaAs/AlAs 96 atomic layer superlattice with a lattice constant of 5.73 Å. The interface As layer is shown by dashed lines. The envelope of the plot is marked in thick dashed line.

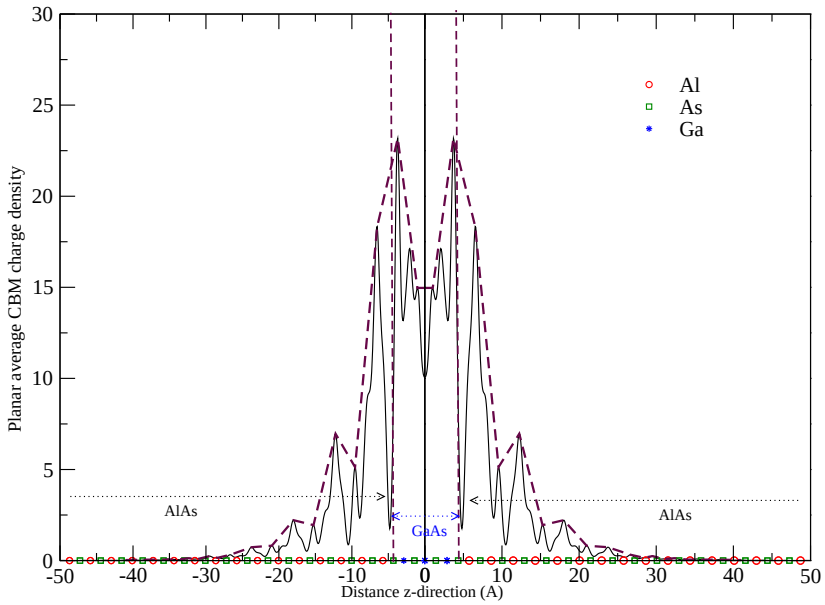

Figure 4.9: Variation of the planar averaged charge density plot of the CBM for 7 atomic layers of GaAs sandwiched cases in the fixed GaAs/AlAs 96 atomic layer superlattice with a lattice constant of 5.73 Å. The interface As layer is shown by dashed lines. The envelope of the plot is marked in thick dashed line.

Table 4.1: Percentage of VBM and CBM contribution in the GaAs well region for different sizes of well sizes considered in the fixed GaAs/AlAs 96 atomic layer superlattice.

Number of layers in the well region			well size	Percentage Contribution of	
Ga	As	total atomic layers	(Å)	VBM	CBM
3	4	7	8.5	59	0.04
5	6	11	14.2	79	0.04
7	8	15	19.8	89	60
9	10	19	25.5	94	79
11	12	23	31.1	96	85

Moving to other limit : Few monolayers of AlAs sandwiched between GaAs layers

We then considered the other limit where we had few atomic layers of AlAs sandwiched between GaAs. There should be no confinement of either electrons or holes in the present case. Plotting the valence band charge density (Fig. 4.10) we find that the wavefunction is localized in the GaAs region with no tunneling into the AlAs region.

The envelope of the conduction band minimum charge density for 7, 11, 15, 19 and 23 atomic layers of AlAs sandwiched in the 96 atomic layer superlattice of GaAs/AlAs is shown in Fig. 4.11. Tunneling is found into the AlAs layer upto around two atomic layers. A closer analysis of the plots reveals suprises. For 7 AlAs atomic layers one finds the envelope of the charge density corresponding to the valence band maximum takes on a beat-like profile with several Fourier components (Fig. 4.12 (a)). Increasing the lattice constant to 5.73 Å one finds that the envelope for the same number of atomic layers resembles a sine function (Fig. 4.12 (b)). The emergence of several Fourier components indicates the emergence of some super structure (Fig. 4.13). This is clearest for n=7 layers of AlAs sandwiched between GaAs. At a lattice constant of 5.73 Å, one finds a buildup of charge density away from the centre of the potential well. The almost two humped structure that one finds could arise from a scenario where the electron wavefunction redistributes itself to minimize the Coulomb repulsion energy. This is the reason it is more prominent in the larger lattice constant cases. Further modelling will be done in terms of microscopic models to see if one can capture this regime for GaAs/AlAs with

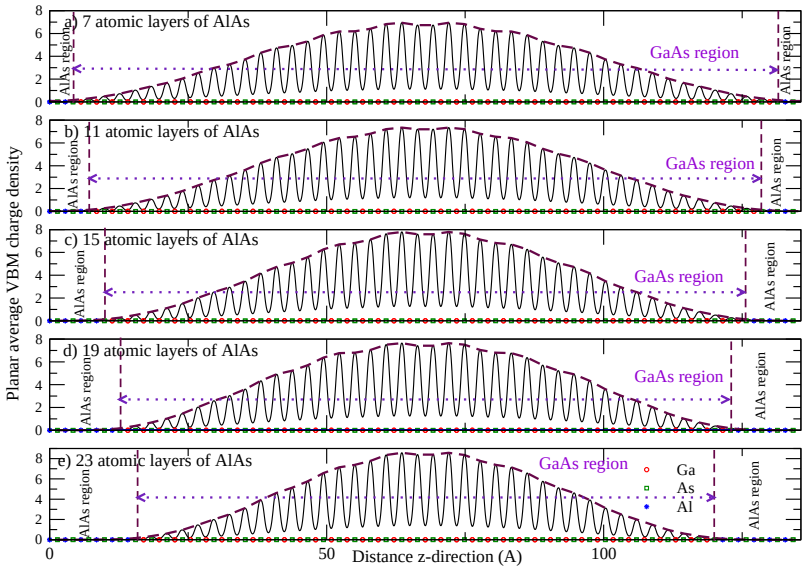

Figure 4.10: Variation of the planar averaged charge density plot of the VBM for (a) 7, (b) 11, (c) 15, (d) 19, and (e) 23 atomic layers of AlAs sandwiched cases in the fixed GaAs/AlAs 96 atomic layer superlattice. The interface As layer is shown by dashed lines. The envelope of the plot is also marked.

realistic parameters.

4.1.5 Conclusion

Studies on GaAs/AlAs superlattices varying the GaAs and AlAs layers, but keeping the total number of layers of the superlattice fixed, were done. Here we studied the type of band alignment and the nature the VBM and CBM wavefunction envelope in different cases considered. When we have few GaAs layers sandwiched between the AlAs layers we see a transition of the superlattice from type-II to type-I. The critical thickness of the GaAs well at which the transition occurs was found to be around 20 Å. Studying the other limit were few AlAs is sandwiched between the GaAs layers we see that the superlattice is

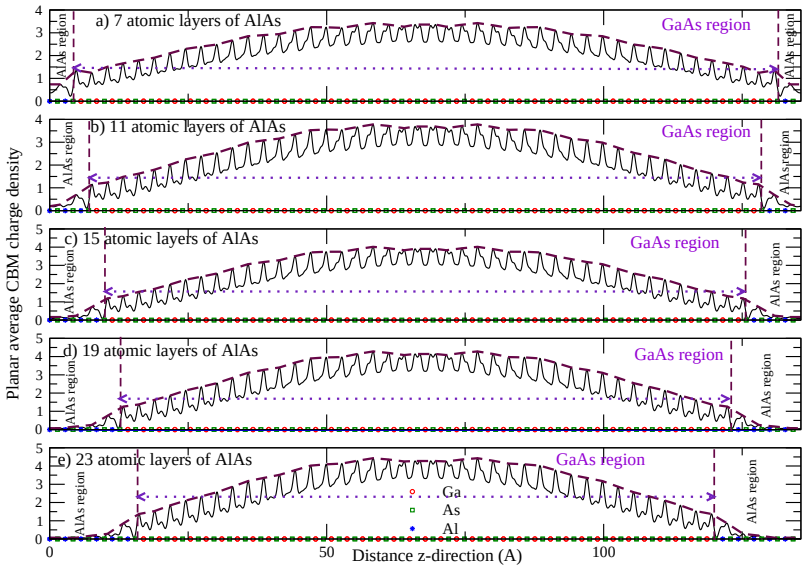

Figure 4.11: Variation of the planar averaged charge density plot of the CBM for (a) 7, (b) 11, (c) 15, (d) 19, and (e) 23 atomic layers of AlAs sandwiched cases in the fixed GaAs/AlAs 96 atomic layer superlattice. The interface As layer is shown by dashed lines. The envelope of the plot is also marked.

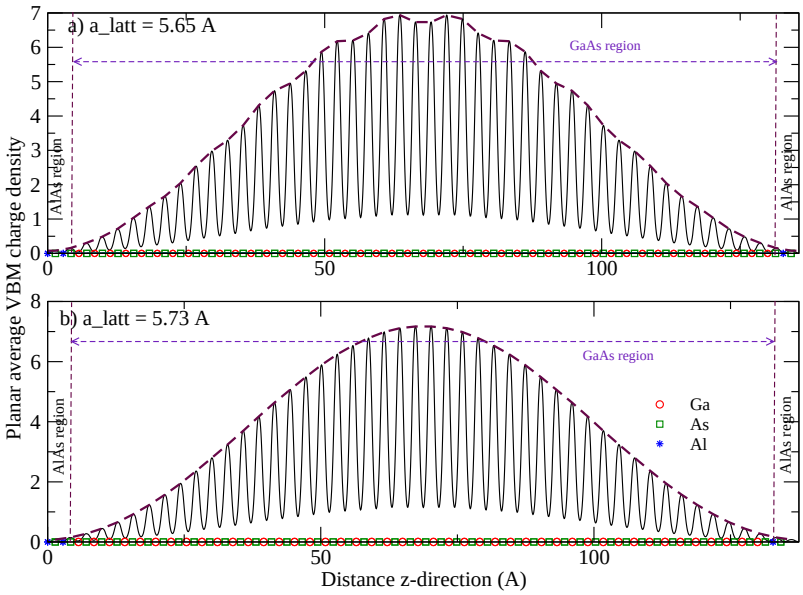

Figure 4.12: Variation of the planar averaged charge density plot of the VBM for 7 atomic layers of AlAs sandwiched cases in the fixed GaAs/AlAs 96 atomic layer superlattice with a lattice constant of (a) 5.65 and (b) 5.73 Å. The interface As layer is shown by dashed lines. The envelope of the plot is marked in thick dashed line.

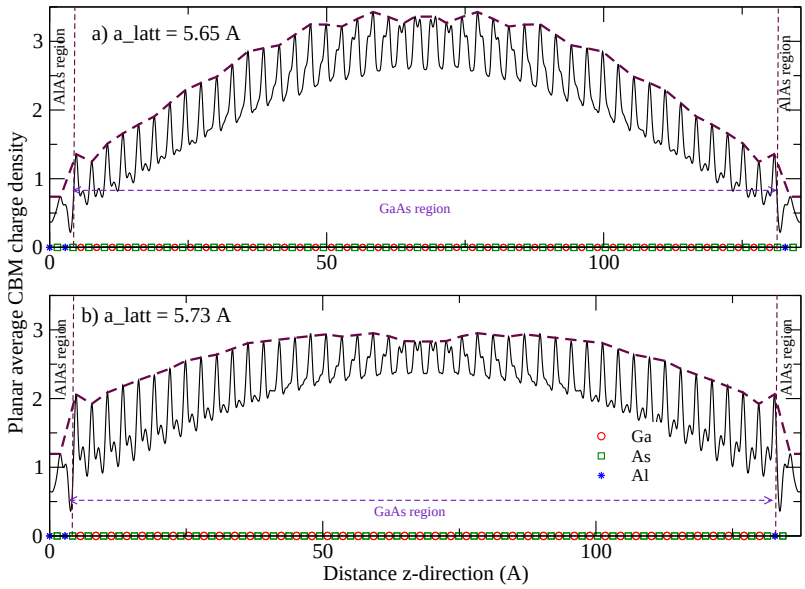

Figure 4.13: Variation of the planar averaged charge density plot of the CBM for 7 atomic layers of AlAs sandwiched cases in the fixed GaAs/AlAs 96 atomic layer superlattice with a lattice constant of (a) 5.65 and (b) 5.73 Å. The interface As layer is shown by dashed lines. The envelope of the plot is marked in thick dashed line.

always type-I. Our studies on VBM wavefunctions i.e., the ground state wavefunction of the holes, agrees quite well with the nature of the ground state wavefunction one expects from a particle in a potential well problem while the CBM wavefunctions (the ground state wavefunction of the electrons) deviates from the particle in a potential well problem for certain n (m) layer sizes.

4.2 Size dependence on the conduction band minimum of semiconductor nanocrystals

4.2.1 Introduction

One of the defining features of a semiconductor is the energy gap separating the conduction and valence energy bands. The color of light emitted by the semiconductor material is determined by the width of the gap. In semiconductors of macroscopic sizes- bulk semiconductors -the gap width is a fixed parameter determined by the materials identity. The situation changes, however, in the case of nanoscale semiconductor particles with sizes smaller than about 10 nanometers. This size range corresponds to the regime of quantum confinement, for which the spatial extent of the electronic wave function is comparable with the dot size. As a result of these geometrical constraints, electrons feel the presence of the particle boundaries and respond to changes in particle size by adjusting their energy. This phenomenon is known as the quantum-size effect, and it plays a very important role in quantum dots (QDs). The size regime in which one has such size dependence varies from material to material and could be as large as 200 Å for PbS or as small as 40 Å for CdSe. In the first approximation, the quantum-size effect can be described by a simple "quantum box" model in which the electron motion is restricted in all three dimensions by impenetrable walls. For a spherical QD with radius R, this model predicts that a size dependent contribution to the energy gap is simply proportional to $1/R^2$, implying that the gap increases as the QD size decreases. In addition, quantum confinement leads to a collapse of the continuous energy bands of a bulk material into discrete, atomic-like energy levels. The discrete structure of energy states leads to a discrete absorption spectrum of QDs, which is in contrast to the continuous absorption spectrum of a bulk semiconductor

Here we focus on the effects of quantum confinement on the electronic structure of two prototypical semiconductors - CdSe and GaAs. Most of the studies have focused on size dependent shifts of the valence band maximum as well as the conduction band minimum. Scaling laws have been derived from experimentally determined shifts and contrasted with

[1]This section is based on the following paper:
R. Cherian, A. Kumar, and P. Mahadevan, *Effects of quantum confinement on the conduction band minimum of semiconductors* J. Nanoscience and Nanotechnology, **9**, 5673 (2009).

various theoretical calculations [13]. Unfortunately the theoretical calculations that can calculate the electronic structure over the entire size range are limited to semi-empirical approaches such as tight binding [14, 15], effective-mass, charge patching [16] or empirical pseudopotential. Each of these predict a different scaling behavior. Coupled with the experimental uncertainties of pinned Fermi levels, one is unsure of the exact trends. In this context *ab-initio* calculations would be extremely useful, although restricted to the small size regime. To date the only report of the shifts from *ab-initio* calculations appears to be from Puzder *et al.* [17], though it is not entirely clear how they align the conduction band minima from different calculations. While we report the conduction band minimum shifts from the *ab-initio* calculations, the size regime is too small to determine the scaling laws.

4.2.2 Methodology

The electronic structure of the clusters was calculated within a plane wave pseudopotential approach using the implementation in VASP. GGA PW91 approximation [12] to the exchange has been used for CdSe and GaAs and the calculations were performed at Gamma point alone. A cut off energy of 250.0 eV was used for the plane wave basis for GaAs calculations while we used 274.3 eV for CdSe. In the case of GaAs clusters the semi core $3d$ states on the Ga were treated as a part of the core (refer section 3.1). As we use a plane wave implementation of density functional theory applicable to periodic systems, we consider a periodic array of nanocrystals separated by 10 Å of vacuum. Increasing the vacuum to 20 Å changed the band gap by 2 meV. Hence 10 Å of vacuum was adequate. We construct nanocrystals by cutting a spherical fragment of a bulk crystal, which has an underlying geometry of the zinc-blende structure. We had considered passivated spherical nanocrystals having 3 to 6 layers of atoms about the center atom (n=3 to n=6 nanocrystals) as discussed in Chapter 6. All atoms were relaxed to attain the minimum energy configuration. The equilibrium volume of the relaxed structure was determined using the convex hull formed by the surface atoms. This was then mapped to a sphere and the corresponding radius determined is referred to in our subsequent discussion.

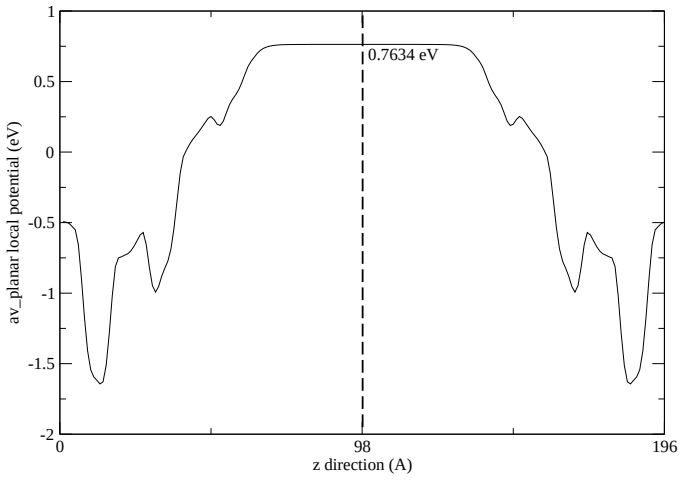

Figure 4.14: Variation of planar averaged electrostatic potential as a function of distance for the CdSe nanocrystal having a volume of 2662 $\mathring{A}^3$.

In order to determine the conduction band shifts as a function of size we need to be able to compare the conduction band minimum from different calculations. A direct comparison is not possible as the zero of the different calculations need not be the same. In this context we borrow the concepts that have been used earlier in the theoretical calculations of the band offsets. We illustrate the basic principle for the spherical cluster of CdSe which has a volume of 2662 $\mathring{A}^3$. The planar averaged electrostatic potential has been plotted as a function of distance (Fig. 4.14). This value is constant in the vacuum region of the cluster. The conduction band minima from different calculations are referred to this average electrostatic potential. For the calculation of the bulk conduction band minimum with respect to the vacuum, a symmetric slab of 11 layers was considered growing in the (001) direction. In addition a vacuum of 10 Å was included in our calculations. The surface of the slab was passivated with pseudo-hydrogens. A gamma centered k-grid of 6x6x1 was used for the calculation. We start with the optimized bond lengths of the bulk for the slabs but perform geometry optimization of the structure, restricting to the T_d point group symmetry.

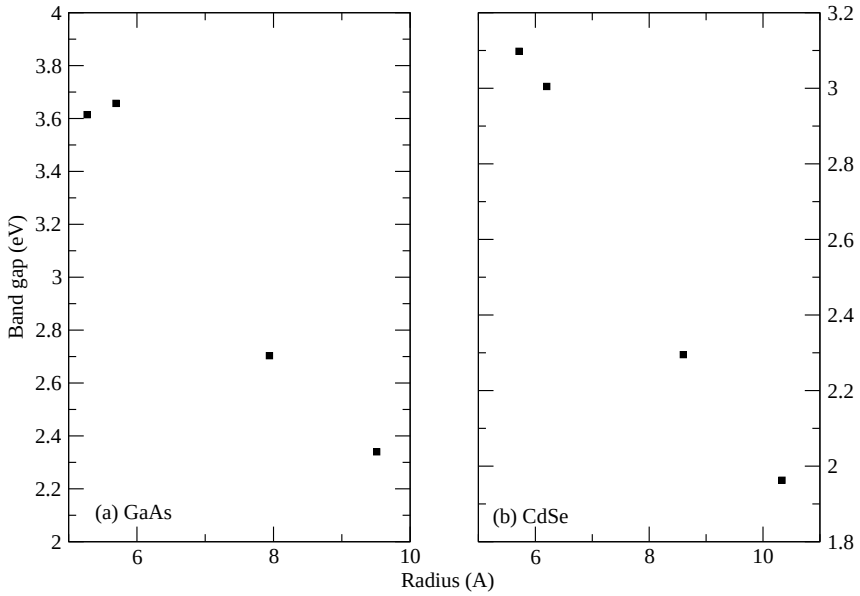

Figure 4.15: Variation of the band gap as a function of the cluster size for (a) GaAs and (b) CdSe.

4.2.3 Results and Discussion

In Fig. 4.15 we have plotted the variation of the band gap as a function of cluster size for GaAs and CdSe. An almost monotonic increase is found with decreasing cluster size. In Fig. 4.16 we have plotted the variations of the conduction band minimum in CdSe and GaAs as a function of particle size. This is of special interest as the work by Puzder *et al.* suggested a pinning of the conduction band minimum for small sizes. However, we do not find any such pinning for the systems that we have studied as well as in the size range that we have considered. For both systems we find a monotonic decrease as a function of particle size, though the changes seem significant for CdSe than for GaAs for a similar size change. Further, we find that for the largest CdSe particles considered by us in our calculations, the deviation of the conduction band minimum from bulk like values is small in contrast to other empirical approaches [14, 15, 16]. A comparison is provided in Table

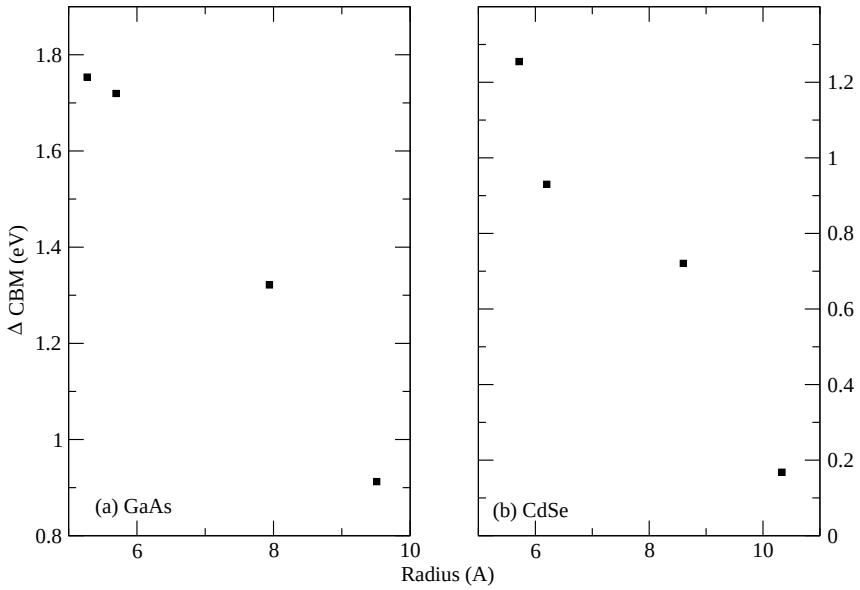

Figure 4.16: Difference of the conduction band minimum from the bulk value as a function of nanocrystals size for (a) GaAs and (b) CdSe.

4.2.

4.2.4 Conclusion

We have extracted absolute values of conduction band shifts from *ab-initio* calculations. The scheme has been applied to GaAs as well as CdSe. While a monotonic decrease of the shifts is found as a function of size, the dependence is faster in the case of CdSe and deviations from bulk-like values are quite small for the largest size considered by us.

Table 4.2: Comparison showing the deviation of the CBM (eV) for various sizes of CdSe nanocrystals from the bulk values within our present work and other empirical approaches.

Cluster size (n)	Radius (Å)	C.P Theory [16]	T.B Theory [14]	T.B Theory [15]	Present Work
3	5.7	1.6	1.3	1.8	1.25
4	6.2	1.5	1.25	1.6	0.93
5	8.6	1.2	0.9	1.4	0.72
6	10.33	1.0	0.75	1.0	0.17

Bibliography

[1] B. R. Nag, Physics of Quantum Well Devices, Kluwer Academic Publishers, (2000).

[2] M. Gratzel, Nature (London) **414**, 338 (2001).

[3] J. Lee, Y. Sung, T. Kim, and H. Choi, Appl. Phys. Lett. **91**, 113104 (2007).

[4] M. Jaros, Physics and Applications of Semiconductor Microstructures, Oxford University Press, (1990).

[5] J. Ihm, Appl. Phys. Lett. **50**, 1068 (1987).

[6] K. J. Moore, P. Dawson, and C. T. Foxon, Phys. Rev. B **38**, 3368 (1988).

[7] M. C Munoz, V. R. Velasco, and F. Garcia-Moliner, Phys. Rev. B **39**, 1786 (1989).

[8] R. Cingolani, L. Baldassarre, M. Ferrara, M. Lugara, and K. Ploog, Phys. Rev. B **40**, 6101 (1989).

[9] Hung-Sik Cho and Paul R. Prucnal, Phys. Rev. B **36**, 3237 (1987).

[10] J. G. Menchero, T. G. Dargam, and Belita Koiller, Phys. Rev. B **61**, 13021 (2000).

[11] A. Franceschetti and A. Zunger, Phys. Rev. B **52**, 14664 (1995).

[12] J. P. Perdew and Y. Wang, Phys. Rev. B **45**, 13244 (1992).

[13] T. van Buuren, L. N. Dinh, L. L. Chase, W. J. Siekhaus, and L. J. Terminello, Phys. Rev. Lett. **80**, 3803 (1998); C. Bostedt, T. van Buuren, T. M. Willey, N. Franco, L. J. Terminello, C. Heske, and T. Mller, Appl. Phys. Lett. **84**, 4056 (2004); J. R. I.

Lee, R. W. Meulenberg, K. M. Hanif, H. Mattoussi, J. E. Klepeis, L. J. Terminello, and T. Buuren, Phys. Rev. Lett. **98**, 146803 (2007).

[14] P. E. Lippens and M. Lannoo, Phys. Rev. B **41**, 6079 (1990).

[15] S. Sapra and D. D. Sarma, Phys. Rev. B **69**, 125304 (2004).

[16] L. Wang and J. Li, Phys. Rev. B **69**, 153302 (2004).

[17] A. Puzder, A. J. Williamson, F. Gygi, and G. Galli, Phys. Rev. Lett. **92**, 217401 (2004).

Chapter 5

Ferromagnetism in Mn doped dilute III-V alloys

5.1 Introduction

Dilute magnetic semiconductors have been intensively studied in recent times with the intention of replacing conventional electronic devices with those based on these materials [1]. No real devices have been realized so far and the interest in this field has been based on concept devices. An essential aspect of dilute magnetic semiconductors based devices is the manipulation of the spin of the electron which one would like to do at room temperature. Hence the search is on for a room temperature ferromagnet. One material that has been intensively studied for this purpose is Mn doped GaAs [2]. The ferromagnetic Curie temperature (T_c) are still far from desirable reaching a maximum of 250 K in specially designed superlattices [3]. Alternate materials such as transition metal atoms doped in II-VI semiconductors [4], perovskite oxides [5], other oxides [6], III-V semiconductors and chalcopyrites [7] have been synthesized and studied and the search is on for the most suitable material. In this work we confine our attention to Mn doping in III-V semiconductors. Theoretical calculations predict a higher ferromagnetic stabilization energy for Mn in GaN than in GaAs [8]. However, the main conclusion from experiments is that the effective interaction between the Mn atoms is antiferromagnetic [9] or could be weakly ferromagnetic [10]. Strong ferromagnetism has been observed though the origin seems to be the presence of ferromagnetic clusters of Mn present at large doping

[1]This chapter is based on the following paper:
R. Cherian, P. Mahadevan, and C. Persson, *Trends in Ferromagnetism in Mn doped dilute III-V alloys from a density functional perspective*, Phys. Rev. B.**79**, 195211 (2009).

concentrations [11].

In this work we examine an alternate strategy to obtaining high Curie temperatures by considering dilute alloys of III-V semiconductors. Strong valence band bowing is expected in the dilute limit in some cases, and we want to use that to modify the ferromagnetic stability. These ideas are not new to the current work and have been proposed earlier in the literature [12]. However there is no detailed theoretical work which has examined the electronic structure, modified interaction strengths and the consequent implications on the T_c. The basic idea that one aims to exploit here is to use semiconductors with band edges energetically closer to the Mn $3d$ levels. This increases the hydridization between the host anion p states and the Mn d states. This however results in a deep acceptor level in the band gap. Thus the ferromagnetism-mediating holes are more localized. A system that has been proposed as a strong candidate is a dilute alloy of GaAs with GaP. The hope is that the itinerancy of the carriers is retained while the p-d exchange is enhanced because of the shorter Mn-anion bond lengths. LDA+U/coherent potential approximation (CPA) based calculations [13] have looked at 25%, 50%, 75% alloys of GaAs and GaP and found a modest increase in T_c. Experiments [14, 15] have looked at the dilute limit of $Ga_{1-x}Mn_xAs_{1-y}P_y$ and $Ga_{1-x}Mn_xAs_{1-y}N_y$ with y $\sim$ 0.01-0.04. There is a strong decrease in T_c with increasing y even at this dilute limit. As the dilute limit has not been studied theoretically we examine whether the experimental trends may be captured within our calculations and if not, then the cause is due to extraneous factors not included in the present approach. We are able to capture the reduction of T_c in GaAs alloyed with GaN as well as the case of GaAs alloyed with GaP.

5.2 Methodology

In order to address these issues we have considered 216 atom supercells of GaAs, GaP and GaN. One Mn was placed at the origin while the second was placed at the fourth FCC neighbor position as earlier work has shown that the ferromagnetic stability is strongest for Mn atoms at these positions [16]. We consider dilute III-V alloys as the host semiconductor into which Mn is doped. In order to form the dilute III-V alloys a group V anion impurity is codoped at different distances on the line perpendicular to the line joining

the two Mn sites. For GaAs alloyed with GaP we included higher dopant concentrations also. The optimized lattice constants for the GaAs, GaP and GaN are 5.72, 5.49 and 4.52 Å respectively. The lattice constant of the supercell is set according to Vegard's law for the III-V alloy. Full optimization of the internal positions is carried out within the first principle electronic structure calculations using a plane wave pseudopotential implementation of the density functional theory. A plane wave cutoff of 400 eV was used for the basis set. The electronic structure was solved considering the generalized gradient approximation for the exchange at Gamma point alone using projected augmented wave (PAW) potentials [17].

5.3 Results and Discussion

We first consider the case of the As doped into GaN. GaN we know has a large band offset with GaAs with the former having a deeper valence band maximum. Mn when doped into GaN has been shown to introduce states into the band gap with significant Mn character. However, in contrast, Mn when doped into GaAs is found to introduce states with weak Mn character in the band gap. Although in both cases the formal oxidation state of the Mn is 3+, in the former case the configuration is d^4 while in the latter case is $\{d^5+$ hole$\}$[18]. Since at this dilute limit, alloys show significant band bowing effects, we investigate Mn doping in this limit to probe modifications in the ferromagnetic stability. In Fig. 5.1 we have plotted the Mn d partial density of states. The N p partial density of states of a N atom which is nearest neighbor of the Mn as well the As p partial density of states have been shown. The valence band maximum seems to comprise of primarily As p states with some N p admixture. However there is hardly any As p character at the Fermi level. We can understand this effect within a simple model that was proposed earlier to explain the electronic structure of transition-metal (TM) impurities in semiconductors [18]. The dominant interaction seems to be between the transition-metal impurity and its nearest neighbors. Atoms farther away from the TM impurity interact to a much lesser extent.

The next question we ask was how is the ferromagnetic stability modified. Should the presence of the As impurity affect the ferromagnetic stability? As the As levels are

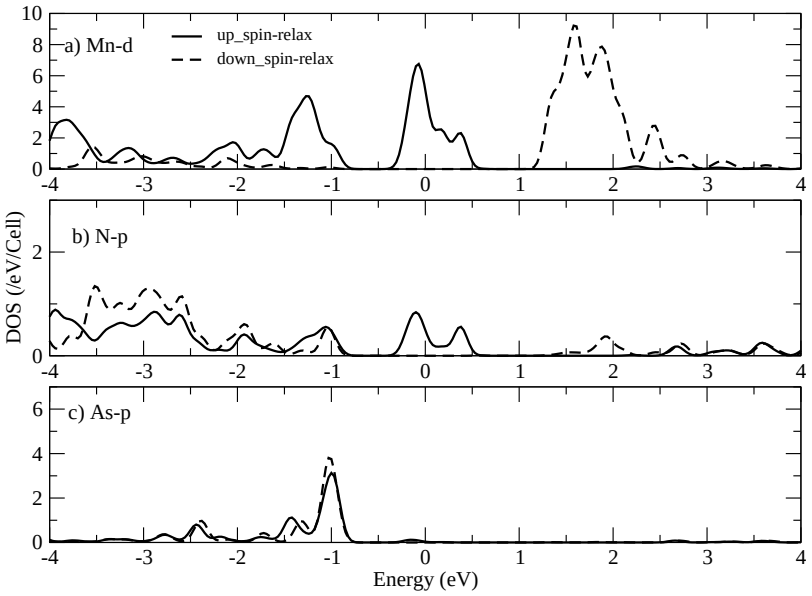

Figure 5.1: (a) The up (solid line) and down (dashed line) spin projected density of states for Mn d, (b) N p, which is the nearest neighbor of the Mn, and (c) for the As p calculated for (Ga,Mn)N codoped with As. The zero of energy corresponds to the Fermi energy.

Table 5.1: Effect on the stability by As codoping in (Ga,Mn)N host. The distance of the As atom from either Mn atoms in both the ferromagnetic (FM) and antiferromagnetic (AFM) relaxed configuration is also given.

Distance (Å)		Ferromagnetic stability (meV)	T_c (K)
FM	AFM	$(E_{FM} - E_{AFM})$	
-	-	-83.8	324.2
3.72	3.71	-20.6	79.6
5.89	5.86	-50.0	193.4
6.71	6.69	-50.0	193.4
8.11	8.10	-34.8	134.6

between the Mn d and the N p levels one would expect a modification in the ferromagnetic stability, possibly a value between the two end limits of Mn in GaN and GaAs. In this dilute alloy limit the valence band maximum is intermediate between that for GaAs and GaN. The ferromagnetic stability as well as the corresponding mean field estimate of T_c are given in Table 5.1 for various distances of the As impurity from either Mn atom. In the absence of As impurity, the ferromagnetic stability is ~ 84 meV and at the other limit of Mn in GaAs it is ~ 164 meV. This drastically drops to ~ 21 meV in the presence of an As impurity at 3.76 Å. As the As impurity is moved farther away the ferromagnetic stability is partly regained though it still remains less than the value in the absence of As impurity. This is contrary to our expectations and indicates that one must consider other factors such as alloy scattering in addition to the modified energy denominator for the interaction.

Examining the opposite limit of GaAs into which the N is doped we find a similar trend in the ferromagnetic stabilization energy. In GaAs, Mn doping gives rise to a ferromagnetic stabilization energy of 164 meV (Table 5.2). This drastically drops to 100 meV (Table 5.2) for a N impurity introduced at 4.73 Å. Ferromagnetic stability corresponding to the unalloyed limit is partially regained for the N atoms farther away from Mn as shown in Table 5.2.

Recent experimental work [14] on dilute magnetic semiconductors have focussed on

Table 5.2: Effect on the stability by N codoping in (Ga,Mn)As host. The distance of the N atom from either Mn atoms in both the ferromagnetic (FM) and antiferromagnetic (AFM) relaxed configuration is also given.

Distance (Å)		Ferromagnetic stability (meV)	T_c (K)
FM	AFM	$(E_{FM} - E_{AFM})$	
-	-	-163.8	633.6
4.73	4.75	-100.1	387.2
7.41	7.42	-154.3	596.9
8.44	8.44	-161.7	625.5
10.18	10.19	-147.5	570.6

transition metal impurities in dilute alloys with an aim of understanding the mechanism of the ferromagnetism better. If the hole introduced by Mn doping is a valence band hole the belief is that it should be weakly perturbed by alloying effects at the dilute limit. However a hole which resides in an impurity band is expected to be strongly affected by alloying effects. We artificially tune the hole introduced by the Mn doping with a introduction of U on the Mn d states in $(Ga, Mn)As_{0.99}N_{0.01}$. With a U of 4 eV on the Mn d states, the hole moves towards a valence band hole. Hence alloy scattering effects are expected to be weaker. Indeed our calculated ferromagnetic stability results effect this. In the absence of any N impurity we see that the FM stability decreases when we apply a U on the Mn-d states, which is expected. Analyzing the Mn-d up character near the Fermi energy (+/- 0.5 eV) (Fig. 5.2) we see that for the U=0 case we see $\sim$ 11 % contribution of the total Mn-d up character while in the presence of U on the Mn-d states we see a very less contribution of Mn-d up states near to the Fermi energy (here its $\sim$ 2% of the total Mn-d up character). So with a U on the Mn d states, the Mn character at the Fermi level decreases. Thus the impurity band introduced by the Mn doping becomes more delocalized and hence faces reduced alloy scattering effects on the T_c (Table 5.3). The ferromagnetic (FM) stability results reflect this. The FM stability changes by about 64 meV in the absence of U to 15 meV in the presence of U. Stone *et al.* [14] have examined P doping in GaMnAs. An insulator to metal transition is observed as a function of doping. Usually high effective mass have to be assumed for the carriers

Table 5.3: Effect on the stability by N codoping in (Ga,Mn)As host. The distance of the N atom from either Mn atoms in both the ferromagnetic (FM) and antiferromagnetic (AFM) relaxed configuration is also given.

U (eV) on Mn-d states	Distance (Å)		Ferromagnetic stability (meV)	T_c (K)
	FM	AFM	$(E_{FM} - E_{AFM})$	
0	-	-	-163.8	633.6
4	-	-	-128.1	495.5
0	4.73	4.75	-100.1	387.2
4	4.75	4.76	-113.6	439.4

to explain the experimental observations. This reinforces the idea of the carriers residing in an impurity band.

While Mn in GaN has usually been accepted as a system in which the hole introduced by Mn doping resides in an impurity band, the case of Mn in GaAs is heavily debated with supporters on both sides. In order to quantify our observations further we examined Mn doping in dilute alloys formed by P introduction in GaAs. If our earlier results of the N doping in GaAs established the validity of the impurity band model, then we should see strong effects on the ferromagnetic stability here also. The results as a function of the impurity distance are given in Table 5.4. The perturbation seems to be very weak and consequently the variations in the ferromagnetic stabilization energy from the unperturbed case are small. Hence modifications of ferromagnetic stability in alloyed systems is not proof enough for the impurity band picture. The deviation between our results and experimental results of $GaMnAs_{1-y}P_y$ could be due to various reasons. One cause could be that the alloying concentration are large. Indeed when we introduced two P impurities, such that each P atom is the nearest neighbor to one of the Mn atom and also these P atoms connects the Mn atoms via a Ga atom, we found a reduction in the ferromagentic stability from 164 meV in the unalloyed limit to 110 meV. Thus impurity scattering is responsible for the reduction in ferromagnetic stability.

Closer analysis revealed that there are two parts which need to be considered when an impurity atom is introduced. The first part is that associated with the modified

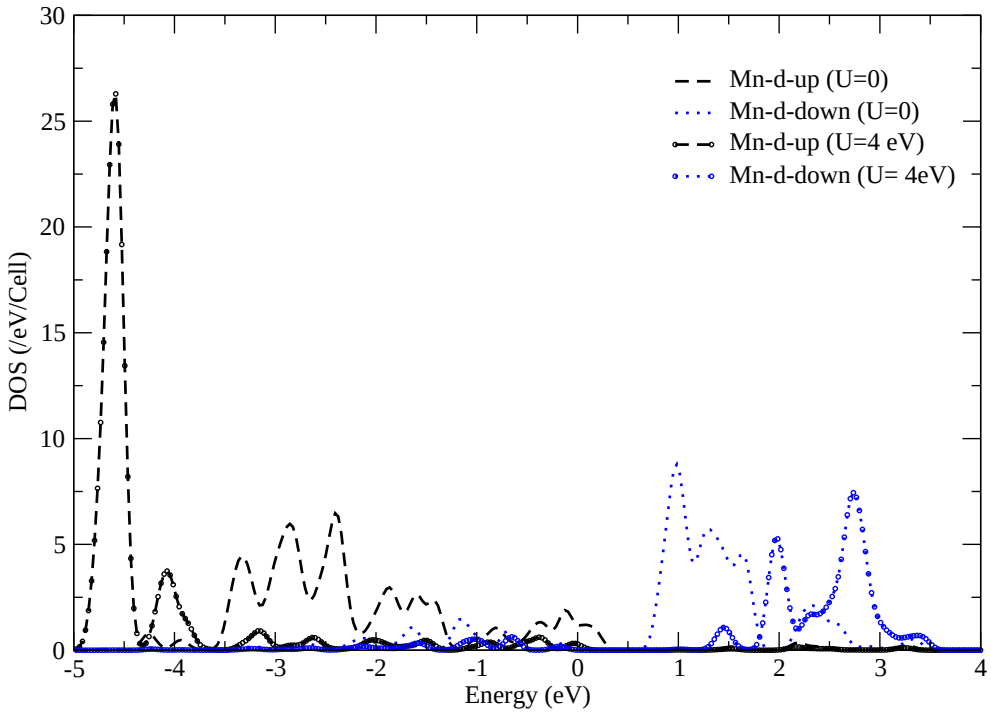

Figure 5.2: The spin up (dashed lines) and down (dotted lines) projected density of states for Mn *d* calculated for (Ga,Mn)As case in the absence (no symbols) and presence (open circles) of a U on the Mn-d states. The zero of energy corresponds to the Fermi energy.

Table 5.4: Effect on the stability by P codoping in (Ga,Mn)As host. The distance of the P atom from either Mn atoms in both the ferromagnetic (FM) and antiferromagnetic (AFM) relaxed configuration is also given.

Distance (Å)		Ferromagnetic stability (meV)	T_c (K)
FM	AFM	$(E_{FM} - E_{AFM})$	
-	-	-163.8	633.6
4.73	4.75	-154.3	596.9
7.42	7.44	-162.1	627.0
8.45	8.45	-169.1	654.1
10.21	10.21	-172.7	668.0

Table 5.5: Effects of relaxation on the stability in the case of (Ga,Mn)As host codoped with N.

	Energy (eV)		Ferromagnetic stability (meV)	T_c (K)
	E_{FM}	E_{AFM}	$(E_{FM} - E_{AFM})$	
Un-Relaxed	-907.192	-906.989	-203.2	786.0
Relaxed	-909.264	909.164	-100.1	387.2

electronic interaction strengths associated with the impurity and the second associated with the strain in the host lattice. Indeed we cannot decouple the two effects completely but the effects of these perturbations may be discussed within calculations performed under some constraints.

In Table 5.5 we consider the case of N codoped into GaAs at a distance of 4.73 Å. The ferromagnetic stability is evaluated in the unrelaxed case where the calculation is performed assuming that N merely replaces an As atom.

This calculation would capture the effects of modified interaction strengths as a result of N doping. Ferromagnetic stability of the Mn pairs is increased from 164 meV in the absence of N impurity to 203 meV. Examining the density of states corresponding to the unrelaxed limit, we find that N p states are energetically closer to the Mn d states and hence the increased interaction between the two could explain the increased ferromagnetic

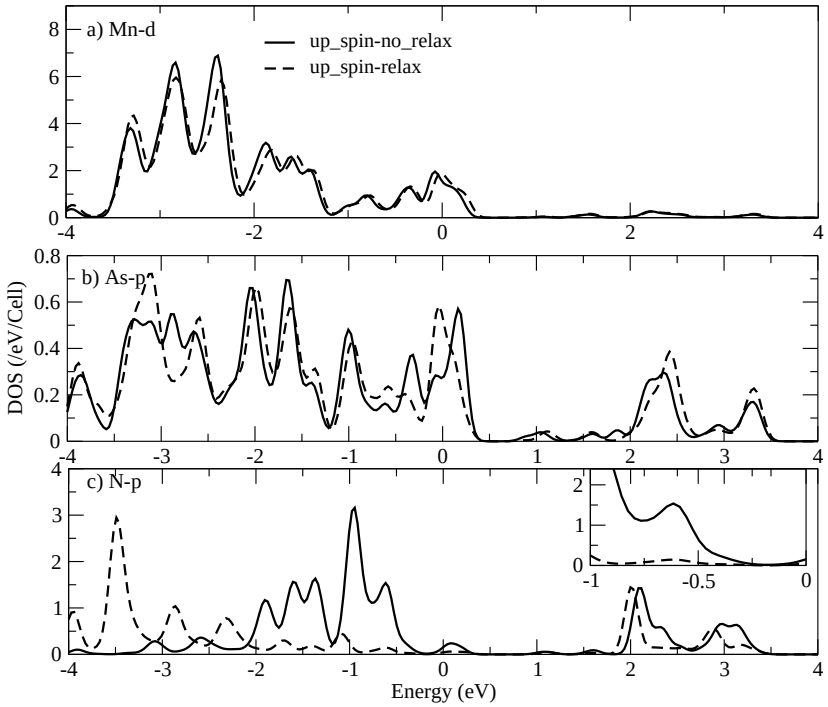

Figure 5.3: (a) The spin up projected density of states for Mn d, (b) As p, which is the nearest neighbor of the Mn, and (c) for the N p calculated for (Ga,Mn)As codoped with N. Inset of (c) shows a magnified view of the N p density of states near the Fermi energy region. The solid lines corresponds to the unrelaxed case while the dashed lines corresponds to the relaxed case. The zero of energy corresponds to the Fermi energy.

stability.

This is reflected in the inset of Fig. 5.3(c) which shows the N p character near Fermi energy. Ga-N bonds are much smaller than the Ga-As bonds. Allowing the atoms to optimize their internal positions by total energy minimization We find that the Ga-N bonds are ~ 2.08 Å long while the Ga-As bonds close to the N atom are 2.53 Å long. Those far away from the N impurity are 2.48 Å long. Examining the ferromagnetic stability in such a configuration, we find that it is drastically reduced to 100 meV. Examining the density of states (Fig. 5.3) we find that there is hardly any change in the As p density of states plotted for the nearest neighbor As atom as well as the Mn d partial density of

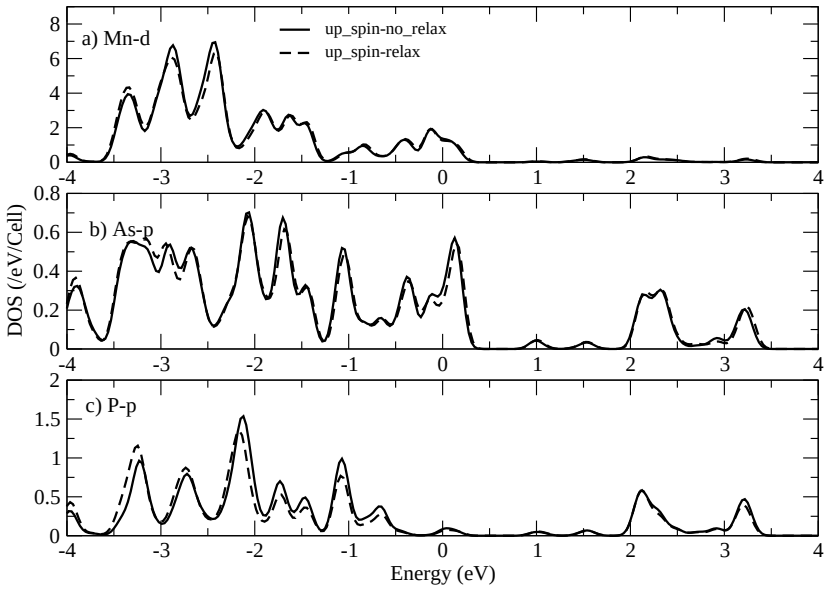

Figure 5.4: (a) The spin up projected density of states for Mn d, (b) As p, which is the nearest neighbor of the Mn, and (c) for the P p calculated for (Ga,Mn)As codoped with P. The solid lines corresponds to the unrelaxed case while the dashed lines corresponds to the relaxed case. The zero of energy corresponds to the Fermi energy.

states with and without relaxation. N p density of states show significant changes with relaxation with the N p states moving from -1 eV to -3.5 eV below the Fermi level. In the inset of Fig. 5.3(c) we magnify the near Fermi energy region of the N p density of states and see that there is significant N p character at the Fermi energy in the unrelaxed case which is reduced upon relaxation. Since movement of N p levels should imply reduced interaction with Mn, the main effect of ferromagnetic stability reduction has to be the lattice strain.

Considering the case of P in GaAs doped with Mn (Fig. 5.4), we find that the effects of relaxation are very weak as a result of which ferromagnetic stability is hardly affected (Table 5.4). Thus we are able to elucidate the microscopic origin of the reduction of T_c when

we alloy III-V semiconductors with another group V anion. Although our calculations provide us with qualitative trends, an exact numerical expression for the T_c as a function of concentration in the dilute limit is difficult. This is because the ferromagnetic stability is a strong function of the disorder position as well as of concentration. Strong disorder potentials caused by clustering of the alloying atoms results in a stronger decrease in T_c than when one has a random distribution.

5.4 Conclusion

We have examined Mn doping in the dilute alloy limit where strong valence band bowing is observed, as a possible route to enhance the ferromagnetic transition temperature. This has been quantified in our calculation as the ferromagnetic stabilization energy for a pair of Mn atoms occupying lattice sites for which ferromagnetic stability has been observed to be strong. Contrary to expectations of enhanced ferromagnetic stability on alloying we find a reduction in the case of $Ga_{1-x}Mn_xAs_{1-y}N_y$ and $Ga_{1-x}Mn_xAs_{1-y}P_y$ where y ~ 0.01. Mn doping in $Ga_{1-x}Mn_xAs_{1-y}P_y$ shows very small changes in the ferromagnetic stability for 1% anion doping but for larger percentage of doping shows a reduction in T_c. The origin of reduced ferromagnetic stability is traced to the strong strain effects that accompany the introduction of the anion impurity. This strongly scatters the electron comprising the valence band maximum and therefore modifies the ferromagnetic stability.

Bibliography

[1] T. Jungwirth, J. Sinova, J. Masek, J. Cora, and A. H. MacDonald, Rev. Mod. Phys. **78**, 809 (2006).

[2] K. M. Yu, W. Walukiewicz, T. Wojtowicz, I. Kuryliszyn, X. Liu, Y. Sasaki, and J. K. Furdyna, Phys. Rev. B **65**, 201303 (2002). M. J. Seong, S. H. Chun, H. M. Cheong, N. Samarth, and A. Mascarenhas, Phys. Rev. B **66**, 033202 (2002).

[3] A. M. Nazmul, T. Amemiya, Y. Shuto, S. Sugahara, and M. Tanaka, Phys. Rev. Lett. **95**, 017201 (2005).

[4] H. Saito, V. Zayets, S. Yamagata, and K. Ando, Phys. Rev. Lett. **90**, 207202 (2003).

[5] S. Ray, P. Mahadevan, S. Mandal, S. R. Krishnakumar, C. S. Kuroda, T. Sasaki, T.Taniyama, and M. Itoh, Phys. Rev. B **77**, 104416 (2008).

[6] S. B. Ogale, R. J. Choudhary, J. P. Buban, S. E. Lofland, S. R. Shinde, S. N. Kale, V. N. Kulkarni, J. Higgins, C. Lanci, J. R. Simpson, N. D. Browning, S. Das Sarma, H. D. Drew, R. L. Greene and T. Venkatesan, Phys. Rev. Lett. **91**, 077205 (2003); J. Philip, A. Punnoose, B. I. Kim, K. M. Reddy, S. Layne, J. O. Holmes, B. Satpati, P. R. Leclair, T. S. Santos, and J. S. Moodera, Nat. Mater. **5**, 298 (2006).

[7] G. A. Medvedkin, T. Ishibashi, T. Nishi, K. Hayata, Y Hasegawa, and K. Sato, Jpn. J. Appl. Phys. **39**, L949 (2000); K. Sato, G. A. Medvedkin, T. Nishi, Y. Hasegawa, R. Misawa, K. Hirose, and T. Ishibashi, J. Appl. Phys. **89**, 7027 (2001).

[8] P. Mahadevan and A. Zunger, Appl. Phys. Lett. **85**, 2860 (2004).

[9] S. Dhar, O. Brandt, A. Trampert, L. Daweitz, K. J. Friedland, K. H. Ploog, J. Keller, B. Beschoten, and G. Guntherodt, Appl. Phys. Lett. **82**, 2077 (2003).

[10] E. Sarigiannidou, F. Wilhelm, E. Monroy, R. M. Galera, E. Bellet-Amalric, A. Rogalev, J. Goulon, J. Cibert, and H. Mariette, Phys. Rev. B **74**, 041306(R) (2006).

[11] S. Dhar, O. Brandt, A. Trampert, K. J. Friedland, and K. H. Ploog, Phys. Rev. B **67**, 165205 (2003).

[12] A. H. MacDonald, P Schiffer, and N Samarth, Nature Mater. **4**, 195 (2005).

[13] J. Masek, J. Kudrnovsky, F. Mca, Jairo Sinova, A. H. MacDonald, R. P. Campion, B. L. Gallagher, and T. Jungwirth, Phys. Rev. B. **75**, 045202 (2007).

[14] P. R. Stone, K. Alberi, S. K. Z. Tardif, J. W. Beeman, K. M. Yu, W. Walukiewicz, and O. D. Dubon, Phys. Rev. Lett. **101**, 087203 (2008).

[15] K. Alberi, K. M. Yu, P. R. Stone, O. D. Dubon, W. Walukiewicz, T. Wojtowicz, X. Liu, and J. K. Furdyna , Phys. Rev. B. **78**, 075201 (2008).

[16] P. Mahadevan, A. Zunger, and D. D. Sarma, Phys. Rev. Lett. **93**, 177201 (2004).

[17] P. E. Blöchl, Phys. Rev. B. **50**, 17953 (1994); G. Kresse and J. Joubert, Phys. Rev. B **59**, 1758 (1999).

[18] P. Mahadevan and A. Zunger, Phys. Rev. B **69**, 115211 (2004).

Chapter 6

Semiconductor nanocrystals

In this chapter we study the variation of the lattice constant and bulk modulus of semiconductor nanocrystals as a function of size. We also examined the strain profile of the bond-lengths in these nanocrystals in their optimized geometries as a function of size and studied the role of different geometries in modifying their equilibrium lattice constant.

Group IV elements, silicon (Si) and germanium (Ge), (which occur in the diamond structure), as well as a group III-V compound, gallium-arsenide (GaAs), and a II-VI compound, cadmium-selenide (CdSe), are considered in this study. The latter two occur in the zinc-blende structure. For certain studies CdSe nanocrystals were also considered in the wurtzite structure [1].

6.1 Methodology

The electronic structure of the crystals were calculated within a plane wave pseudopotential approach using the implementation in VASP. The calculations were performed at Gamma point alone. Unless it is specified specifically, the LDA approximation for the exchange has been used. A cutoff energy of 250.0 eV was used for the plane wave basis for Si, Ge and GaAs calculations while a value of 274.3 eV was used for CdSe.

In our studies, nanocrystal were constructed by considering a central atom and adding the next shell of atoms preserving the tetrahedral coordination that exists in the bulk [2]. The crystals were truncated by either of two schemes. The first (layered) in which

Table 6.1: Atom 'A' centered binary nanocrystals (AB) considered with an underlying zinc-blende or wurtzite geometry. N_A and N_B are the number of 'A' and B type of atoms in each nanocrystals generated by layered and spherical prescriptions.

Nanocrystal	Nanocrystal size (n)	N_A	N_B
Zinc-blende	5	55	92
(Layered)	4	55	28
	3	13	28
	2	13	4
	1	1	4
Zinc-blende	6	79	68
(Spherical)	5	43	44
	4	19	16
	3	13	16
Wurtzite	6	69	74
(Spherical)	5	51	41
	4	19	20
	3	13	14

each subsequent layer is added preserving the tetrahedral bonding of the inner layer. This leads to the scenario where one has atoms of only one type at the surface. In the case of the binary nanocrystal this leads to highly non-stoichiometric nanocrystals. The other method (spherical) of termination involves choosing a central atom and considering only those atoms which lie within a pre-defined cutoff radius [3]. It is believed to be valid for large nanocrystal sizes as various experiments have found bulk-like coordination [4]. The number of A-type (N_A) and B-type (N_B) of atoms for a 'A' centered 'AB' layered and spherical nanocrystals considered by us are given in Table 6.1.

All atoms at the surface would have broken coordination, while the interior would have bulk-like coordination. These nanocrystals will be termed as unpassivated nanocrystals. Consequently, bonds would be shorter at the surface and longer inside. To limit these perturbations, and to be in agreement with experiment (where the samples are usually passivated) the surface atoms of the nanocrystal are then passivated with hydrogen in the case of Si and Ge and with pseudo-hydrogen [5] in the case of binary nanocrystals.

These nanocrystals are termed as passivated nanocrystals. All atoms of the nanocrystal were then relaxed, with the symmetry restricted to T_d point group symmetry, to attain the minimum energy configuration. As we use an implementation of density functional theory which works for periodic cells, a periodic array of nanocrystals with separations consisting of 8 to 10 Å (refer section 6.4.2) of vacuum was considered by us. Finally, in the case of GaAs nanocrystals, the semi core $3d$ states on the Ga atom were treated as a part of the core (refer section 3.1). A passivated layered and spherical nanocrystal centered on one atom and having 3 layers of atoms about the central atom is show in Fig. 6.1 and Fig. 6.2 respectively, and this is given the name n=3 layered and n=3 spherical passivated nanocrystals.

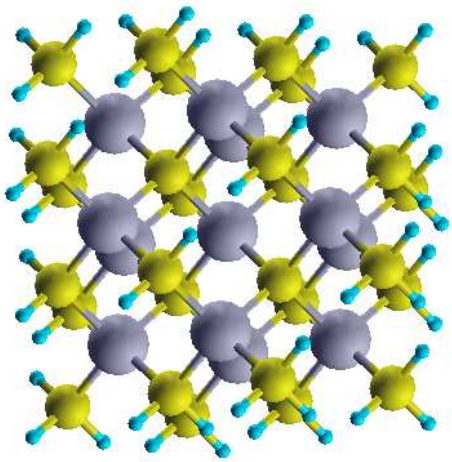

Figure 6.1: A ball and stick model for layered 'A' centered passivated 'AB' nanocrystals (n=3) having an underlying zinc-blende geometry. The large balls correspond to 'A' atoms, the medium sized balls correspond to 'B' atoms and the outer smaller balls denote the pseudo-hydrogen atoms.

Unless it is specified specifically all atoms of the nanocrystal were then relaxed to

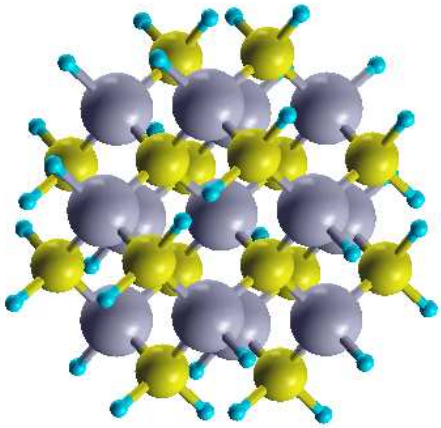

Figure 6.2: A ball and stick model for spherical 'A' centered passivated 'AB' nanocrystals (n=3) having an underlying zinc-blende geometry. The large balls correspond to 'A' atoms, the medium sized balls correspond to 'B' atoms and the outer smaller balls denote the pseudo-hydrogen atoms.

attain the minimum energy configuration. We also test the energy convergence of the nanocrystals for different starting configuration of the nanocrystals. Here for the studies we considered passivated n=4 and n=5 spherical Ga centered GaAs nanocrystals where they were formed by the bulk like fragment having different lattice constants (Table 6.2). We find that all the different starting configuration of the nanocrystal leads to the same minimum energy configuration as well as same averaged equilibrium lattice constant. The details of how the averaged equilibrium lattice constant of the nanocrystals are calculated will become more clear in the section 6.2. The error bar in our calculated average lattice constant is about 0.005 Å.

From the final relaxed optimized structure the nanocrystal was expanded and contracted keeping the geometry fixed and at each size the convex hull formed by the surface

Table 6.2: Variation of the optimized energy and average equilibrium lattice constant variation for different starting configuration of passivated spherical Ga centered GaAs nanocrystal.

	Starting lattice constant (Å)	Final optimized configuration	
		Energy (eV)	Averaged equilibrium lattice constant (Å)
n=4			
	5.65	-253.6672	5.692
	5.75	-253.6670	5.693
	5.80	-253.6675	5.692
n=5			
	5.65	-588.7179	5.711
	5.74	-588.7173	5.713
	5.80	-588.7174	5.714

atoms was constructed and it was used to compute the volume. During the expansion and the contraction of the final optimized structure of a particular sized nanocrystal the supercell was fixed at the same size so that we have the same number of plane wave in all the calculations. The bulk modulus were then calculated by fitting the energy variation with volume to the Murnaghan equation of state [6].

6.2 Size dependence of lattice constants of semiconductor nanocrystals

6.2.1 Introduction

The properties of semiconductor nanocrystals have received a lot of attention in the past two decades as a result of strong size dependence of various physical properties. The underlying crystal structure plays an important role in determining the electronic structure

[1]This section is based on the following paper:
R. Cherian and P. Mahadevan, *Size dependence of lattice constants of semiconductor nanocrystals* Appl. Phys. Lett. **92**, 043130 (2008).

and the ensuing physical properties. However the basic issue of structure determination is difficult in the context of materials at the nanoscale. Even the most powerful techniques that one is familiar with for the characterization of bulk crystals are found to fail in the case of nanocrystals [7]. The difficulties arise because in the present case one does not have a homogeneous distribution of particles. Not only do the sizes vary over several percent depending on the synthesis procedure, one also finds different shaped particles as a result of the growth techniques. Further most of the commonly used techniques provide an averaged lattice constant / bond-length. Hence several of the basic questions in the context of nanoparticles remain unanswered. It is here that theoretical calculations play an important role. They can simulate the ideal situation and hence can be used to provide insight into the modifications in the lattice constant that take place as a function of nanoparticle size.

Nanocrystals consist of a size-able number of atoms on the surface. In an ideal situation, all atoms at the surface would have broken coordination, while the rest would have bulk-like coordination. To make up for the lost coordination, stress develops at the surface and decays into the bulk. Naively as a result of this one would have longer / bulk-like bonds in the interior and shorter bonds at the surface. The naive picture would be modified as the surface atoms are usually passivated by ligands and so the strain effects are not as strong as one would expect in the unpassivated case.

The experimental literature has conflicting reports of bulk-like nearest-neighbor bond-lengths [8], small-intermediate strains resulting in modified lattice constants for the nanocrystals [9] as compared with the bulk. However, the issue of the development and variation of strain is difficult to obtain experimentally. In this context theoretical models will be able to address the issue, as well as ascertain the role of the passivants.

6.2.2 Results and Discussion

Initially the equilibrium bond-length is determined by minimizing the energy with respect to the lattice constant allowing for a uniform expansion or contraction of the volume. The equilibrium lattice constant was determined by fitting the energy as a function of volume to the Murnaghan equation of state [6]. Then the nanocrystals were passivated and all

atoms of the nanocrystals were relaxed to attain the minimum energy configuration. An average bond-length was determined by averaging over all the nearest-neighbor bond-lengths. This was then used to determine an average equilibrium lattice constant. While generating the nanocrystals we can start with either an anion or a cation at the center. In the present case we have considered both schemes of generation of the binary nanocrystals. As the conclusions arrived at were similar in both cases here we present the results for only one case in detail.

We find it useful to use the definition of Masadeh *et al.* [9] to define the surface strain. The surface strain generated in the nanocrystals is defined as

$$Bondstrain(\%) = \frac{(r_0 - r)}{r_0} \tag{6.1}$$

where 'r_0', is the nearest neighbor bond-length between the atoms, is calculated using the theoretical equilibrium lattice constant for the bulk. 'r' is the nearest neighbor bond-length that one obtains after the optimization of the structure described earlier. It should be noted that "r" varies from shell to shell of the nanocrystal, and could be different even for atoms of the same type in a given shell. This arises because of the differences in surface coordination that one can have because of the truncation scheme considered. Inspite of these variations, the qualitative aspects are similar.

We consider the case of an elemental semiconductor, Si. The calculated equilibrium lattice constants are shown in Table 6.3 as a function of nanocrystal size. One finds that the equilibrium lattice constant is 5.407 Å for the bulk. The lattice constant computed for the nanocrystals is smaller than the bulk in all the cases, as expected from the naive considerations presented earlier. A strong size dependence of the lattice constant is found in the unpassivated case which shows deviations ranging from 2.27 % to 1.02 % when we go from smaller nanocrystals with 3 layers around the central layer to larger nanocrystals with 6 layers around the central layer. However the size dependence of the lattice constant is much smaller for the passivated nanocrystals, with deviations $\sim$ 0.3% - 0.4% and approaches bulk-like values for very small nanocrystal sizes. Similar conclusions are arrived at for nanocrystals of CdSe and GaAs (refer section 6.3.2 for the passivated and Table 7.2 for the unpassivated cases). For the binary nanocrystals GGA PW91 [10] approximation for the exchange has been used.

Table 6.3: Comparison of the equilibrium lattice constant and average bond strain for the unpassivated Si nanocrystals with the average equilibrium lattice constant and average bond strain for the passivated Si nanocrystals as a function of nanocrystal size.

Nanocrystal size (n)	Diameter (Å)	lattice constant (Å)		average bond strain (%)	
		unpassivated	passivated	unpassivated	passivated
∞	∞	5.407	-	0.0	-
6	17.10	5.352	5.392	1.02	0.28
5	14.05	5.345	5.384	1.15	0.43
4	10.81	5.323	5.379	1.55	0.52
3	8.97	5.284	5.384	2.27	0.43

Inspite of the fact that the bulk lattice constant is reached quickly in the passivated case, we do find deviation in the bond-lengths as a function of depth from the surface, being maximum at the surface. Quantifying this in terms of the bond strain (Fig. 6.3(a)), we find that in the core of the nanocrystal, for the size considered we find ~ 0 % bond strain. Beyond the second layer, the strain exhibits a linear variation. Since we have a single parameter that changes i.e. depth, we would expect a linear variation with depth. This is however not the case, and we find that the strain is invariant between the third and the sixth layers. However between the first and third layers one has a linear variation with depth, with the core showing almost bulk-like lattice constants. The unusual strain profile that we find here is probably a result of a competition between the microscopic considerations determining the strain profile in the interior being different from those determining it at the surface. Hence the bond strain profile depends on the strength of the surface passivant. Consequently, the strain profile is different in the case of GaAs (Fig. 6.3(b)) and CdSe (Fig. 6.3(c)).

In the case of CdSe we considered both the zinc-blende as well as the wurtzite polymorphs. As in the zinc-blende case, the average lattice constant is almost bulk-like for nanocrystals larger than 15 Å diameter. The equatorial and the axial bonds (Fig. 6.3(d)) show almost similar depth dependences. The averaged bond-length for each layer follows a depth profile very close to one's naive expectations being constant upto the third

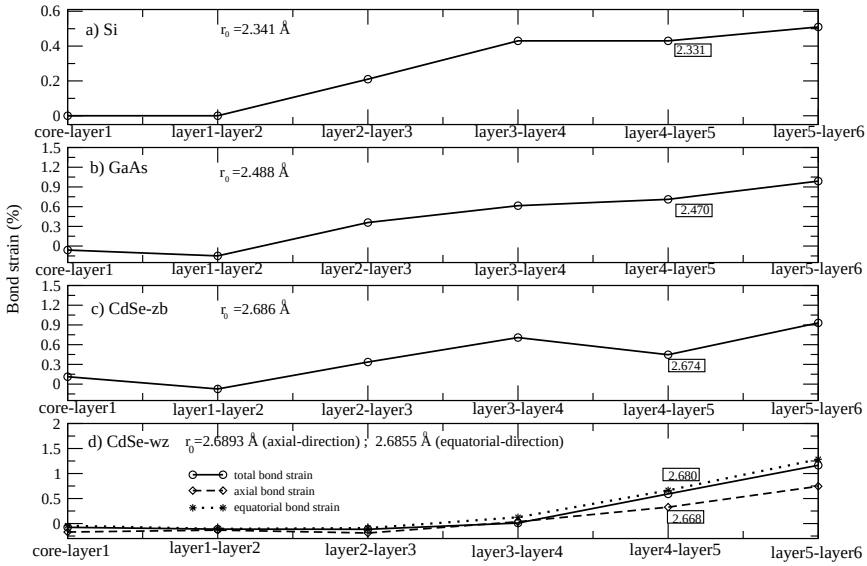

Figure 6.3: Calculated bond strain variation between indicated layers (x-axis) for n=6 (a) Si, (b) Ga-centered GaAs, (c) Cd-centered zinc-blende CdSe and (d) Cd-centered wurtzite CdSe nanocrystals. The corresponding nearest neighbor bond-length between the atoms at the theoretically obtained equilibrium bulk lattice constant for each case is given by r_0. In the case of wurtzite nanocrystals the axial (dashed line), equatorial (dotted line) as well as the average bond strain (black solid line) for each layer have been shown as a function of depth. The values of the bond-length for some layers have been indicated. A positive strain corresponds to compression of bonds by definition.

monolayer and then showing a linear variation with depth.

6.2.3 Conclusion

We have examined the deviation from bulk-like lattice constants considering nanocrystals of Si, GaAs and CdSe. Unpassivated nanocrystals shows larger deviation in the average bond-length values from the bulk-like bond-length values. Naive arguments based on broken coordination at the surface lead us to expect shorter bonds at the surface of the nanocrystal. Indeed this is found to be the case, though the surface stress generated is found to be typically $\sim 1\%$ or less when we consider nanocrystals passivated by hydrogen or pseudo-hydrogens, with almost bulk-like bond-lengths obtained 5-6 layers below the surface. Averaging over all the bond-lengths of the passivated nanocrystal we find that bulk-like bond-lengths are obtained for small nanocrystal sizes having diameter ~ 20 Å.

6.3 Effects of non-stoichiometry on the lattice constant of semiconductor nanocrystals: CdSe and GaAs

6.3.1 Introduction

Determining the structure of nanocrystals is extremely important in order to be able to quantitatively describe the properties of these materials, and derive structure-property relationships. An accurate determination of the structure, however, is limited [7] firstly by the fact that the samples have an inhomogeneous size distribution and secondly because they involve a multi-parameter fitting which depends on the suitability of the starting set. Additional problems in experiments arise from the presence of defects, nature of surface termination etc. In view of these experimental constraints, theory can play an important role in structure prediction as the ideal defect-free situation can be simulated in the calculations. In this work we have considered nanocrystals of both binary semiconductors

[2]This section is based on the following paper:
R. Cherian and P. Mahadevan, *Effects of non-stoichiometry on the lattice constant of semiconductor nanocrystals: CdSe and GaAs* J. Nanoscience and Nanotechnology, **9**, 5564 (2009).

CdSe and GaAs and examined the role of surface termination in determining the equilibrium lattice constant. The results for elemental semiconductor Si have been provided for comparison. Our results suggest that different ways of constructing the nanocrystal could lead to different equilibrium lattice constants for similar sized nanocrystals.

6.3.2 Results and Discussion

The variation of the average equilibrium lattice constants for passivated layered as well as spherical nanocrystals of Si, GaAs and CdSe as a function of nanocrystal size are plotted in Fig. 6.4. The average equilibrium lattice constants for these nanocrystals were calculated as described in section 6.2. The calculated bulk lattice constant (denoted as a_0 in Fig. 6.4) is found to be 5.407, 5.759 and 6.202 Å in the case of Si, GaAs and CdSe respectively. GGA PW91 [10] approximation for the exchange has been used for binary nanocrystals. Experimentally the bulk lattice constant for these materials are found to be 5.431, 5.658 and 6.051 Å [11].

In all the cases considered we see almost similar trends in the variation of the lattice constant of the layered and spherical nanocrystal as a function of size (Fig. 6.4). The passivated layered nanocrystals approaches the bulk equilibrium lattice constant much faster compared to the passivated spherical nanocrystal. In the case of Si nanocrystals there is just one type of atoms but with the the layered nanocrystals having more number of less coordinated atoms on the surface compared to the spherical nanocrytals. Here we see that the deviations in the average equilibrium lattice constant for similar sized layered and spherical Si nanocrytals are less (Fig. 6.4 (a)).

In the case of binary nanocrystals along with this effect of atoms having different coordination we also have different types of atoms that make up the surface. The layered binary nanocrystals always has one type of atoms on the surface making the surface highly non-stoichiometric, while the spherical nanocrystals has almost a stoichiometric surface. In the case of binary nanocrytals we see that the deviation in the lattice constant for similar sized layered and spherical nanocrytals are more ((Fig. 6.4 (b) and (c)) compared to the Si case (Fig. 6.4 (a)). Considering the case of spherical nanocrystals, the largest size GaAs nanocrystals studied by us shows a deviation of 0.47 % while the largest sized CdSe

Table 6.4: Variation of the average axial and equatorial bond-lengths for the passivated spherical CdSe nanocrystals, having an underlying wurtzite geometry, as a function of nanocrystal size. These nanocrystals have a Cd atom at the center.

Nanocrystal size (n)	Diameter (Å)	Volume (Å^3)		bond-length (Å)
∞	∞	∞	Axial	2.689
			Equatorial	2.686
6	21.17	4389.72	Axial	2.681
			Equatorial	2.674
5	19.86	2899.29	Axial	2.673
			Equatorial	2.671
4	13.08	1095.05	Axial	2.684
			Equatorial	2.660
3	11.28	740.05	Axial	2.656
			Equatorial	2.666

nanocrystals studied by us shows a deviation of 0.40 %. We would like to comment here that the deviations were much smaller in the case of the elemental spherical nanocrystals of Si as shown in the section 6.2.2. While for the largest considered layered nanocrystals the corresponding deviations were 0.20% for Si, 0.07% for GaAs and 0.19% for CdSe. Thus similar sized binary nanocrystals which have different shapes are found to have different equilibrium lattice constants.

A similar analysis carried out for spherical passivated wurtzite nanocrystals of CdSe is given in Table 6.4 Here the radius of the nanocrystal is defined as the distance of the central atom to the outermost atom. The infinite diameter/volume nanocrystal (n=∞) represents the bulk limit. Bulk-like lattice constants are reached much faster than the zinc-blende counterparts.

6.3.3 Conclusion

The effect of surface stoichiometry on the average equilibrium lattice constant of nanocrystals has been studied. Similar sized passivated binary nanocrystals reach bulk-like equi-

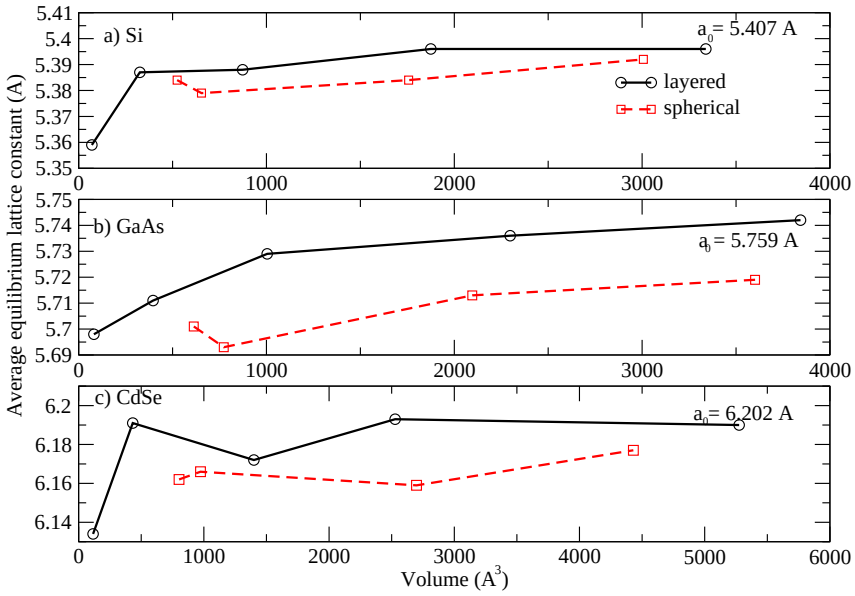

Figure 6.4: Variation of the average equilibrium lattice constant for the passivated layered (solid line and open circles) spherical (dashed line and open squares) nanocrystals of (a) Si, (b) GaAs and (c) CdSe, having an underlying zinc-blende geometry, as a function of nanocrystal size. In the case of GaAs and CdSe nanocrystals, Ga and Se lie at the centers respectively. The theoretically obtained equilibrium bulk lattice constant for each case is given by a_0

librium lattice constants much faster when grown layer by layer than when spherical fragments are considered. This implies that different growth conditions could result in similar sized nanoparticles with different average equilibrium lattice constants.

6.4 Size dependence of the bulk modulus of semiconductor nanocrystals

6.4.1 Introduction

This work focuses on the size dependence of the bulk modulus, which is a measure of the compressibility, of semiconductor nanocrystals. The problem is difficult to address experimentally, as usually synthesized particles exhibit a distribution of sizes. Some studies reveal an enhancement of the bulk modulus for nanocrystals with respect to the bulk values. In the case of AlN nanocrystals having an average particle size of 10 nm an enhancement of about 340 GPa is observed compared to the bulk modulus of 208 GPa for the bulk [12], thus showing an enhancement of 63.4 %. While γ-Fe_2O_3 [13] and CeO_2 [14] nanocrystals showed 50.2 % and 52.2 % bulk modulus enhancement respectively from their bulk values. As all these papers give results for only one specific size of the nanocrystals, the evolution of mechanical properties as a function of size could not be completely investigated. In this context, theoretical calculations which enable to simulate the ideal situation would provide valuable insight into the size dependence. The advantage of these simulations are that they allow to take the ideal systems and and study the size dependence effect on the bulk modulus. The *ab-initio* calculations reported here consider nanocrystals in the size range 0.5 to 5 nm^3, and evaluate the bulk modulus. The motivation of our work lies in proposing a phenomenological rule characterizing the size dependence of bulk-modulus, as a result we can predict the behavior of bigger sizes which is difficult to calculate due to the numerical cost.

6.4.2 Convergence Checks

As part of the convergence test we considered two sizes of n=3 spherical nanocrystals in all the cases and computed the change in energies of the nanocrystals for two different sizes of the cubic supercell considered. Increasing the size of the supercell leads to the increase of the vacuum region separating the nanocrystals. The calculation here was done with an energy cutoff of 312.5 eV in the case of Si, Ge and GaAs while with 342.8 eV as the energy cutoff in the case of CdSe nanocrystals. Its clear from the Table 6.5 that the energy difference is the same in these two sets of supercells considered, thus showing that the chosen vacuum of 8 Å is enough to attain the bulk modulus values accurately. In our present studies we define the amount of vacuum used as the difference of the supercell size and the diameter of the nanocrystal considered. For example in the case of Si nanocrystal considered here, the diameter of the nanocrystal is 12 Å, so in this case the amount of vacuum used is 8 Å. In our studies we have considered vacuum of 10 Å in the case of small size nanocrystals while a vacuum of 8 Å in the case of larger sized nanocrystals.

Since we intended to study the size dependence of the bulk modulus of various nanocrystals first we went to see how much accurately we can find this dependence with minimum computational cost. Doing the calculation for larger size nanocrystals with high energy cutoff are computationally very expensive. For this we started off the analysis with the Si nanocrystals.

Considering vacuum spacing as decided above we calculated the bulk modulus of the spherical Si nanocrystals for nanocrystal sizes n=3 to n=6 for various energy cutoffs. We show the plot (Fig. 6.5) for the Murnaghan equation of state to determine the bulk modulus for the n=3 spherical passivated nanocrystal of Si taking different cutoff energies with the supercell size fixed at the 20 Å. We can see that the equilibrium volume (marked in Fig. 6.5) in these two cases matches quite well. The difference in the equilibrium volume is about 0.16 $Å^3$. But we see that there is difference in the equilibrium energy values (0.5 eV), which is due to the difference in the energy cutoff used. We see that the bulk modulus does not vary much with different energy cutoff considered (Table 6.6). So the trend of the variation of the bulk modulus as a function of size over a large range can be captured well within smaller energy cutoff. Similar studies on convergence were done on the Ge and

Table 6.5: Difference in energies (ΔE in eV) for two sizes of n=3 nanocrystals at two different sizes of supercell considered.

	Supercell size Å	Volume of nanocrystal (Å^3)	Energy (eV)
Si			
	20	523.788	-290.1626
		517.859	-290.1509
ΔE			0.012
	25	523.788	-290.1550
		517.859	-290.1434
ΔE			0.012
Ge			
	20	577.674	-262.9764
		571.561	-262.9523
ΔE			0.024
	25	577.674	-262.9612
		571.561	-262.9386
ΔE			0.023
GaAs			
	23	578.530	-245.1926
		572.408	-245.1774
ΔE			0.015
	28	578.530	-245.1830
		572.408	-245.1676
ΔE			0.015
CdSe			
	22	717.078	-182.0085
		709.990	-181.9894
ΔE			0.019
	27	717.078	-182.0116
		709.990	-181.9940
ΔE			0.018

on the binary nanocrystals of GaAs and CdSe and obtained similar conclusions (Table 6.7) as in the case of Si (Table 6.6).

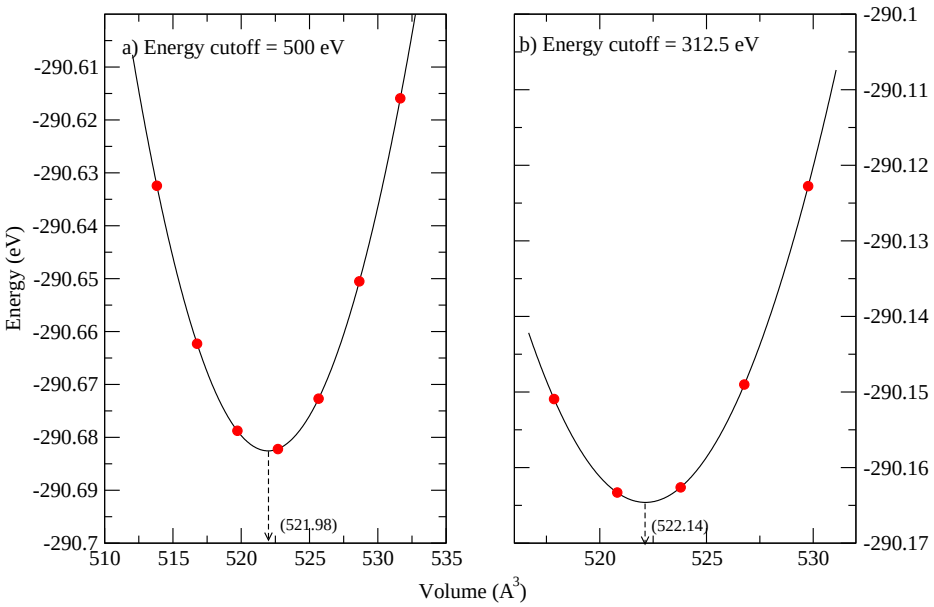

Figure 6.5: Murnaghan equation of state fit for the n=3 spherical nanocrystal of Si for the energy cut off (a) 500 eV and (b) 312.5 eV.

6.4.3 Results and Discussion

The bulk modulus is defined by the equation,

$$B = V\frac{\partial^2 E}{\partial^2 V} = -V\frac{\partial P}{\partial V} \tag{6.2}$$

where, E(V) is the total ground-state energy as a function of volume, P is the pressure, and B is evaluated at the minimum of E(V). Thus, B is considered as the curvature of E(V) at the equilibrium volume. This state is determined by a fit of the Murnaghan equation of states [6].

Table 6.6: Variation of the bulk modulus of spherical Si nanocrystals as a function of size at different energy cutoff considered.

Nanocrystal size (n)	Bulk Modulus (GPa) with energy cutoff		
	250 eV	312.5 eV	500 eV
3	122.7	123.2	122.8
4	117.4	117.0	116.6
5	105.2	105.8	105.4
6	101.3	102.6	-

Table 6.7: Bulk modulus variation of spherical n=3 nanocrystals of Ge, GaAs and CdSe at different energy cutoff considered.

Nanocrystal size	Bulk Modulus (GPa) with energy cutoff		
	250 eV	312.5 eV (for Ge and GaAs) 342.8 eV (for CdSe)	450 eV
n=3 Ge	105.1	106.9	108.1
n=3 GaAs	-	100.1	100.3
n=3 CdSe	-	65.3	65.2

Here it should be noted that determination of bulk modulus strongly depends on the volume computation. From the Eqn. 6.2 it is clear that an error of 25% in the determination of the volume can lead to an error of 33% in the bulk modulus determination. In the case of nanocrytals there is no unique definition for the determination of the volume and here we see that the volume determination is really crucial for the correct description of the bulk modulus estimation of these nanocrystals. In our studies, as said earlier, we determine the volume of the nanocrystals by determining the volume of the convex hull formed by the surface atoms.

Table 6.8 below gives the size dependence of the bulk modulus of the nanocrystals considered using LDA as the exchange. The desired vacuum in these calculations are set as described in section 6.4.2 and the calculation here was done with an energy cutoff of 312.5 eV in the case of Si, Ge and GaAs while with 342.8 eV as the energy cutoff in the case of CdSe nanocrystals. For bulk Si, Ge, GaAs and CdSe our calculated bulk modulus values are 97.0, 72.3, 75.1 and 57.5 GPa while experimentally [11] these are found to be 98, 77.2, 75 and 53 GPa respectively. Here we do find an enhancement of the bulk modulus in the nanosize regime in every case (Table 6.8). Cohen had [11] calculated the bulk moduli of diamond and zinc-blende solids and arrived at a scaling law in which the bulk modulus of these materials depends on the nearest neighbor separation. Thus the observed enhancement of bulk modulus in the nanosize regime can be attributed to the changes in the bond-length. In the case of the nanocrystals there is no uniform bond-lengths, while it exhibits a bond strain profile as explained in section 6.2. Using the averaged bond-lengths values and using Cohen's scaling relation we see very small enhancement in the bulk modulus in the nanoregime, this is because the averaged bond-lengths for the passivated nanocrystals attains its bulk like value for very small sizes itself (section 6.2). Hence Cohen's scaling law cannot be used in the nanoregime.

A fit of all the available data allows us to extract a dependence describable by the phenomenological rule

$$B_0 = B_\infty exp(\frac{k}{V}) \tag{6.3}$$

where, B_0 is the bulk modulus, B_∞ is the corresponding value for the bulk, k a material

Table 6.8: Bulk modulus calculated for different size of semiconductor nanocrystals (using LDA as the exchange). The size of nanocrystals is both indicated in term of layer number (n) and volume.

Nanocrystal size (n)	Volume (Å^3)	Bulk modulus (GPa)
Si		
∞	∞	97.0
3	522.14	123.2
4	651.32	117.0
5	1751.52	105.8
6	2995.34	102.6
Ge		
∞	∞	72.3
3	577.81	106.9
4	724.36	99.2
5	1959.26	87.8
6	3349.30	83.9
GaAs		
∞	∞	75.1
3	577.72	100.1
4	727.48	96.3
5	1960.41	86.1
6	3372.74	82.9
CdSe		
∞	∞	57.5
3	718.21	65.3
4	922.54	63.6
5	2449.63	57.1
6	4234.44	55.0

parameter consistent to a volumic density, and V the volume. The Fig. 6.6 presents the plot of the function here obtained and the corresponding *ab-initio* computations. The parameter 'k' also has a physical significance, it gives an estimate of the volume of a particular nanocrystal below which the enhancement of bulk modulus is greater than 170 %.

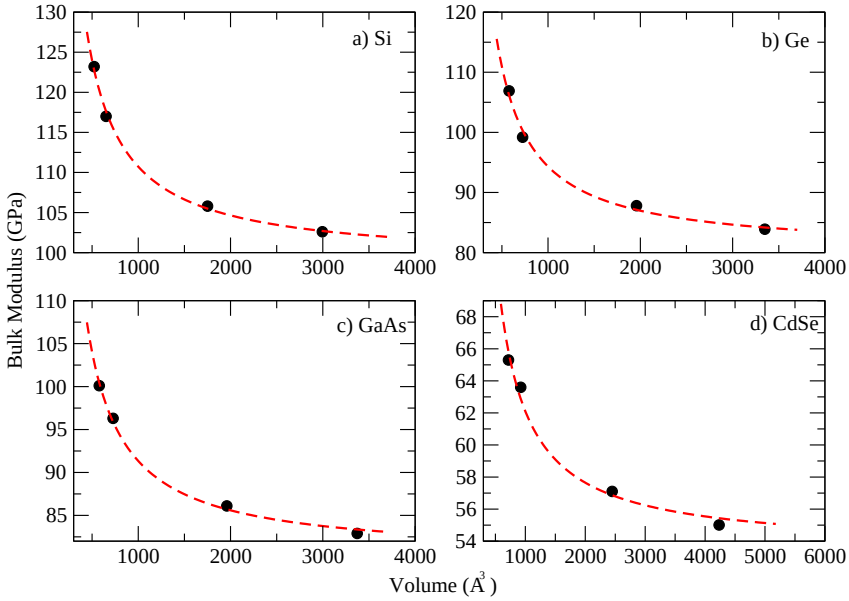

Figure 6.6: Bulk modulus as function of nanocrystal sizes for Si, Ge, GaAs, and CdSe using LDA as the exchange. In dot, the results of *ab-initio* computations. In line, the phenomenological rule determined by fitting all the computation results.

We have not included the bulk modulus of the extended solid in our fitting, but we compare it to the asymptote of our fit function. Table 6.9 indicates the fit details. The deviation between the asymptote of function proposed here and the bulk value is the largest for Ge and its about 10 %. All curves allows an asymptote very close to the bulk value. This gives us greater confidence in our volume computation of the nanocrystals and thus a much better confidence in the the phenomenological relation that we have derived here.

Table 6.9: Results of the fit performed on different nanocrystals using LDA as the exchange.

Nanocrystal	Bulk limit bulk modulus (B_0^{fitted}) (GPa) obtained from fitting	Bulk modulus (B_0^{actual}) (GPa)	k (Å^3)	% deviation between B_0^{fitted} and B_0^{actual}
Si	99.0	97.0	112.95	2.0
Ge	80.2	72.3	162.18	9.8
GaAs	80.2	75.1	129.94	6.3
CdSe	53.5	57.5	148.77	7.5

Table 6.10: Prediction of the size dependence for a 10 nm^3 nanocrystal using the phenomenological law.

Nanocrystal	B_0(GPa)	Fitted B_∞ (GPa)	% deviation
Si	100.1	99.0	1.1
Ge	81.5	80.2	1.6
GaAs	81.2	80.2	1.2
CdSe	54.3	53.5	1.5

The nanocrystal size studied here is evidently a little small compared with those more often experimentally observed. On the other hand, defining a phenomenological law enables to predict the behavior of bigger sizes, more difficult to calculate due to the numerical cost. Thus, Table 6.10 shows the size dependence expected for a 10 nm^3 nanocrystal, size more often experimentally observed.

We also tried GGA exchange for the binary nanocrystals and verified that the trend observed here is not a result of the exchange functional used. The results in these cases are given in Table 6.11. Here too we were able to fit the bulk modulus variation (Fig. 6.7) for the binary nanocrystals using the same phenomenological rule as described in Eqn. 6.3. The fitted details in this case is given in Table 6.12.

Table 6.11: Bulk modulus calculated for different size of semiconductor nanocrystals (using GGA as the exchange). The size of nanocrystals is both indicated in term of layer number (n) and volume.

Nanocrystal size (n)	Volume (Å^3)	Bulk modulus (GPa)
GaAs		
∞	∞	62.5
3	613.067	89.6
4	772.317	84.6
5	2094.795	73.8
6	3601.500	69.9
CdSe		
∞	∞	45.1
3	801.999	65.0
4	972.137	59.8
5	2703.379	48.3
6	4431.198	49.4

Table 6.12: Results of the fit performed on the binary nanocrystals using GGA as the exchange.

Nanocrystal	Bulk limit bulk modulus (B_0^{fitted}) (in GPa) obtained from fitting	Bulk modulus (B_0^{actual}) (in GPa)	% deviation between B_0^{fitted} and B_0^{actual}
GaAs	67.1	62.5	7.4
CdSe	44.8	45.1	0.4

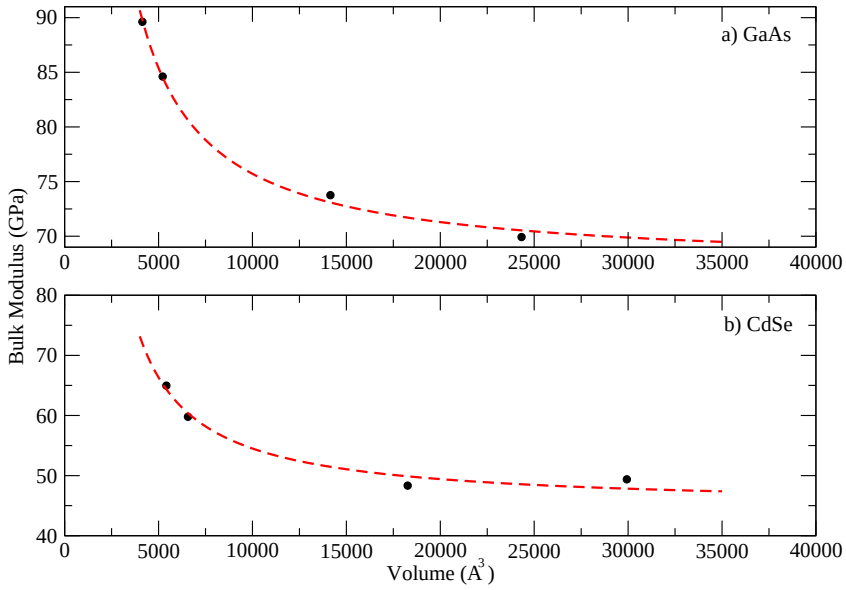

Figure 6.7: Bulk modulus as function of nanocrystal sizes for GaAs, and CdSe using GGA as the exchange. In dot, the results of *ab-initio* computations. In line, the phenomenological rule determined by fitting all the computation results.

6.4.4 Conclusion

We have studied the size dependence of the bulk modulus nanocrystals of Si, Ge, CdSe and GaAs. An enhancement is seen in the small size regime and this we attribute to the bond strain that exist in these nanocrystals. A phenomenological law is derived which in most cases has the correct magnitude in the asymptotic limit.

Bibliography

[1] As there are conflicting reports of CdSe nanoparticles favoring the zinc-blende/wurtzite structure, we have considered both polymorphs.

[2] A full geometry optimization has not been attempted by us, and it is indeed true that at very small sizes the shapes of the nanocrystals may be very different from the bulk. These shapes may lead to different coordinations of the atoms and may result in stronger deviations in the lattice constant than has been observed here.

[3] G. M. Dalpian, M. L. Tiago, M. L. Puerto, and J. R. Chelikowsky, Nano Lett., **6**, 501 (2006).

[4] M. A. Marcus, L. E. Brus, C. Murray, M. G. Bawendi, A. Prasad, and A. P. Alivisatos, Nanostructured Materials **1**, 323 (1992); P. J. Wu, Y. P. Stetsko, K. D. Tsuei, R. Dronyak, and K. S. Liang, Appl. Phys. Lett. **90**, 161911 (2007).

[5] X. Huang, E. Lindgren, and J. R. Chelikowsky, Phys. Rev. B **71**,165328 (2005).

[6] F. D. Murnaghan, Proc. Natl. Acad. Sci. U.S.A. **30**, 244 (1944).

[7] S. J. L. Billinge, and I. Levin, Science **316**, 561 (2007).

[8] N. Herron, J. C. Calabresse, W. E. Farneth, and Y. Wang, Science **259**, 1426 (1993).

[9] A. S. Masadeh, E. Bozin, C. L. Farrow, G. Paglia, P. Juhas, S. J. L Billinge, A. Karkamkar, and M. G. Kanatzidis, Phys. Rev. B **76**, 115413 (2007).

[10] J. P. Perdew, and Y. Wang, Phys. Rev. B **45**, 13244 (1992).

[11] M. L. Cohen, Phys. Rev. B **32** 7988 (1985).

[12] Z. Wang, K. Tait, Y. Zhao, D. Schiferl, C. Zha, H. Uchida, and R. T. Downs, J. Phys. Chem. B **108**, 11506 (2004).

[13] J. Z. Jiang, J. S. Staun Olsen, L. Gerward, and S. Morup, Europhys. Lett. **44**, 620 (1998).

[14] Z. Wang, S. K. Saxena, V. Pischedda, H. P. Liermann, and C. S. Zha, Phys. Rev. B **64**, 012102 (2001).

Chapter 7

Growth of nanocrystals

7.1 Introduction

As the size of materials is decreased and one enters into the regime of dimensions in nanometers, one finds significantly different properties than in the bulk. The strong dependence of physical properties on size, found especially in semiconductors has significant technological implications and this coupled with the ease of fabrication and processing makes this class of materials promising building blocks for materials with designed functions [1]. An access to a control of the properties requires an ability to control the uniformity of size, shape, composition, crystal structure and surface properties. In this work we theoretically examine two limiting scenarios of nanoparticle growth and determine the extent of control that can be achieved on the surface structure and the consequences.

Colloidal chemistry route to nanoparticle synthesis [2] has emerged as a popular route to semiconductor nanoparticles with tremendous applications [3]. Colloidal nanocrystals are made up of an inorganic core which is preserved because of a surface layer of organic molecules. The typical size regime in which the properties show quantum effects are similar to the size regime in which one finds large organic macromolecules. Tremendous precision has been achieved in the latter case. It is therefore the hope that one can achieve the same kind of control in these inorganic macromolecules. While this has still not been achieved to the extent that one desires, in the past decade there have been significant advances in narrowing the size distribution of the synthesized nanoparticles.

A typical synthesis consists of 3 components - precursors, organic surfactants and solvents. Initially the precursors decompose in solution or react at relatively high temperature to form a supersaturation of monomers followed by a burst of nucleation centers and growth of nanoparticles. While high growth rates lead to highly anisotropic shapes with high energy forms, low growth rates result in nanocrystals that are round in shape and correspond to the equilibrium structure where the guiding principles are those of equilibrium thermodynamics [4].

A passivant which is usually an organic surfactant is used to prevent agglomeration of nanocrystals. This moiety as its name suggests attaches itself to the surface of the nanocrystal and saturates all dangling bonds so that optical transitions observed in these materials are not between surface states [5, 6]. The choice of passivant turns out to be especially difficult in the case of binary nanocrystals as it must attach itself to both the cation as well as the anion atoms at the surface and saturate the generated dangling bonds for both cases. We illustrate this considering the example of CdSe with TOP as the passivant. TOP functions as a good passivant for Se atoms at the surface. However, it reacts with the Se atoms that exist in the solution to form TOPSe. These bind to the Cd atoms on the surface and quench the photoluminescence possibly by introducing surface states [6]. Hence surface stoichiometry turns out to be crucial for the enhanced optical efficiency in the nano-regime. If one could generate binary nanocrystals with only one type of atoms at the surface, one can improve the quantum efficiency dramatically. There have been efforts in controlling the surface stoichiometry during synthesis but there is no clear strategy [7]. We started out by asking the question whether nanocrystals with just one type of atoms at the surface can form theoretically. Considering two prototypical examples of GaAs and CdSe respectively, we calculate the formation energies per binary atom as a function of the allowed range of chemical potentials. Highly off-stoichiometric nanocrystals with just one type of atom at the surface are strongly favored over stoichiometric ones at the same size. This tendency we find strongly depends on the strength of the molecule used as the passivant. Considering the opposite limit of no passivant molecule in our calculations, we find that stoichiometric nanocrystals are favored.

7.2 Methodology

In order to examine the growth mechanism, we constructed nanocrystals of GaAs and CdSe. The underlying tetrahedral coordination of the bulk lattice was preserved while constructing the nanocrystals, though the scheme of truncation chosen was different. Here we considered layered nanocrystals and spherical nanocrystals as discussed in section 6.1. The layered nanocrystals are highly off-stoichiometric while the spherical ones are nearly stoichiometric by construction. The surface of the nanocrystals were passivated with pseudo-hydrogens [8] and the positions of the atoms were optimized to the minimum energy configuration. In order to calculate the total energy of the nanocrystals, periodic nanocrystals separated by almost 10 Å of vacuum were considered. The electronic structure was solved within a plane-wave pseudopotential method using VASP. PAW potentials [9] were used in which the Ga *d* states were treated as a part of the core. The GGA PW91 approximation [10] to the exchange has been used. The calculations were performed at Gamma point alone. As the nanocrystals consist of different number of atoms, as well as differing stoichiometry in the case of binary semiconductors, we use the formation energy per binary atom defined according to

$$\begin{aligned}\Delta H_f &= \frac{1}{(m+n)}[E(A_mB_nH1_pH2_q) - mE(A) \\ &\quad -nE(B) - pE(H1) - qE(H2) \\ &\quad -m\mu_A - n\mu_B] \end{aligned} \tag{7.1}$$

to compare the relative stabilities. Here, $E(A_mB_nH1_pH2_q)$ is the total energy of the nanocrystal consisting of m atoms of element A, n atoms of element B and p/q atoms of the two types of pseudo-hydrogen atoms while E(A) and E(B) are the energies of the elements A and B in their most stable structure. E(H1) and E(H2) have been evaluated considering a molecule formed by the pseudo-hydrogens respectively. We have considered the orthorhombic structure for Ga [11], rhombohedral structure for As [12] and hexagonal structure for both Cd [13] and Se [14] at their experimental lattice constants to evaluate the energies of the bulk solids entering the expression for the formation energy. Geometry

optimization of the internal positions was however carried out. The chemical potentials μ_A and μ_B are determined by the criterion for stability of the bulk solids.

7.3 Results and Discussion

In Fig. 7.1 we have plotted the total density of states for layered Se centered n=4 CdSe nanocrystals for the case where there is no passivating layer, and the surface has just been terminated without allowing for surface reconstructions. The total density of states for the passivated CdSe nanocrystals have been provided. The alignment of the energies of the two different calculations has been made with respect to the d levels of the Cd atom at the core of the the nanocrystal. The latter set of calculations enable us to define the band edges. We find that as a result of the passivant, surface states generated in the gap, as shown in panel (b) of Fig. 7.1, are moved into the valence band by approximately 0.5 eV. Hence there are two possible scenarios. The first in which the passivant serves the role of merely of an electron donor/acceptor as the case may be depending on the surface termination. In such a case the expectation is that there is strong reconstruction of the surface which moves the surface states out of the band gap region. The second is one where the passivant interacts with the atoms comprising the surface. Now moving the surface states by 0.5 eV would imply very strong interactions between the passivant molecule and the nanocrystal surface. Considering the case of pseudo-hydrogen atoms as passivating atoms, we examine which of the two scenarios is realized and the consequences of the same.

The passivant considered by us is "near-ideal" in the sense that all states introduced in the band gap in the absence of the passivant are moved out of the band gap. In Fig.7.2 we have plotted the charge density corresponding to the valence band maximum (VBM) and conduction band minimum (CBM). The CBM has dominant weight (Fig.7.2) on the central atom, while the VBM has the maximum weight on the first shell of the anions for the cation-centered nanocrystals. This is what one would expect for proper confinement.

The pseudo-hydrogens in this case compared to the organic passivants used in the

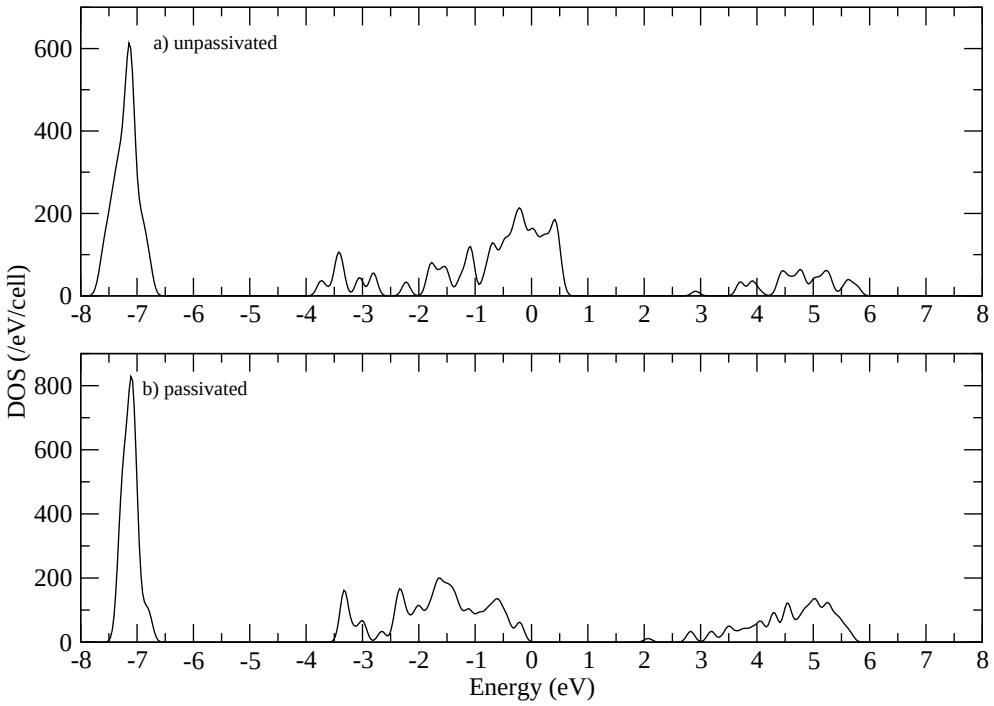

Figure 7.1: The total density of states for the Se-centered layered n=4 nanocrystal for two cases. (a) In the absence of any passivating layer and without allowing any surface reconstructions and (b) in the presence of a passivating layer and allowing for surface reconstructions.

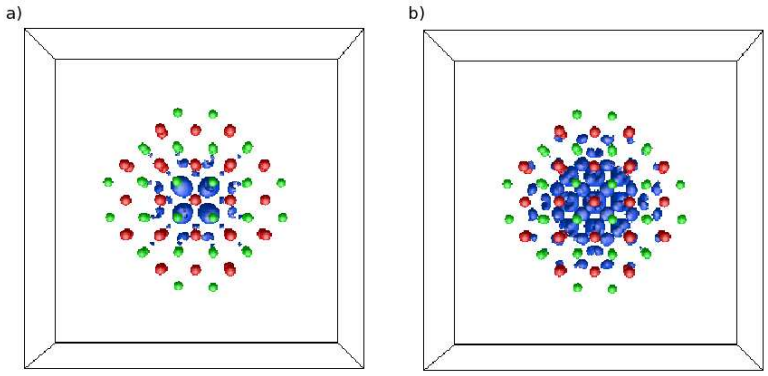

Figure 7.2: The isosurface plots of the wavefunction squares of (a) VBM and (b) CBM for the passivated CdSe spherical nanocrystal (with 5 layers around the central Cd atom). The Cd and Se atoms are shown in dark and light colored balls respectively. The pseudo-hydrogen atoms are not shown.

experiments. Here, we find, that they interact strongly with the surface atoms. For the surface Se atom of a n=4 passivated nanocrystal we plot the Se-p projected partial density of states. The corresponding partial density of states of the H atom to which it is attached is also given. There is substantial admixture of H-s states with the Se-p states as a result of their interaction (Fig. 7.1). Even in the case of Cd terminated nanocrystals (n=5 passivated nanocrystal) we see the same effect where the pseudo-hydrogen atoms shows a strong interaction with the surface Cd atoms (Fig. 7.4). What then are the consequences of this strong interactions ?

We have examined the formation energies per binary atom were computed for both spherical as well as layered nanocrystals as a function of size. Here under both cation-rich conditions as well as anion-rich conditions we find (Fig. 7.5) much to our surprise that the non-stoichiometric layered nanocrystals are favored. Two different semiconductors were considered by us for our study and both show the same behavior as a function of size. The atom making up the terminating layer of the nanocrystal before passivation have been

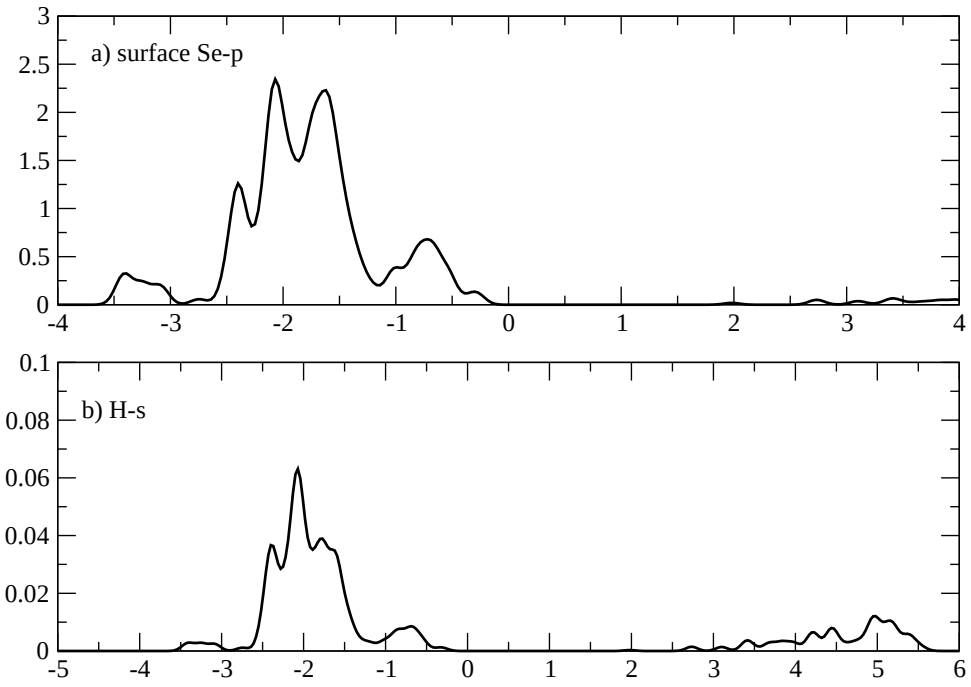

Figure 7.3: The (a) Se p projected partial density of states for a surface Se atom (having a coordination of 1 with the Cd atoms) and (b) the H s projected partial density of states for the pseudo-hydrogen attached to the surface Se atom in the case of a Se-centered layered n=4 nanocrystal. The Fermi energy is set to zero.

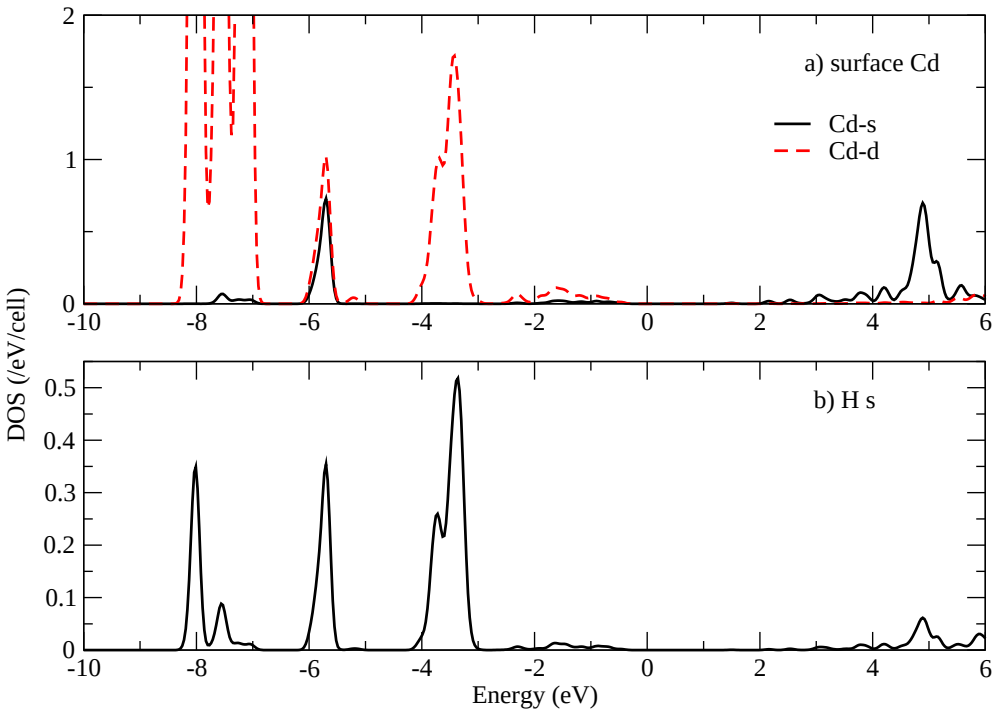

Figure 7.4: The (a) Cd *s* (solid line) and *d* (dashed line) projected partial density of states for a surface Cd atom (having a coordination of 1 with the Se atoms) and (b) the H *s* (dotted line) projected partial density of states for the pseudo-hydrogen attached to the surface Cd atom in the case of a Se-centered layered n=5 nanocrystal. The Fermi energy is set to zero.

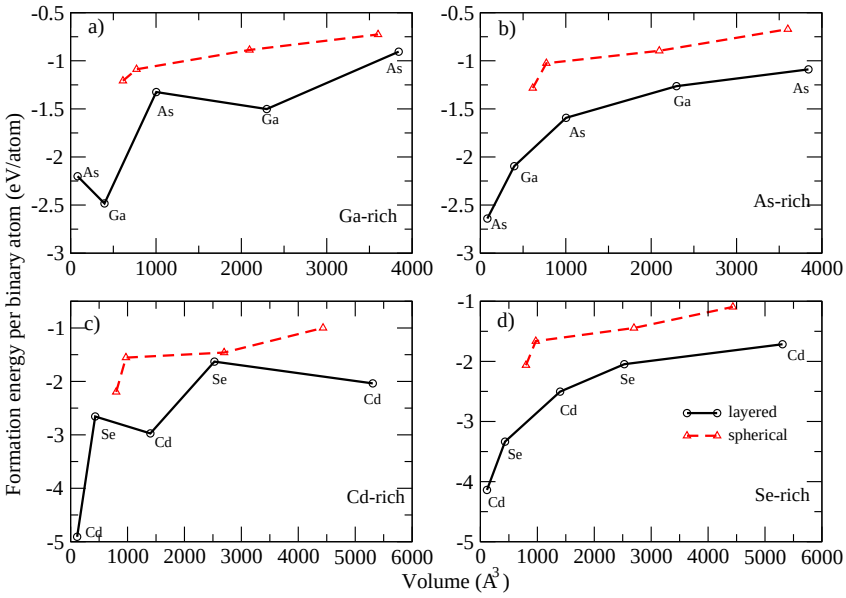

Figure 7.5: Variation of the formation energy per binary atom for the passivated binary nanocrystals of GaAs and CdSe as a function of volume for the layered and spherical nanocrystals under cation-rich (left panel) and anion-rich (right panel) conditions. In the case of GaAs and CdSe, Ga and Se lie at the centers respectively. The type of atom that forms the outermost layer in the case of the layered nanocrystals have been indicated.

indicated on the figure. Under cation-rich conditions we find that the formation energy for cation terminated nanocrystals follow a different curve compared to that followed by anion terminated nanocrystals. The former are significantly lower suggesting that under cation-rich conditions one finds equilibrium growth conditions resulting in a particular surface stoichiometry for the nanocrystals. Under anion-rich conditions both termination types follow a single curve.

We then went on to consider the limit of unpassivated nanocrystals. Here, as shown in Fig. 7.6 chemical potentials did not have such a strong effect on the type of nanocrystals which were favored. Under both cation rich conditions as well as anion rich conditions we found that stoichiometric nanocrystals were favored. These results have important

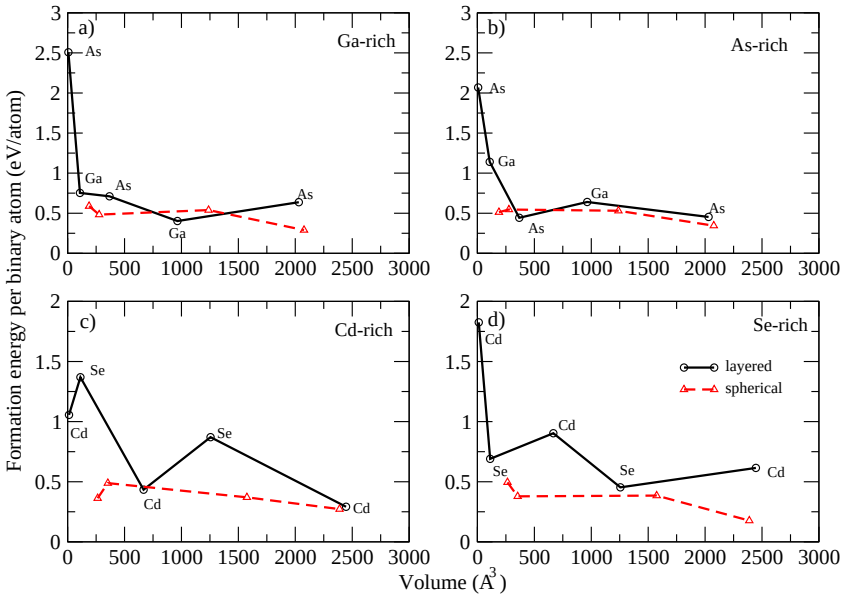

Figure 7.6: Variation of the formation energy per binary atom for the unpassivated binary nanocrystals of GaAs and CdSe as a function of volume for the layered and spherical nanocrystals under cation-rich (left panel) and anion-rich (right panel) conditions. In the case of GaAs and CdSe, Ga and Se lie at the centers respectively. The type of atom that forms the outermost layer in the case of the layered nanocrystals have been indicated.

implications on the growth of nanocrystals and their consequent properties. Firstly, it is not always that one can find a suitable passivant for all atoms comprising the nanocrystal. Hence, these results suggest that as a function of the strength of the passivant we have a crossover from stoichiometric nanocrystals to highly non-stoichiometric nanocrystals. While the most prevalent view of the role of the passivant is one of saturating dangling bonds as well as arresting growth, there are indications from the literature [15] that the passivant plays a complex role during growth. The results of Figs. 7.5 and 7.6 and the subsequent analysis throws some light on this unidentified role of the passivating molecules.

In order to understand the differences in the stability of the stoichiometric nanocrystals as against the non-stoichiometric ones, we have examined the differences in their electronic structure. Considering the layered CdSe nanocrystal with an Se atom at the center and four layers around the central core (n=4), the surface layer is found to be made up of Se atoms. These Se atoms could be 1-, 2- or 3- coordinated with the Cd atoms.

In Fig. 7.7 we have plotted the Se p projected partial density of states for the under-coordinated surface Se atoms as well as inner Se atom located at the center (core) of the nanocrystal. The centroid appears to be shifted towards lower energies for the surface Se atom compared to the core Se atom. This can be understood as arising from the interaction between the pseudo-hydrogen atom belonging to the passivant and the Se p states belonging to the Se atom at the surface. Here the shifting of the centroid towards lower energy is more pronounced for the less coordinated Se atoms. A Se-terminated surface is deficient in cations and the dangling bond states may be considered to be arising from cation vacancies. These are known to be centered on the Se atoms surrounding the cation vacancy. Hence when we passivate the dangling bonds with pseudo-hydrogen, the latter atoms behave like a cation, interact with the Se p states and push them deeper into the valence band. A similar analysis has been carried out for the Cd-terminated surface.

In Fig. 7.8 we have plotted the Cd s projected partial density of states for the surface Cd atoms which have different coordination as well as inner Cd atom. For the less coordinated Cd atoms we see that the centroid shifts towards lower energy compared to the inner Cd atom. Here the passivant atoms behave like an anion, interacting with the

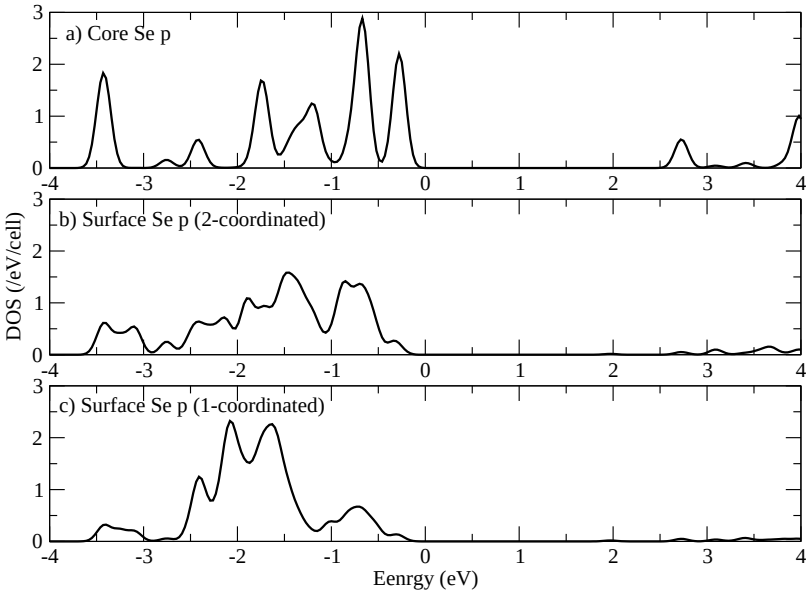

Figure 7.7: The Se p projected partial density of states for a Se atom at (a) the core as well as at the surface having (b) double and (c) single coordination with the Cd atoms. The zero of energy corresponds to the Fermi energy.

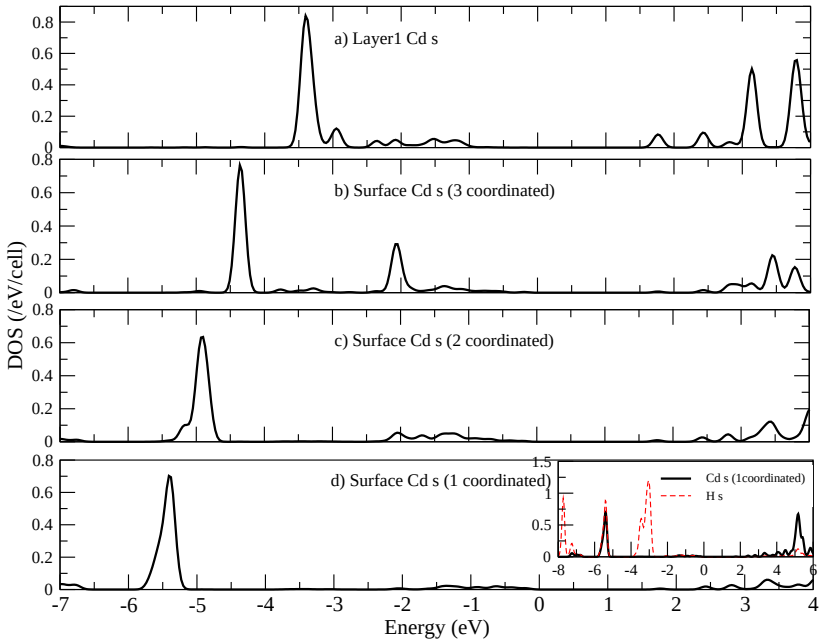

Figure 7.8: The Cd *s* projected partial density of states for a Cd atom (a) in the first layer as well as at the surface having (b) triple, (c) double and (d) single coordination with the Se atoms. The inset in (d) shows the Cd *s* (solid line) states, belonging to a surface Cd atom having single coordination with the Se atoms, and H *s* (dashed line) contribution to the partial density of states corresponding to the passivating pseudo-hydrogen atom. The zero of energy corresponds to the Fermi energy.

Cd-centered dangling bond states forming bonding and antibonding states as the inset of Fig. 7.8(d). There is substantial transfer of charge onto the passivant atom as a result of the interaction.

Table. 7.1 shows the number of surface atoms and the type of coordination one has for the different types of 'A' centered layered and spherical binary 'AB' nanocrystals considered by us.

Table 7.1: Number (types of atom) of 'A' centered binary nanocrystals.

	Number of atoms with coordination				% of single and double coordinated atoms
	1	2	3	4	
Layered					
n=1	4(B)	-	-	1(A)	80
n=2	12(A)	-	-	1(A),4(B)	71
n=3	12(B)	12(B)	-	13(A),4(B)	59
n=4	24(A)	18(A)	-	13(A),28(B)	51
n=5	24(B)	36(B)	4(B)	55(A),28(B)	41
Spherical					
n=3	-	12(B)	12(A)	1(A),4(B)	41
n=4	-	6(A)	12(A),12(B)	1(A),4(B)	17
n=5	-	12(A),12(B)	12(A),16(B)	19(A),16(B)	28
n=6	-	24(A)	24(A),28(B)	31(A),40(B)	16

Examining the coordination of surface and bulk atoms in the layered nanocrystals (Table. 7.1), we find that the percentage of undercoordinated (one and two coordinated) atoms is larger for the layered nanocrystals than for the spherical nanocrystals. This explains the unusual stability of the layered nanocrystals irrespective of their termination.

The next question we asked was how exactly could these theoretical predictions be verified. In Ref. [16], Nanda *et al.* have used core-level spectroscopy to determine how many structurally inequivalent types of Cd and S are there in their CdS nanocrystal. By an analysis of the core-level photoemission spectrum, they arrived at the conclusion that there were three inequivalent S species, while there was just one type of Cd atom in their nanocrystal. The three S atoms are attributed to surface S, bulk S and another belonging

Table 7.2: Variation of the average equilibrium lattice constant for the unpassivated layered and spherical nanocrystals of GaAs and CdSe. In the case of GaAs and CdSe nanocrystals, Ga and Se lie at the centers respectively.

	Nanocrystal size (n)	Average lattice constant (Å)	
		GaAs	CdSe
layered	1	5.405	6.571
	2	5.875	6.228
	3	5.826	6.626
	4	6.041	6.338
	5	5.806	6.364
	∞	5.759	6.202
spherical	3	5.674	6.124
	4	5.726	6.075
	5	5.736	6.152
	6	5.871	6.169
	∞	5.759	6.202

to the passivant molecule they use. These results are suggestive of a S-terminated surface being realized. Further experiments of a similar kind may be used to verify our conjecture.

We go on to examine the limitations on the choice of a non-ideal passivant. An obvious limitation of the non-ideal passivant is in the optical properties. In most cases defect states are generated in the band gap as a result of unpassivated dangling bonds and these quench the bulk band-edge transitions. An alternate consequence that we found in the course of our calculations was in the evaluated equilibrium lattice constant. This is computed for the nanocrystals by first performing a geometry optimization, and then averaging over the nearest neighbor bond lengths. The averaged bond length is then converted to an average lattice constant which we then compare with the bulk value. For the passivated nanocrystals bulk-like equilibrium lattice constants were reached for the moderate sizes (refer section 6.3.2). Also the lattice constants showed an almost monotonic increase with size, approaching the bulk equilibrium lattice constant. In the case of the unpassivated nanocrystals, a non-monotonic behavior of the lattice constant is found as a function of size (Table. 7.2), with the lattice constant being larger than the bulk lattice constant for some

sizes. This larger deviations in the lattice constant arises for the unpassivated nanocrystals as the perturbation effects are more. While in the case of passivated nanocrystals these perturbation effects are reduced as the passivants saturates the dangling bonds that exist at the surface of the nanocrystals. These results have implications on the experimental studies where one might have different types of passivants and the role played by the passivants is strongly reflected on the lattice constant of the nanocrystal. Our studies show that a nanocrystal in presence of a strong passivant shows much less deviation in the lattice constant from the bulk lattice constant compared to the case when the nanocrystals are passivated by a weak passivant. Experimentally it has been observed that the lattice constant is larger than the bulk lattice constant for some nanocrystals [17]. This we believe is due to the use of weak passivant.

7.4 Conclusions

Passivated binary nanocrystals with only one kind of atoms are found to be favored under certain experimental conditions. These are important from a technological point of view for maximizing optical efficiency. A weak passivant on the other hand favor's the formation of spherical nanocrystals which although stoichiometric show significant deviations from the average equilibrium lattice constant evaluated for similar sized well passivated nanocrystals. This study reveals a new role played by passivant molecules. In addition to their traditional role of saturating dangling bond states and arresting growth and therefore preventing agglomeration of particles, here they also alter the surface structure of the grown particles.

Bibliography

[1] A. P. Alivisatos, Science **271**, 933 (1996); A. P. Alivisatos, J. Phys. Chem. **100**, 13226 (1996); Y. Cui, Q. Wei, H. Park, and C. M. Lieber, Science **293**, 1289 (2001).

[2] C. B. Murray, D. J. Norris, and M. G. Bawendi, J. Amer. Chem. Soc. **115**, 8706 (1993); D. V. Talapin, A. L. Rogach, A. Kornowski, M. Haase, and H. Weller, Nano. Lett. **1**, 207 (2001).

[3] X. Michalet, F. F. Pinaud, L. A. Bentolila, J. M. Tsay, S. Doose, J. J. Li, G. Sundaresan, A. M. Wu, S. S. Gambhir, and S. Weiss, Science **307**, 538 (2005); N. Tessler, V. Medvedev, M. Kazes, S. Kan, and U. Banin, Science **295**, 1506 (2002).

[4] Z. A. Peng,and X. Peng, J. Am. Chem. Soc. **123**, 1389 (2001); T. S. Ahmadi, Z. L. Wang, T. C. Green, A. Henglein, and M. A. El-Sayed, Science **272**, 1924 (1996).

[5] G. Kalyuzhny,and R. W. J. Murray, J. Phys. Chem. B **109**, 7012 (2005); C. Bullen, and P. Mulvaney, Langmuir **22**, 3007 (2006).

[6] J. Jasiniak, and P. Mulvaney, J. Amer. Chem. Soc. **129**, 2841 (2007).

[7] J. E. B. Katari, V. Colvin, and A. P. Alivisatos, J. Phys. Chem. **98**, 4109 (1994); B. O. Dabbousi, J. Rodriguez-Viejo, F. V. Mikulec, J. R. Heine, H. Mattoussi, R. Ober, K. F. Jensen, and M. G. Bawendi, J. Phys. Chem. B **101**, 9463 (1997); J. Taylor, T. Kippeny, and S. J. Rosenthal, J. Cluster Sci. **12**, 571 (2001); L. Qu, and X. Peng, J. Am. Chem. Soc. **124**, 2049 (2002).

[8] X. Huang, E. Lindgren, and J. R. Chelikowsky, Phys. Rev. B **71**, 165328 (2005).

[9] G. Kresse, and J. Joubert, Phys. Rev. B **59**, 1758 (1999).

[10] J. P. Perdew, and Y. Wang, Phys. Rev. B **45**, 13244 (1992).

[11] B. D. Sharma and J. Donohue, Z. Kristallogr. **177**, 293 (1962).

[12] D. Schiferl and C.S. Barrett, Journal of Applied Crystallography **2**, 30 (1969).

[13] E. R. Jette and F. Foote, J. Chem. Phys. **3**, 605 (1935).

[14] P. Cherin and P. Unger, Inorg. Chem., **6 (8)**, 1589 (1967).

[15] R. Viswanatha, H. Amenitsch, and D. D. Sarma, J. Am. Chem. Soc. **129 (14)**, 4470 (2007).

[16] J.Nanda, B. A. Kuruvilla and D. D. Sarma, Phys. Rev. B **59**, 7473 (1999).

[17] T. Sarkar, B. Ghosh, A. K. Raychaudhuri, and T. Chatterji, Phys. Rev. B. **77**, 235112 (2008).

Chapter 8

Optical properties of semiconductor nanocrystals

8.1 Can Nano Silicon be Made Optically Active?

8.1.1 Introduction

Silicon has been the workhorse of the electronic industry. With progress in the communications industry based on optoelectronic materials, efforts are on to integrate the two and make a silicon based optoelectronic industry. Bulk Si is an indirect band gap material and is therefore not a candidate. Efforts have been made to look for other forms of silicon which might be optically active. Routes that have been taken include quantum confinement of Si between SiO_2 layers [1], porous silicon [2] as well as quantum dots / nanosized particles of Si [3]. While the size dependence of the electronic structure and therefore the optical properties is well-known for II-VI and II-IV semiconductors [4], the exact mechanism by which the material is rendered optically active is still an enigma. This is aggravated also by the experimental uncertainties arising from different growth methods giving different results. In this context theory which can simulate the ideal situation can play an important role. Focusing on nanoparticles of Si, we examine how different criteria for cutting out nanocrystals from bulk fragments can modify the degeneracies of the conduction band minima. We examine whether this method of artificially modifying the degeneracies renders silicon optically active.

[1]This section is based on the following paper:
R. Cherian, A. K. Nandy, and P. Mahadevan *Can Nano Silicon be Made Optically Active?* J. Nanoscience and Nanotechnology, **9**, 5561 (2009).

8.1.2 Methodology

Here passivated layered and spherical nanocrystals, as discussed in section 6.1, were considered. For the studies here a plane wave cutoff of 500 eV has been used for the basis states. It should be noted that for very small nanocrystal sizes, bulk-like coordination is usually not reached and the nanocrystals have very different geometries and coordination then what is found in bulk. However we are interested in nanocrystals with bulk-like geometries usually attained in the larger size considered here. For the optimized structure we use the longitudinal length gauge of the electromagnetic field defined as used by Adolph *et al.* [5] to evaluate the optical matrix elements.

A good test of any model is its ability to predict the physical properties. We have considered the equilibrium lattice constant as our yardstick. For our optimized structure, we average over all Si nearest neighbor bond-lengths to determine an average bond-length. This is then translated into an equilibrium lattice constant. This is contrasted with the value of the equilibrium lattice constant for bulk Si, which is found to be 5.407 Å (refer section 6.2.2). This value is 0.44% smaller than the experimental lattice constant and it is well known failure of these calculations resulting from the choice of exchange. However the qualitative trends coming out of such calculations are usually reliable. In our calculations for the largest nanocrystal considered here we obtain an average equilibrium lattice constant of 5.392 Å (Ref. Table 6.3). Thus our nanocrystals seem to be reproducing the values of nano Si quite well. We then went on to examine the physical properties of the systems. Considering the band gap of the systems studied we found that the passivation was efficient in every case and eliminated all mid gap defect states.

8.1.3 Results and Discussion

The band gap variation for the nanocrystal generated by the two methods discussed earlier are given in Figs. 8.1 and 8.2 as a function of the volume of the nanocrystal. We define the volume of the nanocrystal as the volume of the convex hull formed by the outermost atoms. We next went on to examine whether the physical properties of two nanocrystals with the same volume, but different shapes could be different. Considering the layered

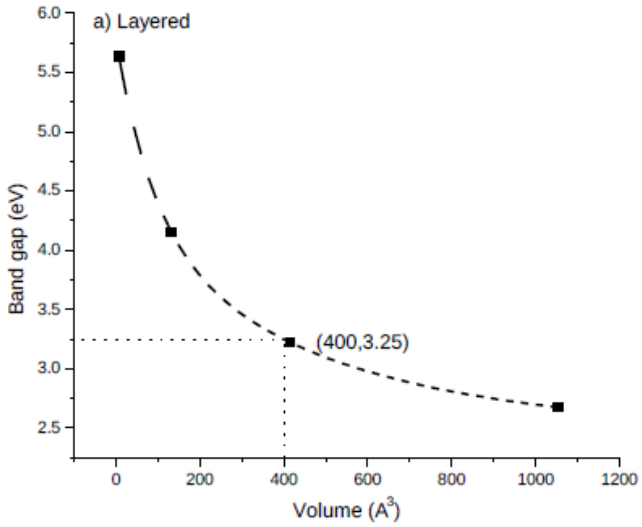

Figure 8.1: Variation of the band gap for Si nanocrystals, generated by layered growth methods as a function of volume.

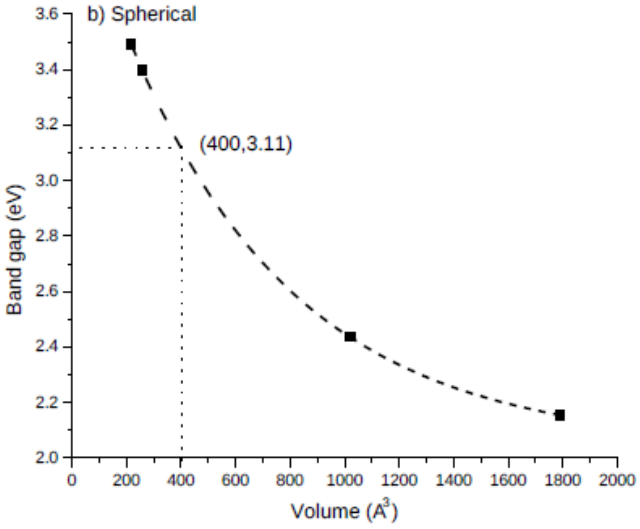

Figure 8.2: Variation of the band gap for Si nanocrystals, generated by spherical growth methods as a function of volume.

case, a 400 $\mathring{A}^3$ nanocrystal has a band gap of 3.25 eV, which is slightly larger than the band gap (3.11 eV) of a spherical nanocrystal with the same volume. However, moving to larger nanocrystals where the deviation in shape is greater, the deviations are much larger. *Hence different routes to synthesize nanoparticles could result in different physical properties for similar sized particles.*

We then went on to examine what the implications of the shape variations were on the degeneracy of the lowest three conduction band states and the top two valence band states. The degeneracies as well as the energies referenced to the valence band maximum are given in Table 8.1 for the layered as well as the spherical cases. While the valence band top's degeneracy remains unchanged, we do find deviations in the degeneracy of the conduction band bottom, which in some cases is singly degenerate and in some cases is triply degenerate. The character of the singly degenerate state is found to be s character, while that of the triply state is found to be p character. Bulk silicon is an indirect band gap material in which the conduction band bottom is singly degenerate and lies along GX direction. While at this juncture we cannot determine the exact symmetry of the conduction band bottom, we can in principle examine whether the band gap transition is optically active.

Evaluating the optical matrix elements, we still find that the oscillator strength of z polarized light is negligibly small (Table 8.2), therefore indicating that manipulating the degeneracy of the conduction band bottom as is artificially done here makes silicon very slightly optically active.

8.1.4 Conclusion

For the various sizes of Si nanoparticles considered we see that the degeneracy of the valence band maximum remains unchanged while we do find deviation in the degeneracy of the conduction band minimum, which in some cases is singly degenerate and in some cases its triply degenerate. From our studies we find that similar sized Si nanoparticles with different shapes can have different band gaps. Optical matrix elements are found to be smaller for larger Si nanocrystals while we see that smaller nanocrystals of Si becomes slightly optically active.

Table 8.1: The degeneracies of the highest two valence band (VB) states and lowest three conduction band (CB) states as a function of nanocrystal size. The corresponding energies (eV) given with respect to the valence band maximum.

	Nanocrystal size (n)	Degeneracy of		Energy of top 2 VB	Energy of bottom 3 CB
		Top 2 VB	Bottom 3 CB		
Layered					
	4	3,3	3,1,2	-0.097,0.0	2.664,2.729,2.796
	5	3,3	1,3,2	0.096,0.0	2.159, 2.186, 2.191
Spherical					
	3	3,3	1,2,3	0.237,0.0	3.483, 3.671, 3.751
	4	3,3	1,3,2	0.138,0.0	3.389, 3.468, 3.497
	5	2,3	1,3,2	0.259,0.0	2.428, 2.482, 2.502
	6	3,3	3,2,1	0.066,0.0	2.149, 2.158, 2.169

8.2 Tuning of Dopant Emission in Mn^{2+}-Doped CdS Nanocrystals

8.2.1 Introduction

Size-dependent optical properties of II-VI semiconductor nanocrystals, for example, tuning of emission color of CdSe nanocrystals across the visible range by tuning the particle size, has been one of the most important topic of fundamental research [6] with obvious technological applications. However, the utility of such intense emission for practical purposes is somewhat hindered by the process of self-absorption in case of these excitonic emissions with overlapping absorption and emission energies. It has been shown that, doping transition metal ions, in particular Mn^{2+} ions, into these semiconductor nanocrystals, gives rise to strong dopant-related emissions, at energies substantially lower than the band gap [7]. Such a large stokes shift between the absorption and emission spectra, overcome the vexing problem of self-absorption [8]. Also, doped nanocrystal emitters are

Table 8.2: The oscillator strength of z-polarized light of different sized nanocrystal.

	Nanocrystal size (n)	Oscillator strength
Layered		
	4	2.09E-04
	5	1.72E-04
Spherical		
	3	8.21E-04
	4	2.44E-04
	5	5.48E-04
	6	2.96E-04

relatively less sensitive to thermal and photochemical disturbances compared to their undoped counterpart[9]. Based on these advantages, doped semiconductor nanocrystals has been proven to be better phosphors in light emitting devices (LEDs)[8, 10] and nontoxic biological labels [11]. In spite of these advantages, the most important disadvantage of these doped nanocrystals is that, one cannot tune the emission color by tuning particle size, unlike their undoped counterpart. In a typical Mn^{2+}-doped II-VI semiconductor nanocrystal, where Mn^{2+} doping introduces *d*-states into the band gap of the host semiconductor, the excitation takes place in the host nanocrystal, whereas the de-excitation involves the dopant energy levels. Therefore, the emission energy is given by the energy difference between the first excited state and the ground state of Mn^{2+} *d*-states. Since Mn^{2+} $3d$ states are essentially localized, atomic-like states, with characteristic orbital spread much smaller than the typical nanocrystal size, a change in the nanocrystal size has no perceptible effect on emission energy of a given dopant in a semiconductor nanocrystal host, leading to a near constancy of the emission energy from the dopant, irrespective of the nanocrystal size. Thus, for a given system, such as Mn^{2+}-doped CdS nanocrystals, the energy for the Mn^{2+} *d*-emission is found to be constant at $\sim$ 2.13 eV [10]. The only way one achieves different emission colors is by changing the transition metal dopant ion[12]; however, this only allows few discrete emission colors, rather than a near-continuous tunability over a range of wavelengths. However, there are a few exceptions in the literature [13, 14] where Mn^{2+} d-emission energy has been reported down to 1.92 eV. In many of these reports, however, a strongly asymmetric emission spectrum,

instead of a symmetric emission peak of Gaussian kind, has been observed, this being attributed to overlapping of dopant emission with strong host related emissions [15, 16] Therefore, it is not clear in such cases whether the intrinsic Mn^{2+} *d*-emission energy could be altered.

Recently [17] it was found to be experimentally possible to tune Mn^{2+} *d*-emission color from Mn^{2+}-doped CdS nanocrystals, in the range of yellow to red by making slight changes in the reaction temperature. Time-delayed emission spectra [8, 14] measuring only Mn^{2+} *d*-emission with no contribution of host-related emissions provided them an unambiguous evidence of this tunability involving only Mn^{2+} *d*-levels. Detailed analysis of their experimental spectra coupled with our *ab-initio* theoretical studies have revealed the microscopic origin of changes in the electronic structure responsible for this tunability of emission energies. We establish that the Mn^{2+} ions residing at surface/sub-surface regions experience a different crystal field compared to those residing at the core of the nanocrystal, giving rise to subtle changes in the electronic structure at the transition metal site; the difference in the relative contributions of these different kinds of Mn^{2+} species to the overall spectrum gives rise to the tunability of the Mn^{2+} d-emissions. These new understandings also provide a tool, and may be the only tool to obtain information about the location of an emitting Mn^{2+} ion in the host nanocrystal.

8.2.2 Methodology

First principle structural optimization was carried out within a plane wave pseudopotential implementation of density functional theory to determine the bond-lengths between Mn^{2+} ion and its anion neighbors. Spherical clusters were constructed (refer section 6.1) retaining bulk-like coordination and a diameter of 2.2 nm, which is very similar to the diameter of the experimentally synthesized nanocrystals. The unit cell containing the nanocrystal was so defined as to have inter-nanocrystal separation equal to 10 Å, ensuring negligible interactions between nanocrystals. The surface of the nanocrystal was passivated with pseudo-hydrogens. Mn^{2+} ion was introduced to replace a Cd^{2+} ion at the surface, sub-surface as well as at the core regions of the nanocrystal in separate calculations. We use cut-off energy of 280 eV and a k-point mesh including only Gamma

point. Full geometry optimization was carried out. The energy eigenvalues corresponding to the Mn^{2+} induced levels were determined from an analysis of the character of the wavefunction.

8.2.3 Results and Discussion

It was experimentally observed [17] that the emission color of Mn doped CdS nanoparticles could be tuned from red to yellow by changing the reaction temperature. Analysis of the emission peaks revealed a multi-component character. Three peaks were identified at 2.14, 2.01 and 1.86 eV and the changes in the reaction temperature changed the relative intensities of the three features and hence brought about variations in the peak position.

They [17] observed the peak-I with maximum at 2.14 +/- 0.006 eV for all their samples, which also matches well with the observed emission maximum in the corresponding bulk samples [18], and is assigned to the Mn^{2+} ions situated at the Cd^{2+} substitutional site in the interior of the nanocrystal. This interpretation is further supported by the fact that they found an increase in the particle size from 1.9 to 2.6 nm, induced by an increase in the reaction temperature from 55 to 130 ^{o}C, leads to a substantial increase in the relative contribution of peak-I to the overall spectrum. Obviously, the larger particle has a smaller surface to bulk ratio, leading to a higher probability of Mn^{2+} incorporation in the interior of the nanocrystal than on its surface. In view of the Mn^{2+} emission for dopant in the core region appearing at 2.14 eV, it is natural to expect the originating lower energy emissions at 2.01 and 1.86 eV (peaks II and III) from different kinds of Mn^{2+} ions situated in perturbed environments, namely near the surface/sub-surface regions of the nanocrystal.

In order to establish the above interpretations conclusively, we have carried out *ab-initio* electronic structure calculations to determine $d - d$ transition energies for Mn^{2+} ions residing at different locations in such an nanocrystal. Separate calculations were carried out for the undoped nanocrystal and doped nanocrystals with one single Mn^{2+} ion introduced at the surface, sub-surface and the core of the CdS nanocrystal of size 2.2 nm. In each of these cases, the nanocrystal geometry was allowed to relax to minimize the total energy. The energy minimization leads to all four Mn^{2+}-S^{2-} bond-lengths for the case of core-doping to be 2.43 Å with a perfect tetrahedral symmetry. In contrast,

for the sub-surface Mn^{2+} ion, MnS_4 tetrahedral is found to be distorted with Mn^{2+}-S^{2-} bond-lengths being 2.41, 2.41, 2.42 and 2.43 Å. Using the results of these calculations, we extracted the $3d$ energy level diagram, as shown in Figs. 8.3 and 8.4 for d-levels of Mn^{2+} ions introduced at the core and sub-surface of the CdS nanocrystal, respectively, including the crystal field splitting. In order to arrive at these energy level diagrams, the eigenvectors of different energy eigenvalues are analyzed for their symmetry, the dominant atom type and angular momentum character. In the case of the Mn^{2+} ion at the core, the doubly degenerate eigenvalues in the up-spin channel with dominantly Mn^{2+} character are identified as the levels with e symmetry, while the triply degenerate levels with dominantly Mn^{2+} character are identified as the Mn^{2+} levels with t_2 symmetry, as shown in Fig. 8.3. The distortion in the MnS_4 tetrahedron near the surface region lifts the degeneracy of e and t_2 levels; this is further contributed by the presence of the terminating surface in the close vicinity on only one side of the MnS_4 unit, making the electronic potential even more asymmetric with respect to the central Mn^{2+} ion. Following the lifting of the degeneracy, the resulting Mn^{2+} d-level energy diagram is shown in Fig. 8.4. The splitting between the up and down-spin energy levels are determined by the intra-atomic exchange interaction strength as the Hunds coupling strength, J_H, with the spin-up and spin-down states being split by 4 J_H.

Earlier analysis [19] of *ab-initio* band structure has estimated J_H to be 0.8 eV for oxides. We expect a slightly lower value of J_H for the sulphides that form compounds with wider bands than the oxides; we find $J_H = 0.7$ eV to be more appropriate in the present case. Thus the spin splitting in both Figs. 8.3 and 8.4 are shown to be 2.8 eV. Mn^{2+} ion with five unpaired electrons defines the ground state as shown in the right hand side of Fig. 8.3, where all the up-spin e and t_2 states are occupied, giving rise to total spin multiplicity of 6. However for the 1st excited state, two up-spin e levels, two up-spin t_2 levels and one down-spin e level are occupied giving total spin multiplicity equal to 4, as shown in the left hand side of Fig. 8.3. The $d-d$ transition energy because of the transition from 1st excited state to ground state in Fig. 8.3 is calculated to be 2.20 eV, in good agreement with the experimentally observed transition energy for peak-I (2.14 eV). In passing, we note that a J_H value 0.68 eV will lead to a perfect agreement with the experimental value of 2.14 eV. However, our concern here is to understand the underlying mechanism of the tunability of

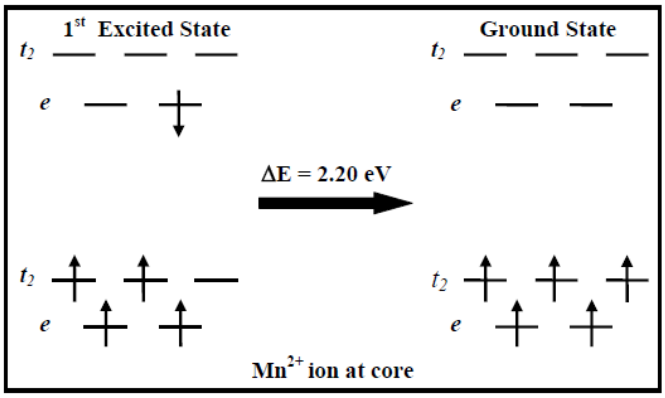

Figure 8.3: Schematic energy level diagrams showing the crystal field splitting of d-levels for Mn^{2+} ions at the core of a CdS nanocrystal.

dopant emission, rather than obtaining perfect quantitative agreement by fine tuning the parameter J_H. Carrying out the same analysis for the near-surface distorted tetrahedral case shown in Fig.8.4, we obtain the transition energy between 1st excited state and the ground state to be 2.04 eV. This calculated transition energy matches very well with that of peak-II (2.01 eV), thus, confirming the fact that peak-II originates from Mn^{2+} ions residing in the sub-surface of these nanocrystals. In view of these results, we believe that the third emission component with peak at 1.86 eV is from Mn^{2+} ions at the surface region with a 1-thioglycerol capping, since this situation would provide an even more strongly distorted crystal field and a consequent more emphatic lifting of the *d*-level degeneracies, which is at the heart of red-shift from peak-I, to peak-II to peak-III. However, an *ab-initio* calculation with such a large sized nanocrystal together with all flexibilities of capping agents including geometry optimization is way beyond the computational infrastructure available at present.

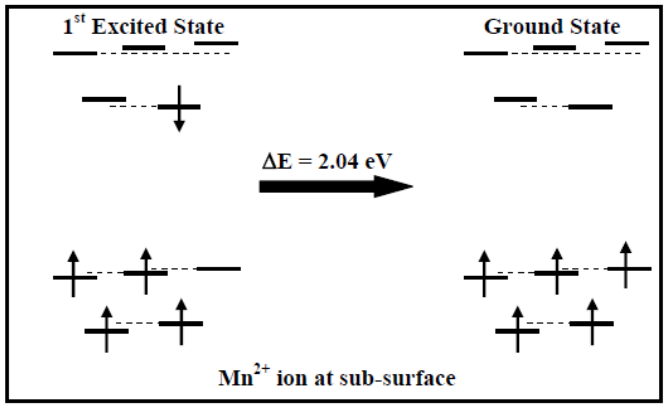

Figure 8.4: Schematic energy level diagrams showing the crystal field splitting of d-levels for Mn^{2+} ions at the sub-surface of a CdS nanocrystal. Dashed lines are just a guide to eye showing the lifting of degeneracy of e and t_2 levels.

8.2.4 Conclusion

Our results firmly establish the fact that Mn^{2+} ions residing at the interior and sub-surface of an nanocrystal, exhibit shift in the emission due to a change in the crystal field leading to a lifting of *d*-level degeneracies. Interestingly, each of these emission from three distinct dopant sites are insensitive to the nanoparticle size, as should indeed be expected in view of the atomic-like nature of transition metal *d*-levels.

Bibliography

[1] Z. H. Lu, D. J. Lockwood, and J. M. Baribeau, Nature **378**, 258 (1995).

[2] L. T. Canham, Appl. Phys. Lett. **57**, 1046 (1990).

[3] Y. Kanzawa, T. Kageyama, S. Takeoka, M. Fujii, S. Hayashi, and K. Yamamoto, Solid State Commun. **102**, 533 (1997).

[4] S. Sapra, R. Viswanatha, and D. D. Sarma, J. Phys. D: Appl. Phy. **36** , 1595 (2003); R. Viswanatha, S. Sapra, T. S. Dasgupta, and D. D. Sarma,Phys. Rev. B **72**, 045333 (2005).

[5] B. Adolph, J. Furthmuller, and F. Bechstedt, Phys. Rev. B **63**, 125108 (2001).

[6] C. B. Murray, D. J. Norris, and M. G. Bawendi, J. Am. Chem. Soc. **115**, 8706 (1993) ; A. P. Alivisatos, Science **271**, 933 (1996); C. N. R. Rao and A. K. Cheetham, J. Mater. Chem. **11**, 2887 (2001); C. Burda, X. Chen, R. Narayanan, and M. A. El-Sayed, Chem. Rev. **105**, 1025 (2005); A. Kongkanand, K. Tvrdy, K. Takechi, M. Kuno, and P. V. Kamat, J. Am. Chem. Soc. **130**, 4007 (2008); P. K. Santra, R. Viswanatha, S. M. Daniels, N. L. Pickett, J. M. Smith, P. OBrien, and D. D. Sarma, J. Am. Chem. Soc. **131**, 470 (2009).

[7] L. Levy, N. Feltin, D. Ingert, and M. P. Pileni, J. Phys. Chem. B **101**, 9153 (1997); S. C. Erwin,L. Zu, M. I. Haftel, A. L. Efros, T. A. Kennedy, and D. J. Norris, Nature **436**, 91 (2005); Y. Yang, O. Chen, A. Angerhofer, and C. J. Cao, J. Am. Chem. Soc. **128**, 12428 (2006); A. Nag, S.Chakraborty, and D. D. Sarma, J. Am. Chem. Soc. **130**, 10605 (2008); R. Beaulac, P. I. Archer, and D. R. Gamelin, Journal of Solid State Chemistry **7**, 1582 (2008); D. J. Norris, A. L. Efros, and S. C. Erwin,

Science **319**, 1776 (2008); R. Beaulac, P. I. Archer, X. Liu, S. Lee, G. M. Salley, M. Dobrowolska, J. K. Furdyna, and D. R. Gamelin, Nano Lett **8**, 1198 (2008).

[8] A. Nag and D. D. Sarma, J. Phys. Chem. C **111**, 13641 (2007).

[9] N. Pradhan and X. Peng, J. Am. Chem. Soc. **129**, 3339 (2007).

[10] H. Yang and P. H. Holloway, J. Phys. Chem. B **107**, 9705 (2003); H. Yang, P. H. Holloway and B. B. Ratna, J. Appl. Phys. **93**, 586 (2003); N. pradhan, N. R. Jana, and D. D. Sarma (to be published)

[11] N. Pradhan, D. Goorskey, J. Thessing, and X. Peng, J. Am. Chem. Soc. **127**, 17586 (2005); N. Pradhan, D. M. Battaglia, Y. Liu, and X. Peng, Nano Lett. **7**, 312 (2007); R. Thakar, Y. Chen, P. T. Snee, Nano Lett. **7**, 3429 (2007); N. R. Jana, N. Pradhan, and D. D. Sarma (unpublished)

[12] R. Viswanatha, S. Chakraborty, S. Basu, and D. D. Sarma, J. Phys. Chem. B **110**, 22310 (2006).

[13] M. Tanaka, J. Qi, and Y. Masumoto, J. Crystal Growth **214/215**, 410 (2000).

[14] A. Nag, S. Sapra, C. Nagamani, A. Sharma, N. Pradhan, S. V. Bhat, and D. D. Sarma, Chem. Mater. **19**, 3252 (2007).

[15] M. A. Chamarro, V. Voliotis, R. Grousson, P. Lavallard, T. Gacoin, G. Counio, J. P. Boilot, and R. Cases, J. Crystal Growth **159**, 853 (1996).

[16] H. Yang and P. H. Holloway, Appl. Phys. Lett. **82**, 1965 (2003).

[17] A. Nag and D. D. Sarma (unpublished).

[18] O. Goede and W. Heimbrodt, phys. stat. sol. (b) **146**, 11 (1998).

[19] P. Mahadevan, N. Shanthi, and D. D. Sarma, J. Phys.: Condens. Matter **9**, 3129 (1997).